IOWA STATE UNIVERSITY
Digital Repository

2009

Ion distributions at charged aqueous surfaces: Synchrotron X-ray scattering studies

Wei Bu
Iowa State University

Follow this and additional works at: http://lib.dr.iastate.edu/etd

Part of the Physics Commons

Ion distributions at charged aqueous surfaces: Synchrotron X-ray scattering studies

by

Wei Bu

A dissertation submitted to the graduate faculty

in partial fulfillment of the requirements for the degree of

DOCTOR OF PHILOSOPHY

Major: Condensed Matter Physics

Program of Study Committee:
David Vaknin, Co-major Professor
Alex Travesset, Co-major Professor
Kai-Ming Ho
David Carter-Lewis
Xueyu Song

Iowa State University

Ames, Iowa

2009

TABLE OF CONTENTS

LIST OF TABLES

LIST OF FIGURES

ACKNOWLEDGEMENTS

I would like to take this opportunity to express my thanks to those who helped me with various aspects of conducting research and the writing of this thesis. It is impossible to list all these people's names. If your name is not listed, rest assured that my gratitude is not less than for those listed below.

First and foremost, I would like to thank my advisors. Dr. David Vaknin's encouragement and invaluable suggestions during this work have taught me how good experimental physics is done and what it really means to be an experimental physicist. Moreover, the joy and enthusiasm he has for his research was contagious and motivational, even during tough times in the pursuit of a Ph.D.. I would also like to thank my co-advisor Dr. Alex Travesset for his tremendous contribution to the theoretical work of this thesis and helpful discussion of experiments. In addition, I want to express my gratitude to my other committee members Dr. Kai-Ming Ho, David Carter-Lewis, and Xueyu Song for their time, interest, and helpful comments.

All the X-ray work presented in this thesis was carried out at Beamline 6ID-B at the Advanced Photon Source, Argonne National Laboratory. I would like to thank the scientists at the APS μCAT, especially Douglas Robinson for sharing his expertise on X-ray techniques and our discussion of liquid surface scattering. I also want to thank Philip Ryan, Jong-Woo Kim, and Didier Wermeille for their volume of helpful technical support. Undergraduate students in our group Kevin Flores, Jacob Pleasants, and Jonathan Kent are thanked for partial data collection and sample preparation work they have done.

On the personal side, I would like to thank my parents for raising me with a love of science and supporting me in all my pursuits, and my little son Aaron for providing me a powerful source of inspiration and energy. I would also like to thank my friends and relatives for their

loving guidance and encouragement during the writing of this work. Last but not least, I want to thank my loving, supportive, encouraging, and patient wife Ying whose faithful support during the final stages of this Ph.D. and my entire life is so appreciated. Thank you.

ABSTRACT

Surface sensitive synchrotron X-ray scattering studies were performed to obtain the distribution of monovalent ions next to a highly charged interface at room temperature. To control surface charge density, lipids, dihexadecyl hydrogen-phosphate (DHDP) and dimysteroyl phosphatidic acid (DMPA), were spread as monolayer materials at the air/water interface, containing CsI at various concentrations.

Five decades in bulk concentrations (CsI) are investigated, demonstrating that the interfacial distribution is strongly dependent on bulk concentration. We show that this is due to the strong binding constant of hydronium H_3O^+ to the phosphate group, leading to proton-transfer back to the phosphate group and to a reduced surface charge. Using anomalous reflectivity off and at the L_3 Cs^+ resonance, we provide spatial counterion (Cs^+) distributions next to the negatively charged interfaces. The experimental ion distributions are in excellent agreement with a renormalized surface charge Poisson-Boltzmann theory for monovalent ions without fitting parameters or additional assumptions.

Energy Scans at four fixed momentum transfers under specular reflectivity conditions near the Cs^+ L_3 resonance were conducted on 10^{-3} M CsI with DHDP monolayer materials on the surface. The energy scans exhibit a periodic dependence on photon momentum transfer. The ion distributions obtained from the analysis are in excellent agreement with those obtained from anomalous reflectivity measurements, providing further confirmation to the validity of the renormalized surface charge Poisson-Boltzmann theory for monovalent ions. Moreover, the dispersion corrections f' and f'' for Cs^+ around L_3 resonance, revealing the local environment of a Cs^+ ion in the solution at the interface, were extracted simultaneously with output of ion distributions.

Another independent technique, X-ray fluorescence near total reflection was used to study ion adsorption at charged surfaces. Below the critical angle, the X-ray fluorescence spectra are only surface sensitive, providing the direct evidence of existence of Cs^+ at the surface. Above the critical angle, combination of fluorescence spectra with and without the presence of monolayer materials yields the number of accumulated Cs^+ per lipid at the surface. In addition, the fluorescence spectra collected as a function of incident X-ray energy near the L_3 edge provide the dispersion corrections, consistent with the results from the energy scans.

CHAPTER 1.   INTRODUCTION

1.1   Ion Distribution near a Charged Surface

Charged surfaces in aqueous systems can be formed by the ionization or dissociation of surface groups or the adsorption of ions from solution onto a previously uncharged surface (e.g., dipolar; zwitterionic moieties). Whatever the source of the surface charges is, the electrostatic field generated by the surface charges affects the distribution of ions in the solution. The electrostatic field in combination with the thermal motion of the ions results in an electrical double layer, which consists of two parallel layers of ions. The first layer is the surface charge (either positive or negative), while the second layer consists of a diffuse layer of ions, which screens the electric field of the first layer. Counterion distribution in the second layer is the key in many research fields, such as electrochemistry, interface and colloid science, and biophysics. It is important for some processes at a variety of interfaces (e.g., solid electrodes, charged biomembranes, biomolecules, mineral surface, etc.), as well as in technological applications (e.g., paints, printing, corrosion inhibition, etc.).

The theoretical determination of ion distributions in aqueous solutions was initiated almost a century ago by Gouy [1] and Chapman [2], who applied the Poisson-Boltzmann (PB) theory. Ever since their seminal work, the topic remains central in statistical mechanics, physical chemistry, and biophysics [3]. The original PB theory is a mean field theory with some simplified assumptions such as (i) ions are point charges; (ii) surface charge density is uniform; (iii) the ionic adsorption energy is purely electrostatic; and (iv) the aqueous solution is modeled as a continuous media with a permittivity constant ε.

Here, as an example, we briefly review the PB theory for a single charged planar surface placed in contact with an aqueous symmetrical (e.g., 1:1) electrolyte solution. Without loss
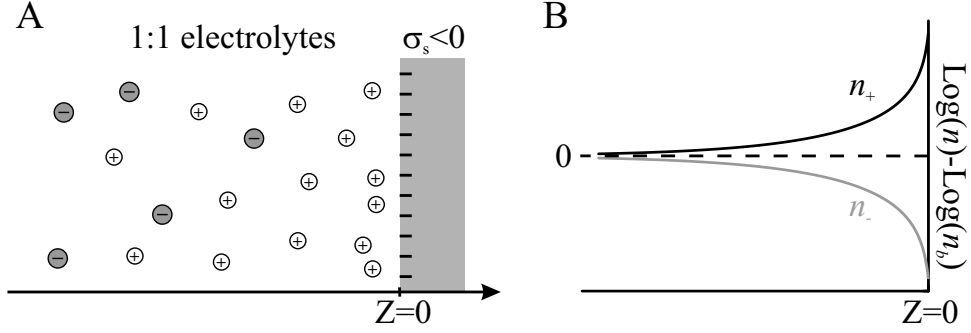
Figure 1.1   (A) Schematic illustration of a single charged surface with surface charge density, $\sigma_s < 0$, at $z = 0$ and monovalent electrolytes in the bulk ($z < 0$). (B) Monovalent counterion (n_+) and co-ion (n_-) distributions according to Eq. 1.9.

of generality, the surface charge is fixed and negative, while electrolytes are monovalent. The system geometry is depicted on Fig. 1.1(A). The negatively charged surface with surface charge density σ_s, is placed at $z = 0$, and monovalent electrolytes (i.e., ions) occupy the negative half ($z < 0$) with average bulk concentration n_b. As the surface charge is uniformly distributed, the electric potential ψ depends only on the distance from the interface z, and the Boltzmann distribution is

$$\rho(z) = en_b[e^{-e\psi(z)/k_BT} - e^{e\psi(z)/k_BT}] = -2en_b \sinh \phi(z), \tag{1.1}$$

where k_B is the Boltzmann constant and $\phi(z) = e\psi(z)/k_BT$. On the other hand, according to the well-known Poisson equation, the electric potential ψ is determined by the net excess charge density at z:

$$\nabla^2 \psi(z) = -\frac{\rho(z)}{\varepsilon_0 \varepsilon_r}, \tag{1.2}$$

where ε_r is the relative permittivity. Substituting Eq. 1.1 into Eq. 1.2 gives

$$d^2\phi/dz^2 = \sinh \phi/\lambda_D^2, \tag{1.3}$$

where $\lambda_D = (\varepsilon_0 \varepsilon_r k_B T/2e^2 n_b)^{1/2}$ is the Debye screening length. Integrating both sides of Eq. 1.3 with ϕ and using the boundary condition at $z \to -\infty$ ($\phi \to 0$ and $d\phi/dz \to 0$), one can readily get

$$d\phi/dz = \frac{2}{\lambda_D} \sinh \frac{\phi}{2},$$

which may be integrated by using the integral $\int \mathrm{csch} Y \, dY = \ln(\tanh(Y/2))$ to yield

$$\tanh(\phi(0)/4)\mathrm{e}^{z/\lambda_D} = \tanh(\phi/4).$$

Applying inverse function of hyperbolic tangent, $\tanh^{-1} Y = \frac{1}{2}\ln\left(\frac{1+Y}{1-Y}\right)$, to the above equation, gives the analytical solution for the potential

$$\psi(z) = \frac{\phi(z)k_BT}{e} = -\frac{2k_BT}{e}\ln\left(\frac{1 + \gamma\mathrm{e}^{z/\lambda_D}}{1 - \gamma\mathrm{e}^{z/\lambda_D}}\right), \tag{1.4}$$

with $\gamma = -\tanh(\phi(0)/4) > 0$ determined by the surface potential.

The electric field in the negative half is immediately found as

$$\mathbf{E}(z) = -\frac{d\psi(z)}{dz} = -\frac{2k_BT}{e\lambda_D}\sinh\frac{\phi(z)}{2}, \tag{1.5}$$

which yields the electric field strength at the surface $(z \to 0^-)$

$$E(z \to 0^-) = -\frac{2k_BT}{e\lambda_D}\sinh\frac{\phi(0)}{2} = -\frac{2k_BT}{e\lambda_D}\frac{2\tanh\frac{\phi(0)}{4}}{1 - \tanh^2\frac{\phi(0)}{4}} = \frac{2k_BT}{e\lambda_D}\frac{2\gamma}{1 - \gamma^2}. \tag{1.6}$$

On the other hand, the surface electric field strength also can be calculated by the surface charge density according to Gauss's law, $E(z \to 0^-) = \frac{|\sigma_s|}{\varepsilon_0\varepsilon_r}$. Combination of this equation with Eq. 1.6 yields a quadratic equation,

$$\gamma^2 + 2\gamma\frac{\lambda_{GC}}{\lambda_D} - 1 = 0, \tag{1.7}$$

where $\lambda_{GC} = 2k_BT\varepsilon_0\varepsilon_r/|\sigma_s|e$ is the Gouy-Chapman length. The positive root of this quadratic equation gives an expression for γ,

$$\gamma = -\frac{\lambda_{GC}}{\lambda_D} + \sqrt{\left(\frac{\lambda_{GC}}{\lambda_D}\right)^2 + 1}. \tag{1.8}$$

Once the potential profile is known, ionic distributions can be obtained from Eq. 1.4 and the Boltzmann distribution, expressed as

$$n_{\pm}(z) = n_b\left(\frac{1 \pm \gamma\mathrm{e}^{z/\lambda_D}}{1 \mp \gamma\mathrm{e}^{z/\lambda_D}}\right)^2, \tag{1.9}$$

providing the counterion (n_+) and co-ion (n_-) distributions shown in Fig. 1.1(B). Obviously, the counterion has an excess concentration, while the co-ion has a deficit near the charged surface as the negatively charged surface attracts counterions and repels co-ions.
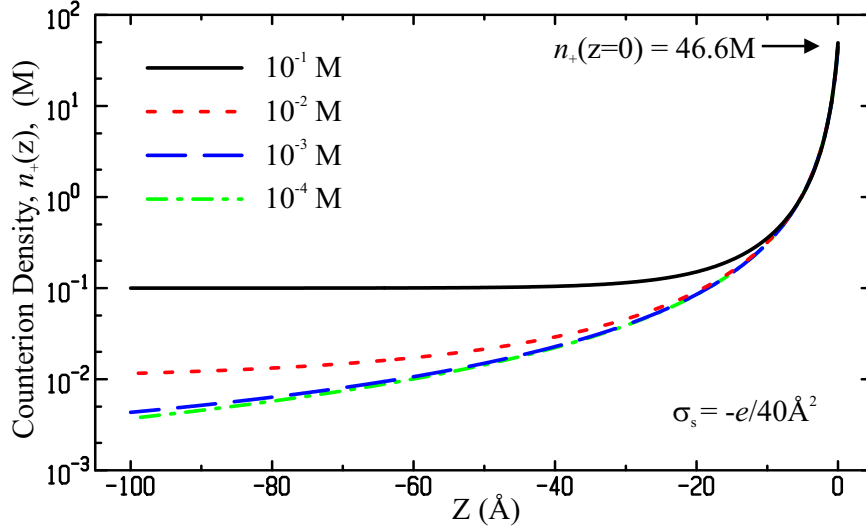
Figure 1.2 Calculated monovalent ion distributions $n_+(z)$ near a negatively charged surface as obtained from PB theory, Eq. 1.9, for different bulk concentration as indicated. Surface charge density σ_s is one electron charge per 40 Å^2, $\varepsilon_r = 80$, and $T = 293$ K. Note that the value of the distribution at the $z = 0$ is practically a constant (i.e., independent of ionic bulk concentration n_b).

Figure 1.2 shows the calculated counterion distribution using Eq. 1.9 for a fixed surface charge density $\sigma_s = -e/40\text{Å}^2 = -0.4\,\text{C/m}^2$ and several salt concentrations. It is worth noting that for this surface density ($\lambda_{GC} \approx 0.9$ Å) and bulk salt concentrations ($\lambda_D = 304.7$ and 9.6 Å at 10^{-4} and 10^{-1}M, respectively), $\frac{\lambda_{GC}}{\lambda_D} \ll 1$ and $\gamma \approx 1 - \frac{\lambda_{GC}}{\lambda_D}$, the concentration of counterions next to the interface is independent of bulk concentration,

$$n_+(z) \approx \frac{2\varepsilon_0\varepsilon_r k_B T}{e^2(z + \lambda_{GC})^2}; \quad \text{for} \frac{z}{\lambda_D} \ll 1.$$

At the surface ($z = 0$), the counterion density is given by

$$n_+(0) \approx \frac{\sigma_s^2}{2\varepsilon_0\varepsilon_r k_B T} = 46.6 \text{ M},$$

for $\sigma_s = -e/40\text{Å}^2$, $\varepsilon_r = 80$, and $T = 293$ K. As shown in Fig. 1.2, one can readily find two conclusions for a system with highly charged surface σ_s and dilute bulk concentration n_b: (i) excess counterions are concentrated in the first $10-15$ Å from the surface, and (ii) counterion concentration is almost independent of bulk concentration in that region. PB theories

for asymmetrical electrolytes and other non-planar geometry such as sphecial and cylindrical coordinates are discussed in Ref. [4].

Since Guoy and Chapman introduced the PB theory, a series of modifications have been raised to correct for the assumptions in the original PB theory. To account for the finite ionic radius, Stern introduced a phenomenological layer with a different dielectric constant, named the Stern layer, in which the electric potential drops linearly [5]. The effect of excess salt concentration and the resulting screening was extended by Debye-Hückel [6]. Grahame generalized the Gouy-Chapman theory to multivalent ions [7]. Subsequently, more refined theories and numerical simulations were developed to incorporate short-range interactions, image charges, finite size ionic radius, and ion-ion correlations [8, 9, 10, 11, 12]. More recently, modifications of PB theory have been developed to incorporate hydration forces [13, 14, 15]. Some first-principles calculations of surface tension for amphiphilic monolayers assume a PB theory with one or more layers of varying dielectric constant [16].

Experimental support for the validity of PB theory was provided by electrokinetic, visco-electric effects, and other techniques [17]. McLaughlin and collaborators [18] have shown good agreement between ζ potentials computed from PB theories and electrophoretic measurements in lipid vesicles. Other techniques, such as radiotracer experiments [19, 20, 21], X-ray reflectivity [22, 23, 24], or infrared spectroscopy [25], allow the determination of the total amount of ions in the immediate vicinity of a charged interface. It is noteworthy that all of the experimental data for monovalent ions (at moderate salt concentrations ≤ 0.1 M) outlined above are adequately described by the Guoy-Chapman theory (with the generalization of excess salt) with no need for further corrections [23, 26]. A close inspection, however, shows that the agreement between theory and experiment is either based on fitting variables such as surface charge or interfacial dielectric values that are not known in advance and/or based on integrated quantities. As an example, it has been shown recently that the degree of proton dissociation of arachidic acid as a monolayer on a sodium salt solution is adequately described by PB theory, but this agreement only involves the integral (over the entire space) of the sodium distribution [25, 26]. Thus, local deviations that preserve the integral of the distribution (i.e., total number of ions) are

not discriminated by these experiments. On the other hand, force measurements between two charged membranes separated by salt solutions, although well described by PB theory at large distances, show strong deviations at short distances $(1-2 \text{ nm})$ [3, 13]. The origin of these hydration forces is still controversial. In some cases, it has been suggested to extend PB theory to incorporate the restructuring of water, resulting in ion distributions that deviate from PB at short distances from the interface [14, 27, 28]. It is therefore imperative to determine the ion distribution itself to establish the degree of accuracy of PB theory.
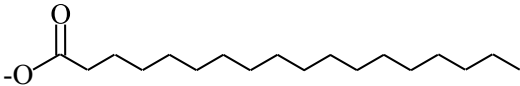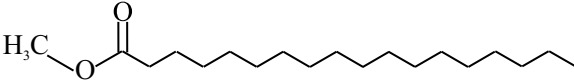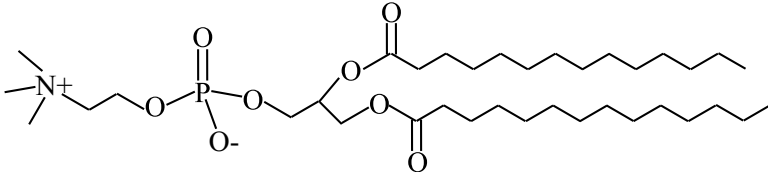
1.2 Langmuir Monolayers

A Langmuir monolayer (LM) is a one-molecule thick insoluble layer of an organic material spread onto an aqueous subphase (typically water with or without salts in the bulk). The first person to make worthwhile, reproducible measurements on monolayers was Agnes Pockels who performed her first experiments on monolayers in her kitchen, starting in about 1882. However, this system is now named after Irving Langmuir since he was the first to understand its structure at the molecular level, in particular the fact that the molecules show a preferential orientation.

Traditional compounds used to prepare LMs are amphiphilic materials that possess a hydrophilic (polar) headgroup and a hydrophobic tail typically consisting of one or two hydrocarbon chains [29, 30, 31]. The amphiphilic nature of the monolayer materials dictates the orientation of the molecules at the air/water interface in such a way that the polar headgroup is immersed in the water and that the long hydrocarbon chain is pointing towards air. Typical examples of molecules that form monolayers are fatty acids, phospholipids, alcohols, and others as shown in Table 1.1.

The length of the hydrocarbon chain can be chemically varied, affecting the hydrophobic character of the molecule. If the tail is long (i.e., hydrophobic) enough (typically more than 12 hydrocarbons or groups in the chain; $(CH_2)n$, $n > 12$), the material is insoluble, and the molecules on the surface of the liquid subphase form an isolated two-dimensional system. If the chain is shorter, though still insoluble in water, the monolayer materials may form a micelle, which is an aggregate with the hydrophilic headgroup regions in contact with surrounding sol-

Table 1.1   Structure and catalog of typical examples for monolayer materials.

catalog	structure
fatty acid	
fatty methyl ester	
alcohol	
phospholipid	

vent, sequestering the hydrophobic single tail regions in the micelle center. Monolayer molecules insoluble in water can, with the help of a volatile and water insoluble solvent (chloroform or hexane is commonly used), readily be spread on a water surface.

There are many reasons to study LMs. Besides providing an excellent model system for studying ordering in two dimensions, one of the most important reasons is their close relationship to membrane biophysics. Membranes of all living cells and organelles within cells consist of lipid bilayers (two weakly coupled monolayers) interpenetrated with specific proteins, cholesterol, and other organic compounds that combine to create functional ensembles which determine transport of matter and energy through them. LMs can therefore be used as a model system to simulate the chemical and biological reactions of membranes in living cells.

LMs have been studied for more than a century, but the field has undergone a revolution in the last two decades. This is partially due to the development of novel experimental techniques, such as synchrotron X-ray diffraction experiments [32, 33], which yield the LMs structure at the molecular scale. Additionally, new microscopy techniques, such as fluorescence microscopy

[34], polarized fluorescence microscopy [35] and Brewster-angle microscopy [36, 37], allow for the visualization of the mesoscopic structures in LMs. These techniques are often more sensitive to phase transitions in monolayers than classical isotherm measurements.

1.3   Motivation and Techniques

In this thesis, we mainly focus on monovalent ion distributions near a highly charged LM surface. The reason for studying this system is twofold. First, ions at a cell membrane (consisting of two LMs) surface affect the function and conformation of nearby molecules and thus play an important role in inter- and intracellular processes (such as, cell-cell recognition) and biomimetic mineralization processes [38, 39, 40, 41]. Second, when monolayer materials with ionic headgroups are spread on the water surface, they give a uniformly charged surface with planar geometry, which is the experimental prerequisite for testing PB theory.

Synchrotron X-ray scattering techniques are commonly used and are powerful tools for studying LMs. Grazing incidence X-ray diffraction and X-ray reflectivity are well suited for extracting LMs structure on the molecular length scale [42, 43, 44]. Grazing incidence X-ray diffraction is useful for identifying the in-plane structure of LMs, while X-ray reflectivity is well suited to determine the gradient of electron density profile normal to an interface, including contributions from all constituents in the system (no specificity). However, anomalous X-ray reflectivity technique, by collecting reflectivity data at different energies (at and away from the resonance of a specific ion), can yield the spatial distributions of the probed ion. This was successfully applied to extract the ion distribution from an organic thin film [45], a metal oxide thin film [46], and a charged LM surface [47]. Energy scans at fixed momentum transfer (dubbed resonant anomalous X-ray reflectivity in some literature) is a technique with an ability to yield specific ion distribution, as well as the dispersion corrections at the interface [48]. The near total X-ray reflection fluorescence, which make use of the characteristic emission line spectra of ions, is another common technique to determine ion adsorption specifically and quantitatively near the interface [49, 50, 51], yet it does not yield spatial information. The studies presented in this thesis utilize X-ray techniques to investigate the monovalent ions distribution near a highly

charged LM surface.

CHAPTER 2. THEORETICAL BACKGROUND FOR THE MAIN X-RAY TECHNIQUES

2.1 X-ray Reflectivity (XR)

2.1.1 X-ray Refractive Index

The refractive index n of a medium is defined as the ratio of the phase velocity c of a wave in the vacuum to the phase velocity v_p in the medium itself: $n = c/v_p$. For electromagnetic waves (EW), it equals $n = \sqrt{\varepsilon_r \mu_r}$, where ε_r is the material's relative permittivity, and μ_r is its relative permeability. For nonmagnetic materials with $\mu_r = 1$, the refractive index can be reduced to

$$n(\mathbf{r}) = \sqrt{\varepsilon_r(\mathbf{r})}. \tag{2.1}$$

$\varepsilon_r(\mathbf{r})$ is defined as $\varepsilon_r(\mathbf{r}) = 1 + \frac{\mathbf{P}(\mathbf{r})}{\varepsilon_0 \mathbf{E}(\mathbf{r})}$, where $\mathbf{P}(\mathbf{r})$ is the polarization (i.e., dipole moment per unit volume), and $\mathbf{E}(\mathbf{r})$ is the electric field.

Let us consider a plane harmonic EW with frequency ω and wave vector $\mathbf{k}_0$. The electric field can induce a displacement for each free electron in the medium, equal to $-\frac{e}{m_e \omega^2}\mathbf{E}(\mathbf{r})$, where m_e is the mass of the electron. Then the polarization is given by

$$\mathbf{P}(\mathbf{r}) = -\frac{\rho_e(\mathbf{r})e^2}{m_e \omega^2}\mathbf{E}(\mathbf{r}) = -\frac{4\pi \varepsilon_0 \rho_e(\mathbf{r})r_0}{k_0^2}\mathbf{E}(\mathbf{r}), \tag{2.2}$$

where $k_0 = |\mathbf{k}_0| = 2\pi/\lambda$, $\rho_e(\mathbf{r})$ is the electron density at $\mathbf{r}$ in the medium, and $r_0 = e^2/4\pi \varepsilon_0 m_e c^2 = 2.82 \times 10^{-13}$cm is the classical radius of the electron. Using the definition of ε_r and Eq. 2.2, one can rewrite Eq. 2.1 as

$$n(\mathbf{r}) = \sqrt{1 - \frac{4\pi \rho_e(\mathbf{r})r_0}{k_0^2}} \simeq 1 - \frac{2\pi \rho_e(\mathbf{r})r_0}{k_0^2}. \tag{2.3}$$

Other than scattering, absorption processes also take place in the medium. After traveling a distance z within the medium, the X-ray intensity is attenuated by a factor of $e^{-\mu z}$, but the

amplitude only by a factor of $e^{-\mu z/2}$, where μ is the linear absorption coefficient. Assuming that the X-ray beam strikes into the medium at the normal angle from the vacuum, the wave vector changes from k_0 in the vacuum to nk_0 in the medium. If the refractive index n is now allowed to be a complex number, $n = 1 - \delta + i\beta$, then the wave propagating in the medium is

$$e^{ink_0 z} = e^{i(1-\delta)k_0 z}e^{-\beta k_0 z},$$

which implies $\beta k_0 = \mu/2$. In general, the X-ray refractive index of a medium can be written in the following form:

$$n = \sqrt{1 - 2\delta + 2i\beta}$$

$$n = 1 - \delta + i\beta$$

with

$$\delta = \frac{2\pi \rho_e(\mathbf{r}) r_0}{k_0^2} \quad \text{and} \quad \beta = \mu/2k_0. \tag{2.4}$$

δ and β are wavelength dependent, and typically of the order of 10^{-6} and 10^{-8}, respectively, for X-ray of wavelength 1 Å.

Assuming no absorption ($\beta = 0$), the refractive index can be reduce to $n = \sqrt{1 - 2\delta}$, which is smaller than 1, implying that X-rays undergo total external reflection. It means this kind of total reflection takes place outside of the material, which is different from the total internal reflection for the visible light. Snell's law relates the incident angle α to the refracted angle α' (see Fig. 2.1), $\cos\alpha = n\cos\alpha'$. Expanding this equation for small angles of incidence yields $\alpha^2 - \alpha'^2 = 2\delta$. The critical angle for the total reflection α_c, obtained when $\alpha' = 0$, is given by

$$\alpha_c = \sqrt{2\delta}. \tag{2.5}$$

Its value is typically of the order of milli-radian for 1 Å X-ray. Critical angles at $\lambda = 1.54$ Å for the selected materials are shown in Table. 2.1.

2.1.2 Reflectivity from an Ideally Flat Interface

When a plane EW with unit amplitude moves from air into the medium, separated by an ideally flat interface (zero roughness) with air, it will be specularly reflected and transmitted as

Table 2.1 Electron density, critical angle, δ, and β at $\lambda = 1.54$ Å for the selected materials. δ and α_c are calculated from Eqs. 2.4 and 2.5, respectively. β is given by X-ray web resource [52].

	ρ_e $(e/\text{Å}^3)$	δ $(\times 10^{-6})$	β $(\times 10^{-8})$	α_c (deg)
H_2O	0.334	3.555	1.215	0.153
Si	0.699	7.440	1.728	0.221
Hg	3.249	34.583	348.6	0.477

shown in Fig. 2.1. The reflection is referred to Fresnel reflectivity. The amplitude of the reflected wave and transmitted wave are called the Fresnel reflectance r and Fresnel transmittance t, respectively.

For the neutral and nonmagnetic medium, X-ray wave equations can be derived from the following Maxwell's equations

$$\nabla \times \mathbf{E} = -\partial \mathbf{B}/\partial t, \tag{2.6}$$

$$\nabla \times \mathbf{H} = \partial \mathbf{D}/\partial t, \tag{2.7}$$

$$\nabla \cdot \mathbf{D} = 0, \tag{2.8}$$

$$\nabla \cdot \mathbf{H} = 0. \tag{2.9}$$

Taking the curl of Eqs. 2.6 and 2.7, using $\nabla \times \nabla \times \mathbf{A} = \nabla(\nabla \cdot \mathbf{A}) - \nabla^2 \mathbf{A}$, $\mathbf{D} = \varepsilon_0 \varepsilon_r(\mathbf{r})\mathbf{E}$, and $\mathbf{B} = \mu_0 \mathbf{H}$, and noticing $\partial^2/\partial^2 t \rightarrow -\omega^2$ for time-harmonic wave, one can obtain

$$\nabla^2 \mathbf{E} + \xi^2 \mathbf{E} = -\nabla(\nabla \ln \varepsilon_r(\mathbf{r}) \cdot \mathbf{E}), \tag{2.10}$$

$$\nabla^2 \mathbf{H} + \xi^2 \mathbf{H} = -\nabla \ln \varepsilon_r(\mathbf{r}) \times (\nabla \times \mathbf{H}), \tag{2.11}$$

where $\xi^2 = \omega^2 \mu_0 \varepsilon_0 \varepsilon_r(\mathbf{r}) = \varepsilon_r(\mathbf{r})k_0^2 = n^2(\mathbf{r})k_0^2$.

For a stratified medium with an electron density that varies along one direction, z, the relative permittivity becomes $\varepsilon_r(\mathbf{r}) = \varepsilon_r(z)$. In this case, it is convenient to divide the wave into two parts: an s-wave component and a p-wave component as defined in Fig. 2.1. For an s-wave with the electrical field parallel to the surface, one can readily get $\nabla \ln \varepsilon_r(\mathbf{r}) \cdot \mathbf{E} = 0$. Then Eq. 2.10 can be reduced to a scalar equation

$$\nabla^2 E_x + \xi^2 E_x = 0. \tag{2.12}$$
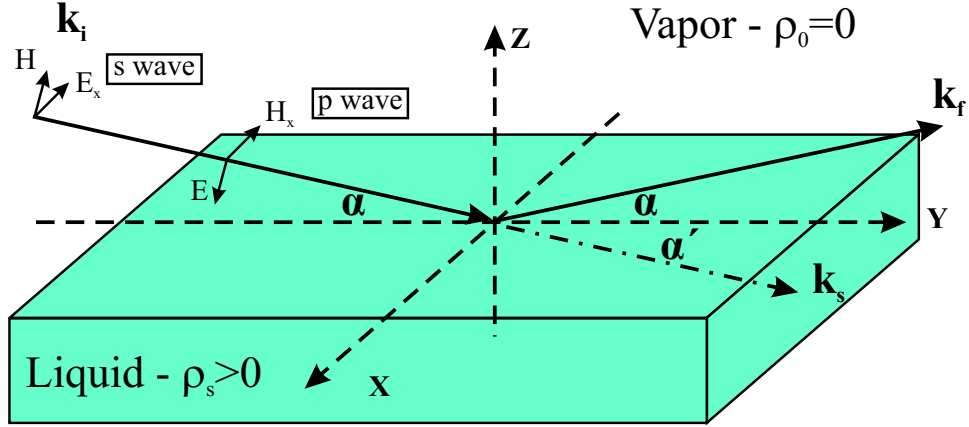
Figure 2.1   Illustration of the incidence ($\mathbf{k_i}$), reflection ($\mathbf{k_f}$), and transmission ($\mathbf{k_s}$) of a plane wave X-ray on a stratified medium. S-wave has an electric intensity vector $\mathbf{E} = \hat{\mathbf{x}}E_x$ pointing in the x-axis, while p-wave has a magnetic intensity vector $\mathbf{H} = \hat{\mathbf{x}}H_x$.

By symmetry arguments, the field in the medium does not depend on the x-axis, and the y-component of the wave vector is conserved when the wave travels into the medium, $k_{i,y} = k_0 \cos\alpha = k_0 n \cos\alpha' = |\mathbf{k_s}| \cos\alpha'$. Therefore, the general solution to Eq. 2.12 is given by

$$E_x(\mathbf{r}) = U(z)e^{ik_0 y \cos\alpha}.$$

Substitution of the above equation into Eq. 2.12 gives

$$U''(z) + k^2 U(z) = 0, \tag{2.13}$$

where $k^2 = \xi^2 - k_0^2 \cos^2\alpha = k_0^2(\sin^2\alpha - 2\delta + 2i\beta)$. k is the magnitude of the z-component of X-ray wave vector in the medium. With a similar derivation, one can prove that the p-wave also satisfies Eq. 2.13, which is termed the Helmholtz equation [53].

For the reflectivity setup as illustrated in Fig. 2.1, the wave equation in the air and liquid would be, according to Eq. 2.13,

$$U''(z) + k_z^2 U(z) = 0, \qquad z \geq 0 \text{ in air,} \tag{2.14}$$

$$U''(z) + k_s^2 U(z) = 0, \qquad z \leq 0 \text{ in liquid,} \tag{2.15}$$

where $k_z = k_0 \sin \alpha$ and $k_s = \sqrt{k_z^2 - 4\pi\rho_s r_0}$ (assuming $\beta = 0$). A solution of Eqs. 2.14 and 2.15 is

$$U(z) = e^{-ik_z z} + re^{ik_z z}, \qquad z \geq 0 \text{ in air,} \tag{2.16}$$

$$U(z) = te^{-ik_s z}, \qquad z \leq 0 \text{ in liquid.} \tag{2.17}$$

The first and the second term in Eq. 2.16 represent the incident (traveling along $-z$-direction) and reflected waves (traveling along $+z$-direction), respectively. Eq. 2.17 only has one term (transmitted wave) since there is no wave traveling along $+z$-direction (see Fig. 2.1). Using the continuity conditions of the wave functions and their derivatives at $z = 0$ gives

$$1 + r = t,$$

$$k_z(1 - r) = k_s t,$$

which further leads to the Fresnel reflectance (r) and transmittance (t)

$$r = \frac{k_z - k_s}{k_z + k_s},$$

$$t = \frac{2k_z}{k_z + k_s}.$$

The squared-modulus of the reflectance r and transmittance t gives Fresnel reflectivity R and transmission T, respectively. As a function of momentum transfer $Q_z = |\mathbf{k_f} - \mathbf{k_i}| = 2k_0 \sin \alpha = 2k_z$, Fresnel reflectivity is given by

$$R_F(Q_z) = \left| \frac{Q_z - \sqrt{Q_z^2 - Q_c^2}}{Q_z + \sqrt{Q_z^2 - Q_c^2}} \right|^2, \tag{2.18}$$

where the subscript F represents Fresnel and $Q_c = 4\sqrt{\pi\rho_s r_0}$, which is termed the critical momentum transfer since total external reflection (e.g., $R_F(Q_z) = 1$) takes place when $Q_z \leq Q_c$. The critical angle $\alpha_c \simeq \sin \alpha_c = \frac{Q_c}{2k_0} = \sqrt{2\delta}$, which is consistent with Snell's law (see Eq. 2.5). One should notice that the critical angle α_c depends on the X-ray wavelength although the critical momentum transfer Q_c does not. For $Q_z \gg Q_c$ (large Q_z region), Eq. 2.18 reduces to

$$R_F(Q_z) \sim \left(\frac{Q_c}{2Q_z} \right)^4, \tag{2.19}$$

which is sometimes referred to Porod's Q_z^{-4} law.

According to Eq. 2.17, the wave function of the transmitted beam in the medium is $te^{-ik_s z} = te^{-iRe(k_s)z}e^{Im(k_s)z}$. Noticing that z is negative here, the intensity of the transmitted beam is reduced by a factor of $e^{2Im(k_s)z}$ after traveling the distance z. Therefore, the e-fold penetration depth is defined as $D = 1/[2Im(k_s)]$. Without the absorption one should notice that below the critical angle $(Q_z < Q_c)$, $Re(k_s) = 0$ and the transmitted wave, $te^{Im(k_s)z}$, is not a propagating wave. Total external reflection takes place when the wave does not propagate in $-z$-direction into the medium, which means that all photons must turn back into the incident space.

Taking the absorption into account here with $k_s = k_0\sqrt{\sin^2\alpha - 2\delta + 2i\beta}$ and using the fact $Im(\sqrt{a+ib}) = \frac{1}{\sqrt{2}}\sqrt{\sqrt{a^2+b^2}-a}$, one can get

$$D(\alpha) = 1/\left[2k_0 Im\left(\sqrt{\sin^2\alpha - \sin^2\alpha_c + 2i\beta}\right)\right]$$

$$= \left(1/\sqrt{2}k_0\right)\left\{\left[\left(\sin^2\alpha - \sin^2\alpha_c\right)^2 + 4\beta^2\right]^{1/2} + \sin^2\alpha_c - \sin^2\alpha\right\}^{-1/2}. \tag{2.20}$$

Figure 2.2 shows the penetration depth calculated from Eq. 2.20 for the pure water at two typical incident X-ray energies (8.0 and 16.2 keV) we used in the subsequent study.

For $\alpha \ll \alpha_c$ (the low-angle regime), the penetration depth becomes $D(\alpha) \simeq 1/Q_c$, which is virtually independent of wavelength of the incident X-rays but is dependent on Q_c, i.e., on the electron density of the subphase ρ_s. On the other hand for $\alpha \gg \alpha_c$ (the high-angle regime), the penetration depth is given by $D(\alpha) \simeq \sin\alpha/2k_0\beta = \sin\alpha/\mu$, which originates from the geometrical projection of the X-ray linear absorption length μ along the sample surface normal. One should notice that the penetration depth dramatically changes around the critical momentum transfer (Q_c; see Fig. 2.2), which is the advantage that can be taken in X-ray scattering techniques which shall be explained later in this thesis.

2.1.3 Reflectivity from a Graded Interface

2.1.3.1 Born Approximation (BA) and Distorted Wave Born Approximation (DWBA)

The Born approximation (BA) assumes that the scattered field is so small, compared to the incident field, that the scattered wave function is very close to the incident wave function.
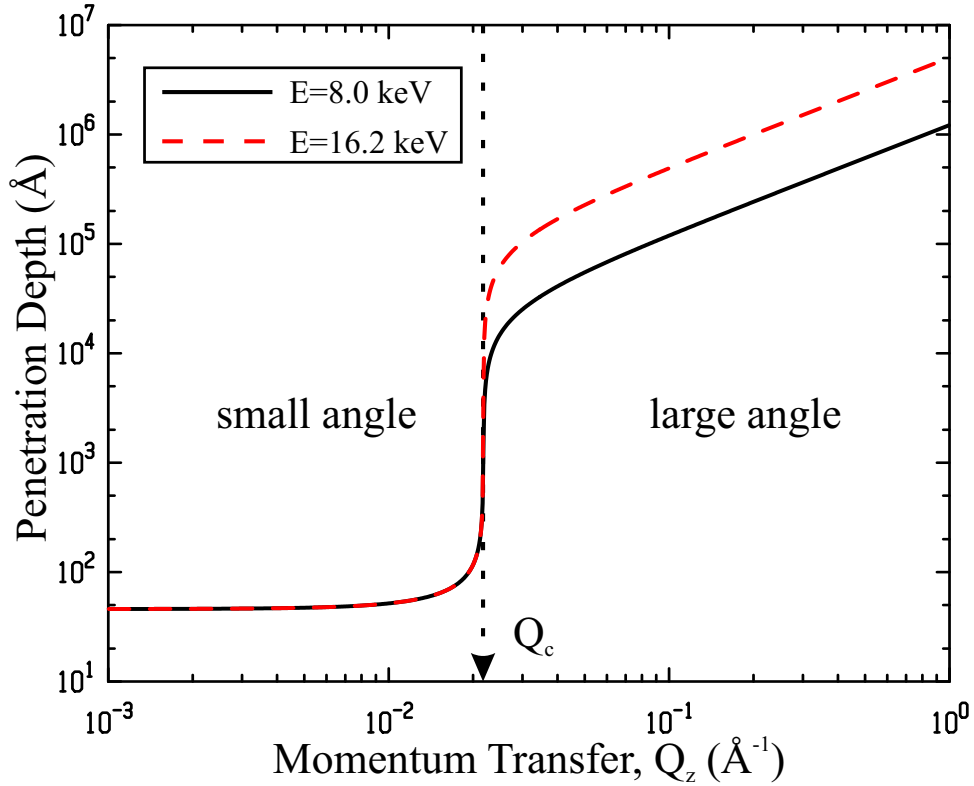
Figure 2.2   Penetration depth versus Q_z for the pure water at different incident X-ray energies as indicated. Arrow indicates the location of the critical angle.

Therefore, it is valid when single scatterings are dominant and multiple scatterings are negligible. In reflection, this could only happen at large Q_zs. According to this approximation, the reflectivity can be given as follows [53],

$$R(Q_z) = \left| \frac{4\pi r_0}{Q_z^2} \int \frac{d\rho(z)}{dz} \exp(-iQ_z z) dz \right|^2 , \qquad (2.21)$$

where $\rho(z)$ represents the electron density (ED) profile along z-direction. For an ideally flat surface ($\rho = \rho_s$ for $z < 0$ and $\rho = 0$ for $z > 0$; see Fig. 2.1), substituting the derivative of the step function, $d\rho(z)/dz = -\rho_s \delta(z)$, into Eq. 2.21 gives

$$R(Q_z) = 16\pi^2 \rho_s^2 r_0^2 / Q_z^4 = \left(\frac{Q_c}{2Q_z} \right)^4 , \qquad (2.22)$$

which agrees with the Fresnel reflectivity at large Q_zs (see Eq. 2.19).

Figure 2.3 shows comparison between the exact solution and the Born approximation for
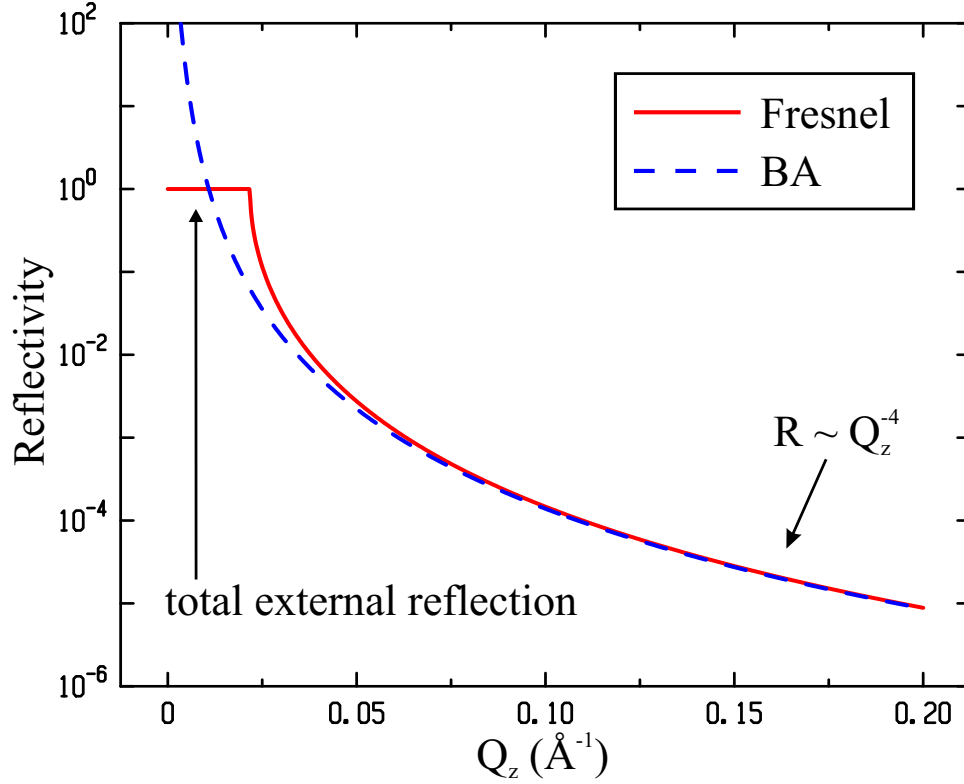
Figure 2.3   Fresnel reflectivity (solid line) and Born approximation (dashed line) for pure water with an ideally flat surface.

pure water with an ideally flat surface. As shown Fig. 2.3, BA matches the Fresnel reflectivity very well at large Q_zs, but fails at small Q_zs as it diverges instead of saturating at total reflection. That is due to the fact that the wave function is quite different from the incident wave function (see definitions of k_s and k_z) at small Q_zs, where multiple scatterings are dominant.

Due to the failure of the BA at small Q_zs, it is necessary to introduce a higher-order approximation known as the distorted wave Born approximation (DWBA), which accounts for multiple scatterings. According to the DWBA, the reflectivity can be obtained from the modification of Eq. 2.21 by multiplying the Fresnel transmission T for both incident and reflected beams as follows [54].

$$R(Q_z) = T^2 \left(\frac{Q_c}{2Q_z} \right)^4 \left| \frac{1}{\rho_s} \int \frac{d\rho(z)}{dz} \exp(-iQ_z z) dz \right|^2 . \tag{2.23}$$

Substituting $T = |t|^2 = \left| \frac{2Q_z}{Q_z + \sqrt{Q_z^2 - Q_c^2}} \right|^2$ into the Eq. 2.23 gives the reflectivity under DWBA

$$R(Q_z) = \left| \frac{Q_c}{Q_z + \sqrt{Q_z^2 - Q_c^2}} \right|^4 \left| \frac{1}{\rho_s} \int \frac{d\rho(z)}{dz} \exp(-iQ_z z) dz \right|^2$$

$$= \left| \frac{Q_z + \sqrt{Q_z^2 - Q_c^2}}{Q_z + \sqrt{Q_z^2 - Q_c^2}} \right|^2 \left| \frac{Q_z - \sqrt{Q_z^2 - Q_c^2}}{Q_z + \sqrt{Q_z^2 - Q_c^2}} \right|^2 \left| \frac{1}{\rho_s} \int \frac{d\rho(z)}{dz} \exp(-iQ_z z) dz \right|^2$$

$$= R_F(Q_z) \left| \frac{1}{\rho_s} \int \frac{d\rho(z)}{dz} \exp(-iQ_z z) dz \right|^2 . \tag{2.24}$$

One can readily find that Eq. 2.24 gives the exact Fresnel reflectivity $R_F(Q_z)$ for a step function ED profile.

2.1.3.2 Possible ED Profiles

The thicknesses and ED profiles of the liquid/gas interface have been investigated theoretically [55, 56, 57, 58, 59, 60] and experimentally [61, 62, 63] since about a century ago. Near the critical temperature of gas/liquid phase transition, the thickness of the interface varies from hundreds to thousands of Å [61, 62, 63], whereas, far below the criticality, the thicknesses can be reduced to several Å [64, 65]. Meanwhile, several possible ED profiles, such as, hyperbolic tangent function associated with mean field theory [55, 56] and error function associated with capillary wave theory [58], have been discussed to describe the interfacial structure. Nowadays, far below the criticality, the thickness of the interface is well understood by hybrid capillary wave model, which combines the intrinsic and capillary wave contributions. However, ED profile at the interface has been much less addressed and is still kind of open question.

Although there are several possible ED profiles theoretically, ED values far from the interface are constrained to two extreme values: ρ_0 and ρ_s, corresponding to the ED of the gas and the liquid, respectively. The interfacial profile is therefore written as

$$\rho(z) = \frac{1}{2} \left[(\rho_0 + \rho_s) + (\rho_0 - \rho_s) f(z) \right], \tag{2.25}$$

where f is a universal monotonic function such that $f(\pm\infty) = \pm 1$. Noticing that $\rho_0 = 0$ for the air ED, one can readily simplify Eq. 2.25 as

$$\rho(z) = \frac{\rho_s}{2} (1 - f(z)). \tag{2.26}$$

The simplest case is the ideally flat surface (zero interfacial thickness), which means the profile is a step function (i.e., $f(z) = sign(z)$, which gives 1 and -1 for $z > 0$ and $z < 0$, respectively.). And the corresponding X-ray reflectivity is so-called the Fresnel reflectivity as discussed above. However, the liquid/gas interface always has nonzero thickness, which induces the departure of the reflectivity from the Fresnel reflectivity.
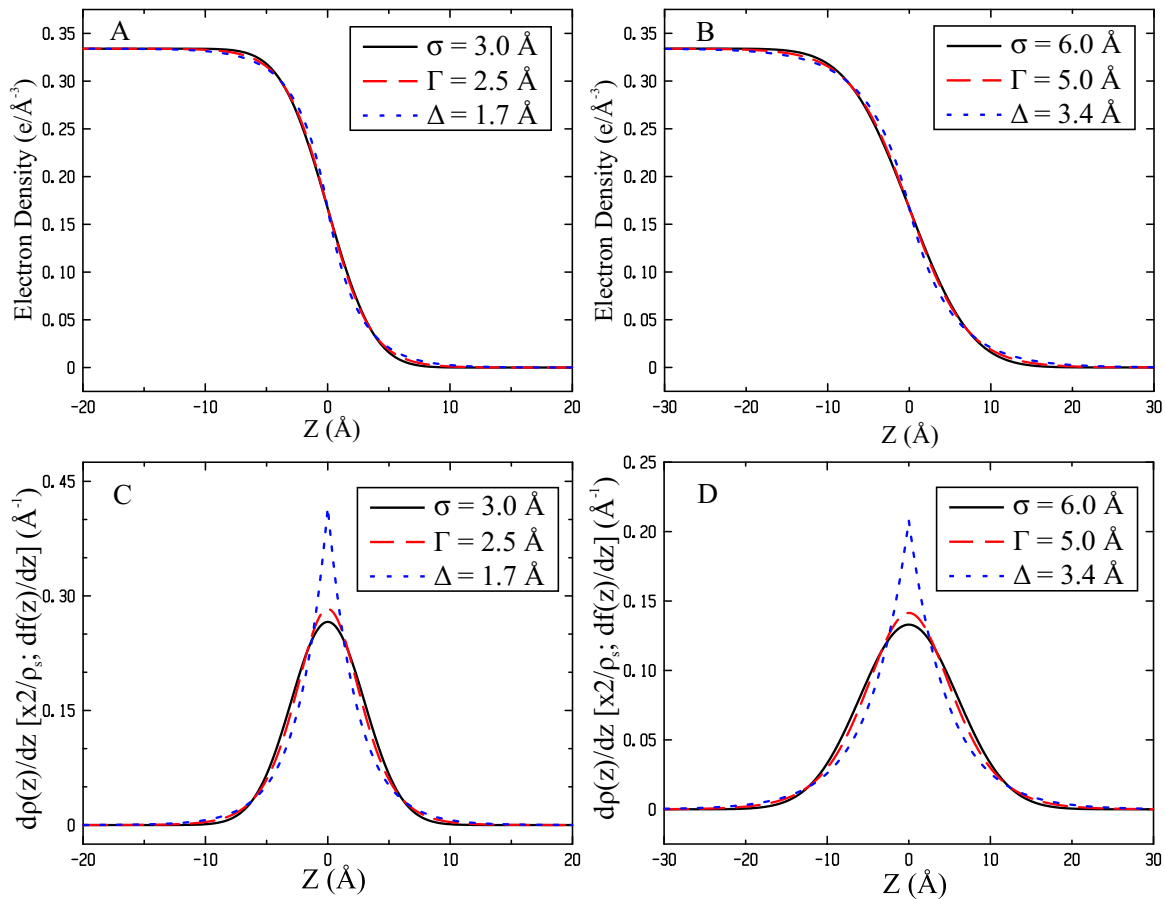
Figure 2.4   ED profiles constructed by three different functions with exchange length L of 3.0 Å in (A) and 6.0 Å in (B), respectively. Here, $\rho_s = 0.334 \, e/\text{Å}^3$ represents ED for the pure water. (C) and (D) are derivatives of corresponding ED profiles shown in (A) and (B), respectively.

The most common profile, first introduced by Buff, Lovett, and Stillinger [58], is the error function (ERF), $f(z) = \text{erf}(\frac{z}{\sqrt{2}\sigma})$, where σ is the surface roughness. However, the classical profile function arising from the van der Waals and Cahn-Hilliard theory [55, 56] gives a hyperbolic

tangent function (TANH), $f(z) = \tanh(\frac{z}{\sqrt{2}\Gamma})$. In this section, we mainly focus on these two common profiles. Moreover, for comparison, we include an exponential function (EXP), $f(z) = sign(z)(1 - \exp(\frac{-|z|}{\sqrt{2}\Delta}))$. Here, σ, Γ, and Δ represent the roughnesses for the different profile functions. The exchange length [62], defined by

$$L = \sqrt{\frac{\pi}{2}} \int_0^\infty (1 - f(z))dz, \tag{2.27}$$

which induces $L = \sigma = \ln 2\sqrt{\pi}\Gamma = \sqrt{\pi}\Delta$, gives the best basis for comparisons amongst profile functions. There are also some other profiles we do not discuss here, such as Fisk-Widom profile, which is nearly identical to the error function.

Figure 2.4(A) shows the ED profiles constructed from ERF (solid line), TANH (dashed line), and EXP (dotted line). $\sigma = 3.0\,\text{Å}$ for ERF is the typical value for a water/air interface at room temperature (RT). Using the same exchange length L for TANH and EXP ($\Gamma = 2.5\,\text{Å}$ and $\Delta = 1.7\,\text{Å}$) makes all three lines almost indistinguishable, which is still true for $L = 6.0\,\text{Å}$ as shown in Fig. 2.4(B). However, their derivatives, which determine the reflectivity according to DWBA, are quite different as shown in Fig. 2.4(C) and (D), especially for EXP.
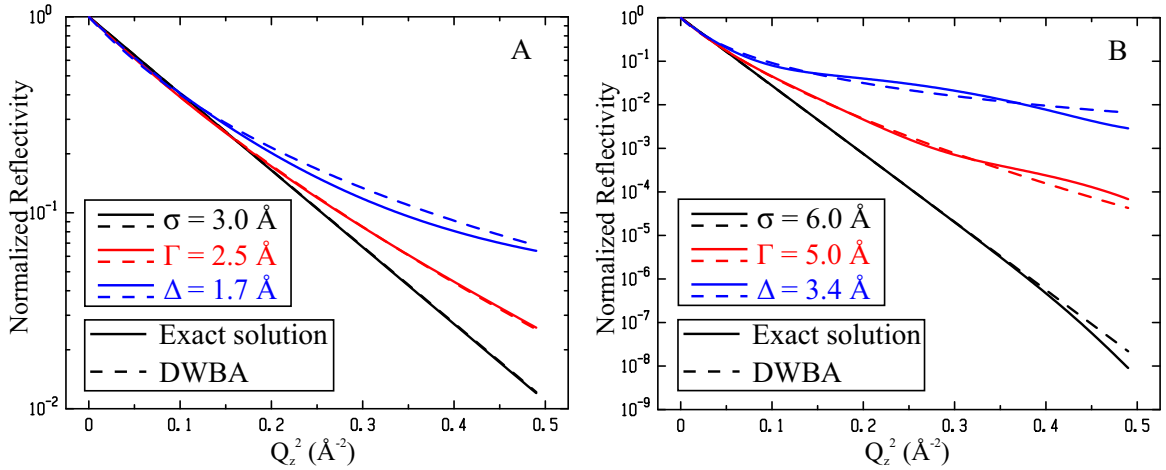
Figure 2.5   Calculated normalized reflectivities of corresponding ED profiles shown in Fig. 2.4 are plotted versus Q_z^2. Solid lines and dashed lines represent the exact solution and the distorted wave Born approximation, respectively.

Substitution of the derivatives of all three possible ED profiles (ERF, TANH, and EXP) into

Eq. 2.24 gives the normalized reflectivities as listed below:

$$\frac{R}{R_F} = \exp(-Q_z^2\sigma^2), \tag{2.28}$$

$$\frac{R}{R_F} = \left[\frac{\Gamma Q_z \pi}{\sqrt{2}\sinh(\frac{\Gamma Q_z \pi}{\sqrt{2}})}\right]^2, \tag{2.29}$$

$$\frac{R}{R_F} = \left[\frac{1}{1 + 2Q_z^2\Delta^2}\right]^2. \tag{2.30}$$

One should notice that all these normalized reflectivities, R/R_F, are independent on the sub-phase ED, ρ_s. The right-hand side of Eq. 2.28 is known as the Debye-Waller factor, which implies that a straight line is expected in a semi-log plot of R/R_F versus Q_z^2. Figure 2.5 shows normalized reflectivities calculated by the recursive dynamical method (exact solution as we shall discuss later in this thesis; solid lines) and DWBA (dashed lines) for the corresponding ED profiles shown in Fig. 2.4. Figure 2.5(A) shows that reflectivities calculated from these two different methods are indistinguishable for ERF and TANH ED profiles when $L = 3.0\,\text{Å}$. However, DWBA starts to fail for large L, especially at large Q_z, and does not work well for the EXP ED profile at all. Although the ED profiles associated with different construction functions have very close shapes shown in Fig. 2.4(B), the normalized reflectivities are significantly different, especially for $L = 6.0$ Å. Intensities for TANH and EXP ED profiles are about 4 and 6 orders larger than the one with ERF ED profile at large Q_z, respectively.

Table 2.2   Parameters that generate the best-fit calculated reflectivities to the experimental data in Fig. 2.6.

subphase	σ (Å)	Γ (Å)	σ/Γ
pure water	2.64	2.18	1.21
0.5% ethanol	2.93	2.43	1.20
50% ethanol	3.81	3.20	1.19
pure ethanol	4.36	3.62	1.21

As discussed above, a large roughness ($L > 3.0$ Å) is necessary to discriminate between the reflectivities of ERF and THAN ED profiles. Pure alcohol has a larger surface roughness (~ 4.4 Å) and lower surface tension ($\gamma \sim 22$ mN/m), compared to pure water ($\gamma \sim 73$ mN/m). Thus, water and ethanol mixtures have been used here for increasing the roughness gradually.
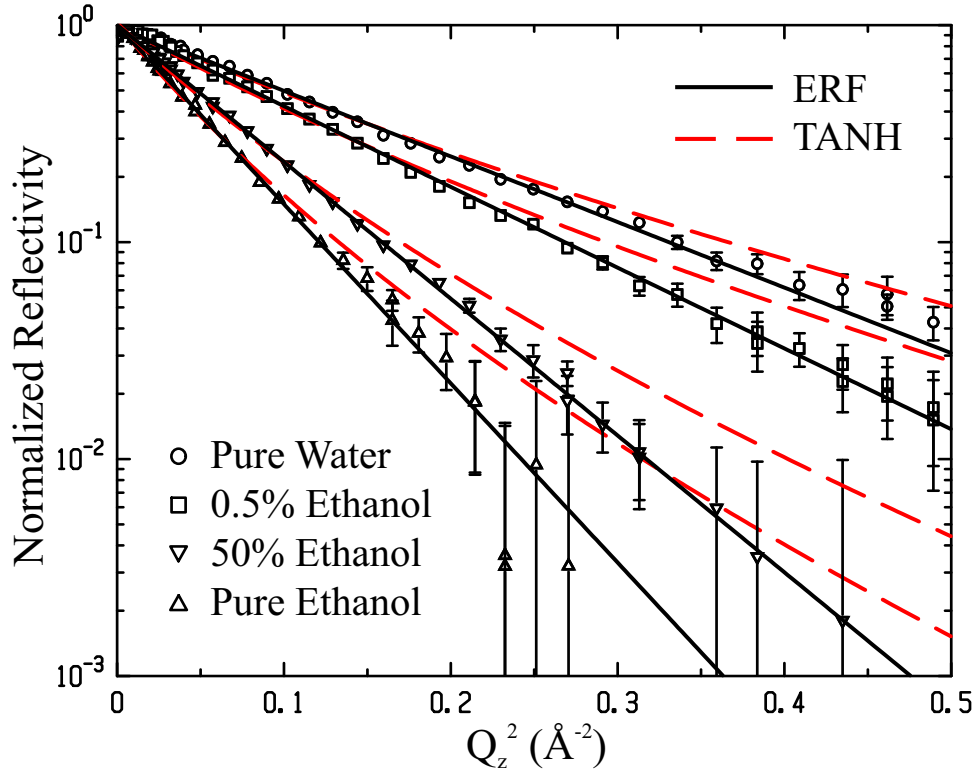
Figure 2.6   Normalized reflectivities (R/R_F) of pure water (circles), 0.5%
ethanol (squares), 50% ethanol (inverted triangles), and pure
ethanol (triangles). Solid and dashed lines are the best fits by
considering ERF and TANH as ED profiles, respectively.

Figure 2.6 shows normalized reflectivities of four different subphases. Solid and dashed lines
are the best fits calculated by Eq. 2.28 and Eq. 2.29, respectively. Calculations of recursive
dynamical method (exact solutions) did not show any significant difference. σ and Γ are the
only fitting parameters which are listed in Table 2.2. The ratios of σ and Γ shown in the forth
column of Table 2.2 are very close to the criterion ($\sigma/\Gamma = \ln 2\sqrt{\pi} \sim 1.23$ Å) for both ERF and
TANH having the same exchange length. In other words, ED profiles from the fitting results
based on ERF and TANH trend to be as close as possible.

In Table 2.2, we also observed that the interface roughness increases for the mole-fraction
or decreases for the surface tension, consistent with capillary wave theory as discussed later.
As shown in Fig. 2.6, for the pure water/air interface, it is hard to tell which fitting result is
better than the other one. However, as the roughness goes up, solid lines almost go through

every experimental data point, whereas dashed lines stray away from the data as Q_z goes up. Therefore, the TANH ED profile can be clearly ruled out.

2.1.3.3 Capillary Wave Theory and Off-specular Diffuse Scattering

Due to the rough surface, which is mainly induced by thermally excited capillary waves, the reflected beam can be even found under off-specular condition (e.g., $\alpha \neq \beta$ or $Q_{xy} \neq 0$; see Fig. 2.7), referred as X-ray diffuse scattering. The measured intensity, denoted by $I(\mathbf{Q}_{xy}, Q_z)$, is proportional to the integration of the differential cross section $d\sigma/d\Omega$ over the solid angle $d\Omega = d\mathbf{Q}_{xy}/(k_0^2 \sin\beta)$. Starting from DWBA and integrating over the experimental resolutions in reciprocal space [54, 64, 66, 67], the normalized scattering intensity can be expressed as

$$\frac{I(\mathbf{Q}_{xy}, Q_z)}{I_0} = \frac{T(\alpha)T(\beta)}{4Q_z^2 k_0^2 \sin\alpha \sin\beta} \left(\frac{Q_c}{2}\right)^4 \exp(-Q_z^2 \sigma_0^2) R(\mathbf{Q}_{xy}, Q_z), \quad (2.31)$$

where I_0 is the incident X-ray intensity and σ_0 is the intrinsic roughness. The dependence of observed intensity on the capillary wave roughness and the detector resolution is contained in the factor [67]

$$R(\mathbf{Q}_{xy}, Q_z) = \frac{1}{(2\pi)^2} \int d^2 \mathbf{Q}'_{xy} \Xi(\mathbf{Q}_{xy} - \mathbf{Q}'_{xy}) \times \int d^2 \mathbf{r}_{xy} e^{i\mathbf{Q}'_{xy} \cdot \mathbf{r}_{xy}} e^{-(1/2)g(\mathbf{r}_{xy})Q_z^2}, \quad (2.32)$$

where $\Xi(\mathbf{Q}_{xy} - \mathbf{Q}'_{xy})$ is the resolution function, which satisfies $\Xi(0) = 1$ and $\Xi \to 0$ well outside the resolution widths. The capillary wave (CW) fluctuations [54, 58, 64, 66, 67] cause the height-height correlation function $g(\mathbf{r}_{xy})$ to be given by a logarithmic form

$$g(\mathbf{r}_{xy}) = \left\langle [h(\mathbf{r}_{xy}) - h(0)]^2 \right\rangle \approx \frac{k_B T}{\pi\gamma} \ln(Q_{max} r_{xy}),$$

where γ is the surface tension and Q_{max} is the short CW wavelength cutoff.

Let $\eta = \frac{k_B T}{2\pi\gamma} Q_z^2$, one can solve the second integration on the right side of Eq 2.32 as follows:

$$\int d^2 \mathbf{r}_{xy} e^{i\mathbf{Q}'_{xy} \cdot \mathbf{r}_{xy}} e^{-(1/2)g(\mathbf{r}_{xy})Q_z^2}$$

$$= \int d^2 \mathbf{r}_{xy} e^{i\mathbf{Q}'_{xy} \cdot \mathbf{r}_{xy}} (Q_{max} r_{xy})^{-\eta}$$
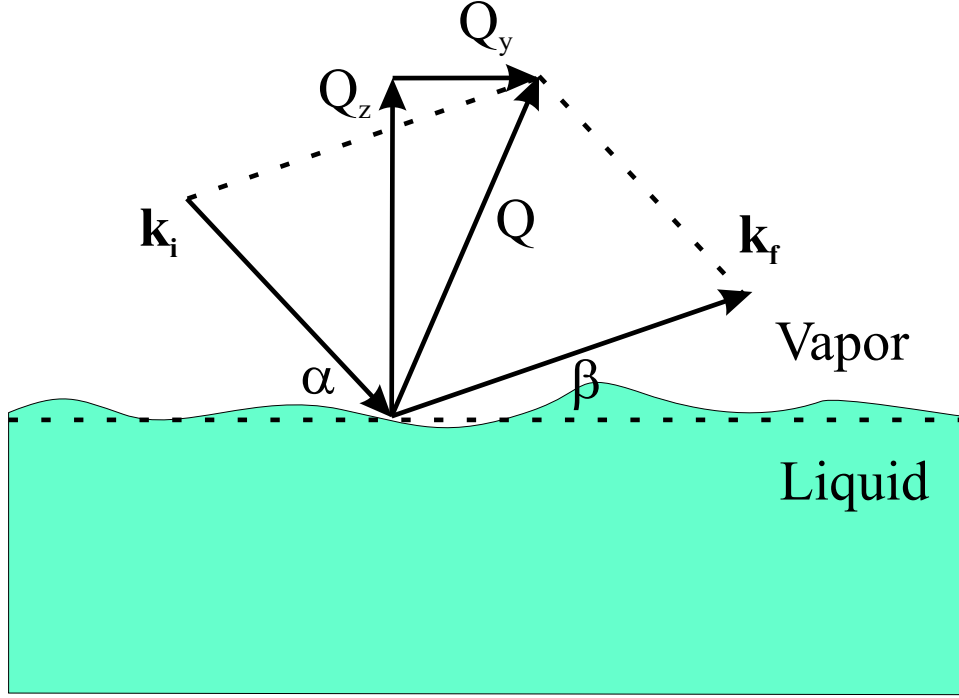
Figure 2.7   Schematic illustration of off-specular diffuse scattering.

$$= \int_0^\infty dr_{xy} r_{xy} (Q_{max} r_{xy})^{-\eta} \int_0^{2\pi} d\theta e^{iQ'_{xy} r_{xy} \cos\theta}$$

$$= \frac{2\pi}{Q'^2_{xy}} \left(\frac{Q'_{xy}}{Q_{max}} \right)^\eta \int_0^\infty d(Q'_{xy} r_{xy})(Q'_{xy} r_{xy})^{1-\eta} J_0(Q'_{xy} r_{xy})$$

$$= \frac{2\pi}{Q'^2_{xy}} \left(\frac{Q'_{xy}}{Q_{max}} \right)^\eta 2^{1-\eta} \frac{\Gamma(1-\eta/2)}{\Gamma(\eta/2)}. \tag{2.33}$$

In order to get the final $R(\mathbf{Q}_{xy}, Q_z)$, we need to integrate Eq. 2.33 with the resolution function $\Xi(\mathbf{Q}_{xy} - \mathbf{Q}'_{xy})$. Usually, the resolution function is infinitely wide along $\mathbf{Q}_x$, making Ξ only the function of Q_y, $\Xi(Q_y - Q'_y)$. Our slits configuration has a rectangular resolution function, which gives $\Xi(Q_y - Q'_y) = 1$ for $\left| Q_y - Q'_y \right| \leq \frac{1}{2}\Delta Q_y$ and $\Xi(Q_y - Q'_y) = 0$ otherwise. Substitution of this resolution function into Eq. 2.32 and using Eq. 2.33 gives

$$R(Q_y, Q_z) = \frac{2^{1-\eta}\Gamma(1-\eta/2)}{2\pi Q^\eta_{max}\Gamma(\eta/2)} \int dQ'_x \int_{Q_y - \Delta Q_y/2}^{Q_y + \Delta Q_y/2} dQ'_y (Q'^2_x + Q'^2_y)^{(\eta-2)/2}$$

$$= \frac{2^{-2\eta}((\Delta Q_y - 2Q_y)|\Delta Q_y - 2Q_y|^{\eta-1} + (\Delta Q_y + 2Q_y)|\Delta Q_y + 2Q_y|^{\eta-1})\Gamma(1/2 - \eta/2)}{Q_{max}^\eta \sqrt{\pi}\eta\Gamma(\eta/2)}, \quad (2.34)$$

where $\Delta Q_y = k_0 \sin \beta \Delta\beta \simeq \frac{Q_z^2 - 2k_0 Q_y}{2Q_z}\Delta\beta$ for small angles ($\Delta\beta$ is the detector acceptance angle).
Normalization of the intensity to unity at $Q_y = 0$ gives

$$R(Q_y, Q_z)/R(0, Q_z) = \frac{(\Delta Q_y - 2Q_y)|\Delta Q_y - 2Q_y|^{\eta-1} + (\Delta Q_y + 2Q_y)|\Delta Q_y + 2Q_y|^{\eta-1}}{2(Q_z\Delta\beta/2)^\eta}.$$
$$(2.35)$$

One should notice that Eq. 2.35 is independent of the short wavelength cutoff Q_{max}.

The real measured diffuse scattering intensity, which includes the background, should be presented as follows:

$$I_m(Q_y, Q_z) = f(Q_z)R(Q_y, Q_z)T(\alpha)T(\beta)/\sin\alpha + b(\alpha, \beta), \quad (2.36)$$

where $f(Q_z) = I_0 \frac{Q_c^4}{32k_0 Q_z^3}e^{-\sigma_0^2 Q_z^2}$, $\sin\alpha$ accounts for the change of the footprint, and b is the background which mainly comes from the bulk scattering. If the footprint of the incident beam is much smaller than the footprint of the detector slit, which is true for $Q_y > 0$ according to our setup, the background can be given by [68]

$$b = T(\alpha)T(\beta)\int_0^L \frac{A}{\sin\alpha}S(Q)e^{-z/D(\alpha)}e^{-z/D(\beta)}dz, \quad (2.37)$$

where L is the thickness of the sample, $S(Q)$ is the bulk scattering intensity per unit volume ($Q = \sqrt{Q_y^2 + Q_z^2} \simeq Q_z$), A is the cross section of the incident beam, and D is the penetration depth. For $L \gg D(\alpha), D(\beta)$, the background intensity can be simplified as

$$b = \frac{T(\alpha)T(\beta)}{\sin\alpha}AS(Q)D(\alpha, \beta), \quad (2.38)$$

with $D(\alpha, \beta) = \frac{D(\alpha)D(\beta)}{D(\alpha)+D(\beta)}$. For convenience, we define $I_n(Q_y, Q_z) = \frac{\sin\alpha I_m(Q_y,Q_z)}{T(\alpha)T(\beta)}$, which leads to

$$I_n(Q_y, Q_z) = f(Q_z)R(Q_y, Q_z) + AS(Q)D(\alpha, \beta).$$

Normalization to $I_n(0, Q_z)$ gives

$$\frac{I_n(Q_y, Q_z)}{I_n(0, Q_z)} = a\frac{R(Q_y, Q_z)}{R(0, Q_z)} + cD(\alpha, \beta), \quad (2.39)$$
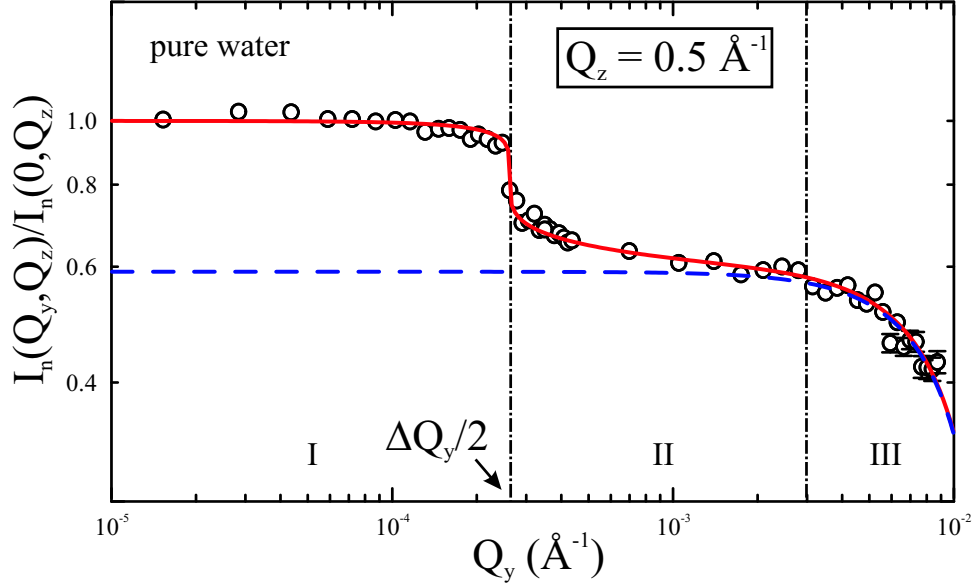
Figure 2.8   Rocking scan data (circles) represented by $I_n(Q_y, Q_z)/I_n(0, Q_z)$ for pure water at $Q_z = 0.5 \, \text{Å}^{-1}$. Solid line and dashed line are the best fit and background according to Eq. 2.39, respectively.

where $a = 1 - cD(\alpha, \alpha)$. Here, $c = AS(Q)/I_n(0, Q_z)$ is the only fitting parameter, which can also be determined experimentally at a small azimuthal angle away from the scattering plane for the specular reflectivity condition.

X-ray diffuse scattering data can be yielded from a rocking scan in the incidence plane ($Q_x = 0$), in which α and β are variable but $\alpha + \beta$ is constant. During a rocking scan, total $Q = 2k_0 \sin(\frac{\alpha+\beta}{2})$ is constant, and Q_z is constant as well since $Q_z = k_0(\sin\alpha + \sin\beta) \simeq Q$ for small angles. Therefore, the diffuse scattering is represented by the reflected beam intensity as a function of Q_y for a fixed Q_z.

Figure 2.8 shows the rocking scan (circles) for pure water at $Q_z = 0.5 \, \text{Å}^{-1}$. The background intensity (dashed line) is almost a constant except for the region III, where the difference between α and β is considerably large. Therefore, in the region I and II, the feature of $I_n(Q_y, Q_z)/I_n(0, Q_z)$ is mainly determined by $R(Q_y, Q_z)/R(0, Q_z)$. According to Eq. 2.35, one can readily find that, in the region I ($Q_y \ll \Delta Q_y/2$), $R(Q_y, Q_z)/R(0, Q_z) \simeq 1$, which gives the unity, whereas, in the region II ($Q_y \gg \Delta Q_y/2$), $R(Q_y, Q_z)/R(0, Q_z) \propto Q_y^{\eta-1}$, which gives power law.

2.1.3.4 Effective Roughness

According to Eqs. 2.31 and 2.34, the specular reflectivity ($\alpha = \beta$ or $Q_{xy} = 0$) can be expressed as

$$R(Q_z) = \frac{I(0, Q_z)}{I_0} = T(\alpha)^2 \left(\frac{Q_c}{2Q_z}\right)^4 \exp(-Q_z^2 \sigma_0^2) R(0, Q_z)$$

$$= R_F \exp(-Q_z^2 \sigma_0^2) \frac{2^{1-2\eta} \Gamma(1/2 - \eta/2)}{\sqrt{\pi} \eta \Gamma(\eta/2)} \left(\frac{\Delta Q_y}{Q_{max}}\right)^\eta.$$

In the Q_z-range of a typical reflectivity measurement ($< 0.8\ \text{Å}^{-1}$), η values are small and the specular reflectivity reduces to

$$R(Q_z) = R_F \exp(-Q_z^2 \sigma_0^2) \left(\frac{\Delta Q_y}{Q_{max}}\right)^\eta = R_F \exp(-Q_z^2 \sigma_{eff}^2), \tag{2.40}$$

where the effective roughness is

$$\sigma_{eff}^2 \equiv \sigma_0^2 + \sigma_{cw}^2 = \sigma_0^2 + \frac{k_B T}{2\pi\gamma} \ln\left(\frac{Q_{max}}{Q_{min}}\right), \tag{2.41}$$

with long CW wavelength cutoff $Q_{min} = \Delta Q_y = Q_z \Delta\beta/2$. One should notice that Eq. 2.40 gives the same specular reflectivity expression as DWBA (see Eq. 2.28) with the detailed definition of the roughness. In that definition (Eq. 2.41), the effective roughness σ_{eff} increases with the temperature (T), but decreases with the surface tension (γ). Moreover, it has weak logarithmic dependence on Q_z and two unknown parameters σ_0 and Q_{max}. Q_{max} has been usually estimated from the molecular size R such that $Q_{max} = \pi/R$ [64, 65, 66, 69]. On the other hand, σ_0 has had several interpretations: molecular size [64], atomic distance [65], or even zero [66, 69].

Equation 2.41 contains three physical quantities, which we can either control (T and $\Delta\beta$) or measure (γ). One should notice that Eq. 2.41 can be written as $\sigma_{eff}^2 = \sigma_0^2 + \frac{k_B T}{2\pi\gamma} \ln(Q_{max}) - \frac{k_B T}{2\pi\gamma} \ln(Q_{min})$, showing that the contribution of σ_0 and Q_{max} cannot be decoupled by varying the slit size ($\Delta\beta$). In other words, in order to find σ_0 and Q_{max}, we have to vary T and/or γ. Water and simple alcohols (methanol, ethanol, and propanol) mixtures could be good samples for this measurement since γ can be continuously varied over a wide range (22-73 mN/m at RT) by changing the mixture concentration [70]. The alcohol molecules are very close in size to a water molecule (in particular methanol), minimizing the presumed differences due to molecular size through σ_0 and/or Q_{max}.

The linear fits to the logarithm of reflectivities from the water-alcohol mixtures yield $\sigma_0 = 1.4 \pm 0.2$ Å and $Q_{max} = 0.09^{+0.06}_{-0.03}$ Å^{-1} [71]. The value of the intrinsic roughness $\sigma_0 = 1.4$ Å is very close to the bond lengths in our systems (e.g., C-C and C-O with bond lengths 1.53 and 1.43 Å, respectively), implying that σ_0 is on the order of the average interatomic distance. The shortest wavelength $l = \pi/Q_{max} = 35^{+17}_{-13}$ Å, which is about 3-7 molecular diameters, implies some rigidity of the surface over short length scales.

2.1.4 Reflectivity from Multiple Interfaces

Figure 2.9 shows N discrete uniform layers with different EDs between the air and the liquid subphase. The interface between layer i and layer $(i+1)$ is located at $z = z_i$. The ith layer has a thickness $d_i = z_{i-1} - z_i$ and z-component wave vector $k_i = k_0\sqrt{\sin^2\alpha - 2\delta_i + 2i\beta_i}$ (see Eq. 2.13). For convenience, we introduce a complex ED

$$\rho = \rho' - i\rho''$$

with $\rho' = \delta k_0^2/(2\pi r_0)$ and $\rho'' = \beta k_0^2/(2\pi r_0)$. The z-component wave vector for ith layer therefore can be written as

$$k_i = \sqrt{k_z - 4\pi r_0 \rho_i}.$$

One should notice that the z-component of wave vector in the air $k_{i=0} = k_z$ not k_0 (as shown in Fig 2.9), which has been used to define the amplitude of the X-ray wave vector in the vacuum.

The wave function in any uniform layer i satisfies the Helmholtz equation

$$U_i''(z) + k_i^2 U_i(z) = 0.$$

The solution of this equation can be written as

$$U_i(z) = A_i \left(e^{-ik_i(z-z_i)} + r_i e^{ik_i(z-z_i)} \right).$$

The continuity boundary conditions for the wave functions and their derivatives of ith and $(i+1)$th layer at $z = z_i$ give

$$A_i (1 + r_i) = A_{i+1} \left(e^{-ik_{i+1}d_{i+1}} + r_{i+1} e^{ik_{i+1}d_{i+1}} \right), \tag{2.42}$$
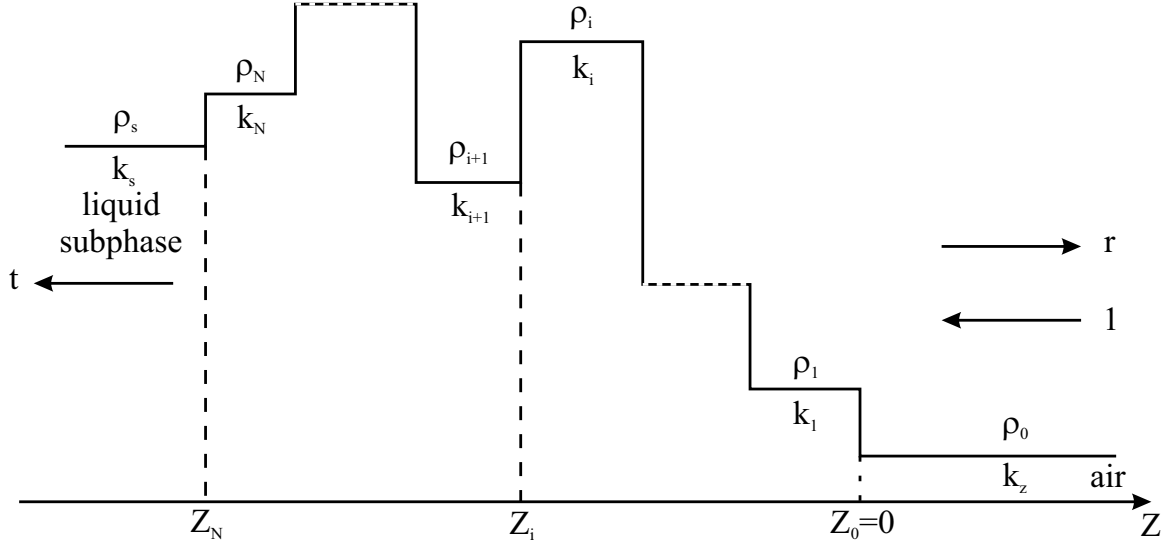
Figure 2.9   Illustration of N discrete layers between the air and the liquid
subphase.

$$k_i A_i \left(1 - r_i\right) = k_{i+1} A_{i+1} \left(e^{-ik_{i+1}d_{i+1}} - r_{i+1}e^{ik_{i+1}d_{i+1}}\right). \tag{2.43}$$

Division of Eqs. 2.42 into 2.43 gives

$$\frac{1 - r_i}{1 + r_i} = \frac{k_{i+1}}{k_i} \frac{1 - r_{i+1}e^{2ik_{i+1}d_{i+1}}}{1 + r_{i+1}e^{2ik_{i+1}d_{i+1}}},$$

leading to the final recurrence relation

$$r_i = \frac{R_i + r_{i+1}e^{2ik_{i+1}d_{i+1}}}{1 + R_i r_{i+1}e^{2ik_{i+1}d_{i+1}}}, \tag{2.44}$$

where $R_i = \frac{k_i - k_{i+1}}{k_i + k_{i+1}}$ is the Fresnel reflection coefficient of the interface between the ith and $(i+1)$th layer. One should notice that $r_{N+1} = 0$ since there is no interface below the subphase, which leads to $r_N = R_N = \frac{k_N - k_s}{k_N + k_s}$. Given ρ_i and d_i for $i = 1, 2, \ldots, N$, Eq. 2.44 can be used to calculate r_0, which is the reflection coefficient of the entire system. The method was first introduced by Parratt [72]. In this thesis, the reflectivity $|r_0|^2$ calculated from Eq. 2.44 is referred to the exact solution.

The interface between any two adherent layers is ideally flat in Fig. 2.9, however, the real ED profile is graded with an error function connecting the discrete layers as discussed above. In this thesis, the reflectivity from a graded ED profile is calculated by two models: the box

model and the sliced box model. Within the box model, we first calculate $|r_0|^2$ for the ED profile consisting of N discrete uniform boxes (layers) by using Eq. 2.44. Then, one can use the Debye-Waller factor to account for the effect of the error function smoothing the interface according to DWBA (see Eq. 2.28). Therefore, assuming that the roughness is a constant for each interface, the reflectivity for the box model is expressed as

$$R(Q_z) = |r_0|^2 \exp(-Q_z^2 \sigma^2).$$

In the sliced box model, we first construct the real complex ED profile $\rho(z) = \rho'(z) - i\rho''(z)$ by a sum of error functions as follows:

$$\rho(z) = \frac{1}{2} \sum_{i=0}^{N} \mathrm{erf}\left(\frac{z - z_i}{\sqrt{2}\sigma_i}\right)(\rho_i - \rho_{i+1}) + \rho_{N+1}/2, \qquad (2.45)$$

where N is the number of discrete boxes between the air and the liquid subphase, $\rho_{N+1} = \rho_s$, σ_i is the roughness at the interface between ith and $(i+1)$th layer, and the definition of the rest of parameters are shown in Fig. 2.9. Then, $\rho(z)$ is sliced into hundreds of thin slabs, in which the complex ED is almost constant. One can further apply Eq. 2.44 to these hundreds of thin slabs to calculate the reflectivity, $|r_0|^2$, which is the exact solution for a graded ED profile (solid lines in Fig. 2.5). The number of thin slabs is considered large enough if adding more slabs does not show any visible change for $|r_0|^2$.

2.2 Grazing Incidence X-ray Diffraction (GIXD)

As discussed above, X-ray reflectivity yields the out-of-plane (z-direction) structure (ED profile), we now consider the in-plane (xy-plane) structure. When surfactants are closely packed at the air/liquid interface, the hydrocarbon chains can be found in 2-D crystalline structure, which usually can be studied by grazing incident X-ray diffraction (GIXD) technique. GIXD measurements are performed at incident angles below (typically 90%) the critical angle. According to Eq. 2.17, the X-ray intensity in the medium can be written as

$$I(\alpha, z) = T(\alpha)e^{-|z|/D(\alpha)}.$$
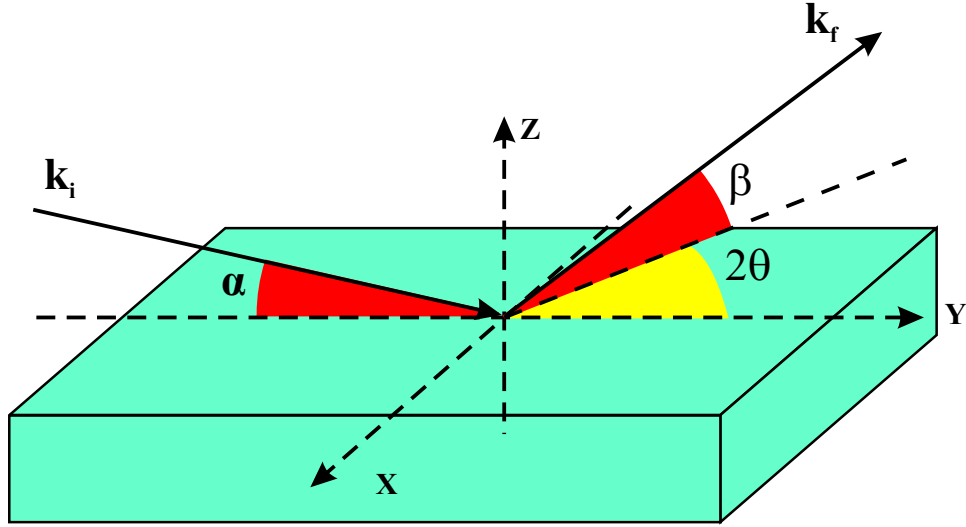
Figure 2.10   Setup for GIXD measurements. The incident beam hits the surface at a fixed angle α with respect to the liquid surface. The scattered beam is collected at an angle β with respect to the surface and at an angle 2θ with respect to the y-direction in the xy-plane.

Below the critical angle, the penetration depth $D(\alpha)$ is in the order of nanometers, rendering Bragg reflections only surface sensitive, which is exactly what we need for extracting the 2-D structure at the surface. Another advantage of GIXD is that the X-ray intensity just below the surface is amplified by a factor of four ($T(\alpha = \alpha_c) = 4$), and therefore the GIXD signal is very strong.

Figure 2.10 shows the setup for the GIXD measurement, which is 2θ scan at fixed α and β. As illustrated in Fig. 2.10, the components of the momentum transfer for GIXD are given by

$$Q_x = -k_0 \cos\beta \sin 2\theta,$$

$$Q_y = k_0 \left(\cos\beta \cos 2\theta - \cos\alpha\right),$$

$$Q_z = k_0(\sin\alpha + \sin\beta).$$

As of yet, there is no way of controlling the mosaicity of LM. In other words, the monolayers are powders within the xy-plane. The diffraction pattern is always averaged over all domain orientations in the monolayer plane. As a result, the lateral scans are usually represented in

terms of Q_{xy}, given by

$$Q_{xy} = \sqrt{Q_x^2 + Q_y^2} = k_0\sqrt{\cos^2\alpha + \cos^2\beta - 2\cos\alpha\cos\beta\cos 2\theta}.$$
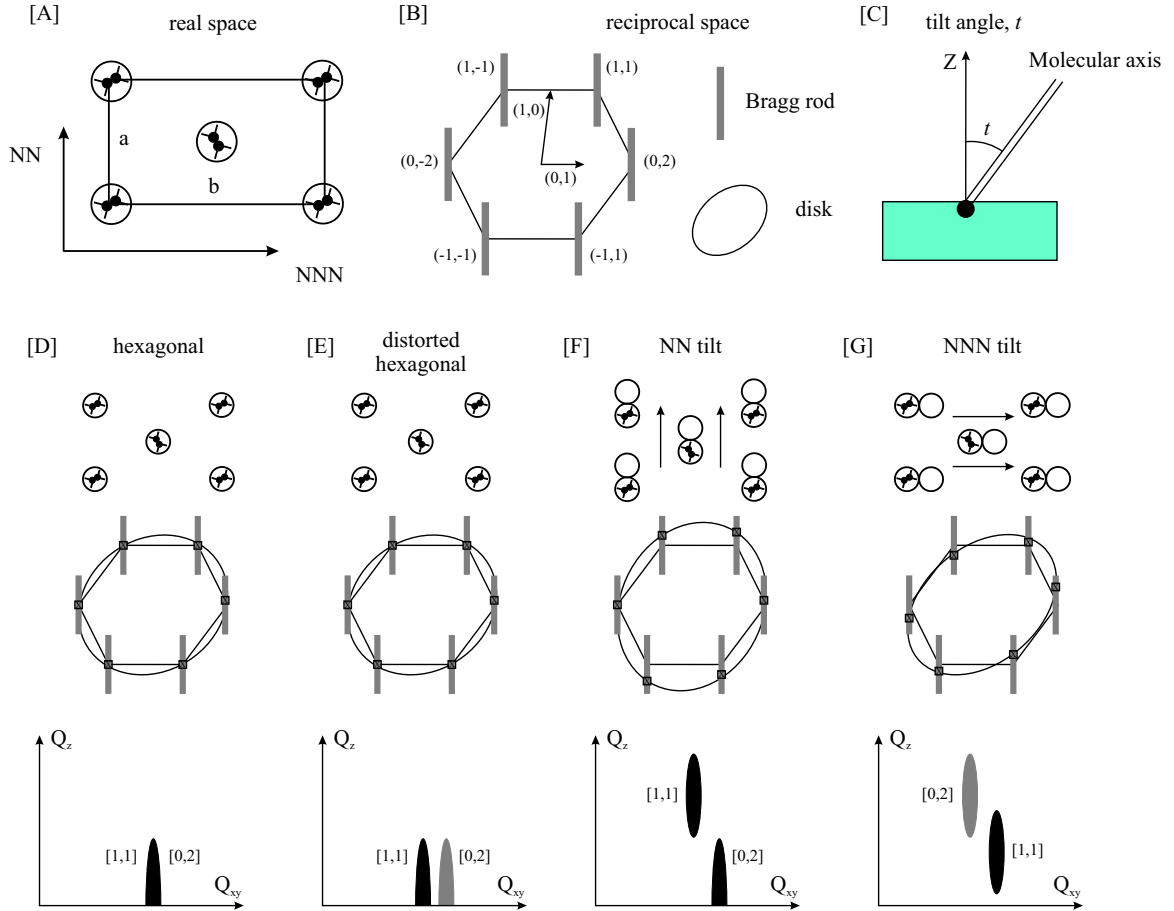
Figure 2.11 (A) Lattice structure in the real space. (B) Lattice structure in the reciprocal space, Bragg rod, and reciprocal disk. (C) Tilt angle, t, defined as the angle between the molecular axis and z-direction. (D-G) Real space (first row), reciprocal space (second row), and sketched diffraction pattern (third row) for four most general phases as indicated.

Assuming that the LM, consisting of uniformly oriented rigid molecules, has 2-D (quasi) long range order, the GIXD pattern usually is determined by two factors: the structure factor of the molecules in the plane of the LM and the form factor of the individual molecule. The structure factor of a 2-D lattice consists of a set of Bragg rods along z-direction, unlike the Bragg points for a 3-D crystal. The form factor of a rod-shaped molecule has its maximum at

a reciprocal disk perpendicular to the molecular axis. The intersections of the Bragg rods with the reciprocal disk give rise to diffraction maxima. If the molecular axis is not normal to the surface (i.e., molecules are tilted), some diffraction maxima will be out-of-plane (i.e., $Q_z \neq 0$). The technique used to find these diffraction maxima is β scan at specific 2θ, which is also called rod scan. In summary, the GIXD yields the diffraction pattern versus Q_{xy} at $Q_z = 0$, whereas, the rod scan yields the diffraction pattern versus Q_z at a specific Q_{xy}. The entire diffraction pattern, consisting of rod scans at each Q_{xy}, can be obtained by the position sensitive detector (PSD) with only one GIXD scan as shown later.

In most cases, the LM shows a centered rectangular structure in real space as shown in Fig. 2.11(A). The distances between nearest neighbors (NN) and next NN (NNN) are a and b, respectively. Figure 2.11(B) shows the corresponding structure in reciprocal space and two reciprocal primitive vectors (1,0) and (0,1), with length of $\frac{2\pi}{a}$ and $\frac{2\pi}{b}$, respectively. Because lattice fluctuations cause the peak intensities to decay rapidly with increasing momentum transfer Q_{xy}, in most cases, one can only observe six first order peaks ((1,1), (1,-1), (0,-2), (-1-1), (-1,1), (0,2)). One can readily find that wave vectors (1,1), (1,-1), (-1,-1), and (-1,1) have equal length $\frac{2\pi}{ab}\sqrt{a^2 + b^2}$, and wave vectors (0,2) and (0,-2) have equal length $\frac{4\pi}{b}$. Herein, we use [1,1] to represent vectors having length $\frac{2\pi}{ab}\sqrt{a^2 + b^2}$, which has fourfold degeneracy, and use [0,2] to represent vectors having length $\frac{4\pi}{b}$, which has twofold degeneracy. In diffraction patterns, these degeneracies can either be broken or further degenerated depending on the molecular phases. In most of our experiments, the most common phases include two untilted phases (hexagonal, see Fig. 2.11(D); distorted hexagonal, see Fig. 2.11(E)) and two tilted phases (NN tilt, see Fig. 2.11(F); NNN tilt, see Fig. 2.11(G)).

For untilted phases, the reciprocal disk is normal to the z-direction, and the maxima of six first order peaks are all in-plane ($Q_z = 0$) as shown in the second row of Fig. 2.11(D) and (E). The hexagonal structure can be obtained from the centered rectangular structure when $b = \sqrt{3}a$. In this case, wave vectors [1,1] and [0,2] have the same length $\frac{4\pi}{b}$, implying that only one sixfold peak can be observed in the diffraction pattern, as shown in the third row of Fig.

2.11(D). The molecular area in the xy-plane is given as

$$A = \frac{1}{2}abn = n\frac{b^2}{2\sqrt{3}} = n\frac{8\pi^2}{\sqrt{3}Q_{xy}^2},$$ (2.46)

where Q_{xy} is the peak position along xy-direction and the factor of $\frac{1}{2}$ is due to the fact that each cell has two molecules (see Fig. 2.11(A)). One should note that Fig. 2.11(A) actually shows the structure of the hydrocarbon chains, not the LM molecules. Therefore, n in Eq. 2.46 is the number of chains that each molecule has.

This sixfold symmetry can be broken when the lattice is distorted from the hexagonal structure. The most common distorted hexagonal structure in our experiments is the centered rectangular structure where $b \neq \sqrt{3}a$. Now, wave vectors [1,1] and [0,2] have different lengths, inducing two peaks in the GIXD pattern as shown in third row of Fig. 2.11(E). The fourfold and twofold degeneracy result in different intensities, indicated by the peak [1,1] in black and [0,2] in gray, respectively. Using $Q_{xy}[1,1] = \frac{2\pi}{ab}\sqrt{a^2 + b^2}$ and $Q_{xy}[0,2] = \frac{4\pi}{b}$, the molecular area is given by

$$A = n\frac{4\pi^2}{Q_{xy}[0,2]\sqrt{Q_{xy}^2[1,1] - Q_{xy}^2[0,2]/4}}.$$ (2.47)

One can readily find that $b > \sqrt{3}a$ yields $Q_{xy}[1,1] > Q_{xy}[0,2]$ and $b < \sqrt{3}a$ yields $Q_{xy}[1,1] < Q_{xy}[0,2]$, the one shown in Fig. 2.11(E).

The symmetry can also be broken by the hydrocarbon chains' tilt. Two most common tilted phases are NN tilt and NNN tilt, which induce the centered rectangular structure in xy-plane (usually $b < \sqrt{3}a$ for NN tilt and $b > \sqrt{3}a$ for NNN tilt). Therefore, Eq. 2.47 can still be used to calculate the molecular area for tilted phases. The tilt angle is defined as the angle between the molecular axis and the z-direction as shown in Fig. 2.11(C), which is also equal to the angle between the reciprocal disk and the xy-plane. Therefore, only peaks whose corresponding wave vector is perpendicular to the tilt direction is still in-plane. For NN tilt, only two peaks [0,2] still remain in the xy-plane, and four other peaks [1,1] are out-of-plane: two upwards and two downwards (see the second row of Fig. 2.11(F)). The third row of Fig. 2.11(F) shows the diffraction pattern sketched for the NN tilt phase. NN tilt induces $b < \sqrt{3}a$, which further induces $Q_{xy}[1,1] < Q_{xy}[0,2]$. As discussed above, peaks [1,1] are out-of-plane,

Table 2.3   Molecular area A in the xy-plane for molecules containing n hydrocarbon chains and tilt angle t. H, DH, NN, and NNN represent hexagonal, distorted hexagonal, NN tilt, and NNN tilt phases, respectively.

	A	$\tan t$
H	$n\dfrac{8\pi^2}{\sqrt{3}Q_{xy}^2}$	0
DH	$n\dfrac{4\pi^2}{Q_{xy}[0,2]\sqrt{Q_{xy}^2[1,1]-Q_{xy}^2[0,2]/4}}$	0
NN	$n\dfrac{4\pi^2}{Q_{xy}[0,2]\sqrt{Q_{xy}^2[1,1]-Q_{xy}^2[0,2]/4}}$	$\dfrac{Q_z[1,1]}{\sqrt{Q_{xy}^2[1,1]-Q_{xy}^2[0,2]/4}}$
NNN	$n\dfrac{4\pi^2}{Q_{xy}[0,2]\sqrt{Q_{xy}^2[1,1]-Q_{xy}^2[0,2]/4}}$	$\dfrac{Q_z[0,2]}{Q_{xy}[0,2]}$

and peaks $[0,2]$ are in the xy-plane. However, they have similar intensity since both of them have twofold degeneracy (two $[1,1]$ peaks' maxima having negative Q_z values cannot be observed). The tangent of tilt angle is given by

$$\tan t = \frac{Q_z[1,1]}{\sqrt{Q_{xy}^2[1,1] - Q_{xy}^2[0,2]/4}}. \tag{2.48}$$

For the NNN tilt phase, all six peaks are out-of-plane (see the second row of Fig. 2.11(G)) since no wave vector is perpendicular to the tilt direction. As shown in the sketched pattern (the third row of Fig. 2.11(G)), $Q_{xy}[1,1] > Q_{xy}[0,2]$ due to the fact that $b > \sqrt{3}a$, and all of the peak's maxima have finite Q_z. The intensity ratio is about 2:1 between $[1,1]$ and $[0,2]$ peaks since only one $[0,2]$ peak and two $[1,1]$ peaks can be observed. The tangent of tilt angle can be expressed as

$$\tan t = \frac{Q_z[0,2]}{Q_{xy}[0,2]}.$$

In brief, Table 2.3 shows the molecular area A and tilt angle t for all four different phases. The projection of the molecular area to the plane normal to the molecular axis is given by $A' = A\cos t$. Figure 2.12 shows the experimental GIXD data collected by PSD for the hexagonal and NN tilt phases.
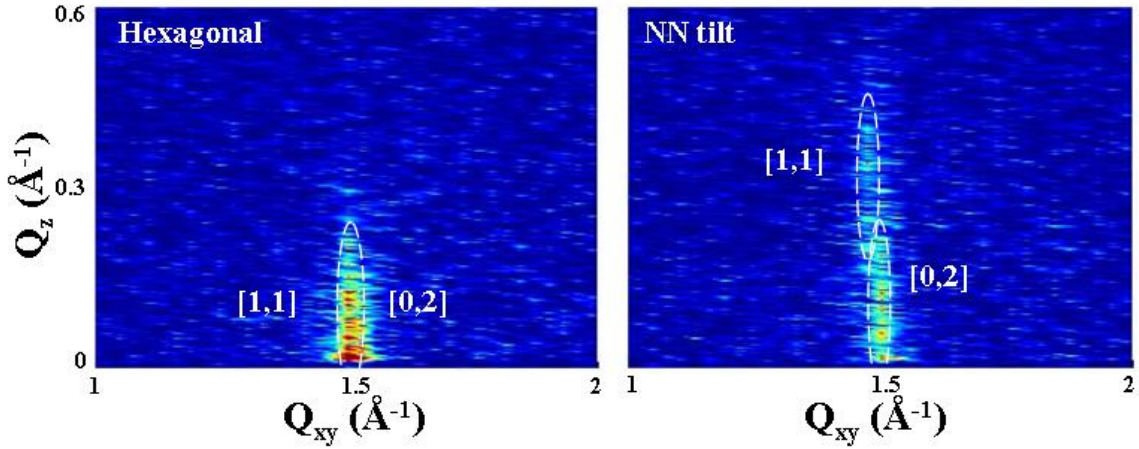
Figure 2.12 Experimental GIXD data for different phases as indicated.

2.3 X-ray Spectroscopy

2.3.1 Anomalous Reflectivity

In the general case, X-ray reflectivity is determined by the complex ED profile $\rho = \rho' - i\rho''$ with $\rho' = \delta k_0^2/(2\pi r_0)$ and $\rho'' = \beta k_0^2/(2\pi r_0)$. This complex ED profile is not only determined by the system (i.e., ion and atom arrangements acrose the interface), but also by the X-ray photon energy. In detail, it is given by

$$\rho(z, E) = \sum_j N_j(z) Z_j f_j(E),$$

where E is the X-ray photon energy and N_j is the number density of an atomic constituent of type j with Z_j electrons. The atomic form factor, $f(E)$, is defined as

$$f(E) = f^0(\mathbf{Q}) + f'(E) + i f''(E),$$

which consists of $\mathbf{Q}$ dependent term $f^0(\mathbf{Q})$, and real and imaginary parts of the dispersion corrections, $f'(E)$ and $f''(E)$, which are only energy dependent. $f^0(\mathbf{Q})$, called Thomson scattering atomic form factor, is the Fourier transform of the charge distribution normalized by the total electrons in an atom, and is given by

$$f^0(\mathbf{Q}) = \frac{1}{Z} \int \rho_e(\mathbf{r}) e^{i\mathbf{Q} \cdot \mathbf{r}} d\mathbf{r},$$

where $\rho_e(\mathbf{r})$ is electron density distribution for a given atom. In the limit that $Q \rightarrow 0$, all of the different volume elements scatter in phase so that $f^0(\mathbf{Q} = 0) = 1$. For our X-ray reflectivity experiments, the momentum transfer $(Q = Q_z)$ is so small that $f^0 \simeq 1$ is a good approximation.

The origin of f' and f'' can be described as follows. Atomic electrons have discrete energy levels with the binding energies defined as the energy difference between these discrete levels and the Fermi level. For the electrons (e.g., K shell) whose bonding energies are much higher than X-ray photon energy, the response of these electrons to an external driving field is reduced. Electrons in shells that are less tightly bound (L, M, etc) will response more closely, but overall it is expected that the scattering length of an atom will be reduced by some amount, which is denoted by $f'(E)$. At photon energies much higher than all binding energies, the electrons can be treated as if they are free and $f' = 0$. On the other hand, f'' represents the dissipation in the system, or in other words the absorption, which can be related with f' by Kramers-Kronig relations,

$$f'(E) = \frac{2}{\pi} P \int_0^{+\infty} \frac{E' f''(E')}{E'^2 - E^2} dE' \tag{2.49}$$

$$f''(E) = -\frac{2E}{\pi} P \int_0^{+\infty} \frac{f'(E')}{E'^2 - E^2} dE', \tag{2.50}$$

where the P in front of the integral stands for "principal value". In most cases, $f'(E)$ and $f''(E)$ only change dramatically when E is close to the binding energies (i.e., resonance, absorption edge). One should note that our sign convention for f'' is negative, but it is positive in some literature, where the refractive index is defined as $n = 1 - \delta - i\beta$.

Anomalous reflectivity consists of two reflectivities at and away from the resonance of the probed element, usually one specific ion in the solution. With this technique, the ED profile across the interface at each energy is determined, and from their differences the contribution of the probed ions is extracted. The advantage of this approach is that it determines the location and distribution specifically of those ions whose absorption edge is being probed. Herein, we introduce the effective number of electrons $Z_{j,eff}$, given by

$$Z_{j,eff} = Z_j(1 + f'_j(E)). \tag{2.51}$$

In general case, the photon energy away from the resonance of the probed ions in the anomalous

reflectivity is high enough for all elements in the system to have $Z_{j,eff} \simeq Z_j$. At the resonance, only ions whose absorption edge is being probed have significantly different Z_{eff} and other elements in the system still have almost the same Z_{eff} as the one at high energy. The distribution of the probed ions therefore is

$$N_{ion}(z) = \frac{ED_{off-res}(z) - ED_{res}(z)}{\Delta Z_{eff}},$$

where ΔZ_{eff} is the change of Z_{eff} between off-resonance and resonance energy.

2.3.2   Energy Scan at Fixed Momentum Transfers

All of the reflectivity experiments mentioned above are conducted at a fixed incident photon energy. Now, we introduce a different X-ray reflectivity technique, in which the momentum transfer Q_z is fixed and the reflected beam intensity is presented as a function of incident photon energy. Usually, the incident photon energy is scanned around one absorption edge of the probed ions ($\sim \pm 50$ eV). In this energy range, atomic form factor f is energy independent for all elements except for the probed ions, which have dramatic energy dependence instead. Therefore, the complex ED profile can be written as

$$\rho(z, E) = \sum_{j \neq ion} \rho_j + N_{ion}(z)Z_{ion}(1 + f'_{ion}(E) + f''_{ion}(E)).$$

Simultaneously fitting energy scans at different Q_zs can yield ion distribution $N(z)$ and dispersion corrections $f(E)$ for the probed ions. In the real fitting process, we treat $f''_{ion}(E)$ as a free parameter and $f'_{ion}(E)$ is numerically calculated by Eq. 2.49.

2.3.3   X-ray Fluorescence

Each element has discrete and characteristic energy levels. Electrons in the lower (inner) levels can be removed if the atom is exposed to the X-ray with high enough energy. Electrons in the higher (outer) level fall into the lower level to fill the hole left behind. In falling, energy is released in the form of a photon whose energy is equal to the energy difference of the two levels involved. This phenomena is called fluorescence, and this can happen in a limited number of transitions. Each transition is corresponding to a emission line (energy), which is also

characteristic for each element. Figure 2.13 shows most readily observable transitions of L shell emission lines. For the heavy element, the emission line energy is sorted in the following order

$$Ll < L\alpha_2 < L\alpha_1 < L\beta_1 < L\beta_2 < L\gamma_1,$$

and the emission line intensity is sorted by

$$L\alpha_1 > L\beta_1 > L\beta_2 > L\gamma_1 > Ll.$$

One should note that $L\alpha_1$ and $L\alpha_2$ are usually so close that it is hard to distinguish them with the resolution of our detector, and emission lines from L_I shell are either too weak to be observed or mixed with $L\beta_1$.
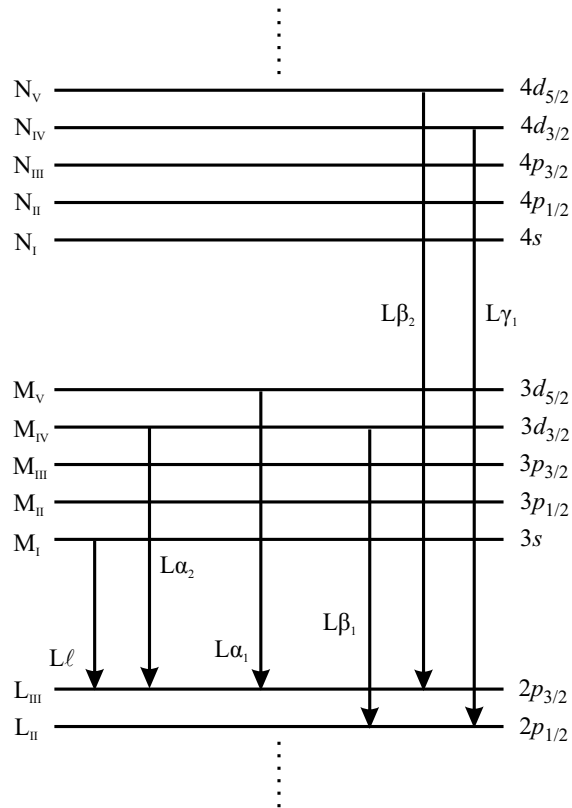
Figure 2.13   Schematic electron transition processes for the emission lines from L shell.

Since the emission line intensity is related to the amount of the element in the system, fluorescence is a useful technique in distinguishing contributions from different atoms or ions

because of their characteristic fluorescence spectra. In this thesis, the fluorescence technique has been used to qualitatively and quantitatively analyze the specific ion next to the charged surface. According to the fact that the X-ray penetration depth changes dramatically around the critical angle for the total reflection (from $60 - 80$ Å to $1 - 2$ μm; see Fig. 2.2), the fluorescence data below and above the critical angle have different origins. Below the critical angle, only ions at the surface contribute to the fluorescence intensity due to very short penetration depth. On the other hand, above the critical angle, the fluorescence data includes contributions from the ions both at the surface and in the bulk.

In most cases, for dilute salt solutions ($\leq 10^{-3}$M), the fluorescence pattern below the critical angle does not show any characteristic emission lines from any ions. However, one or more specific kinds of ions can have higher concentration at the surface when the surface is charged, which is usually high enough to show some emission lines in the fluorescence pattern even below the critical angle. Therefore, X-ray fluorescence below the critical angle can be used to directly detect the accumulation of specific ions near the charged surface. The charged surface can be obtained by spreading the monolayer molecules with charged headgroup on the surface.

The amount of specific ions per charged monolayer molecule at the surface can be extracted as follows. Fluorescence pattern above the critical angle includes the contributions from the surface and the bulk. As discussed before, above the critical angle, X-ray intensity at z in the solution is given by $I(z) = I_0 e^{-|z|/D(\alpha)}$. Assuming the fluorescence intensity (e.g., $L\alpha$ emission line intensity) from one ion at z is $CI(z)$ (C is a scale factor, which is determined by the experimental condition), the fluorescence intensity collected by the detector from the surface (I_s) and the bulk (I_b) can be written as,

$$I_s = CI_0 A N_{ion}/A_{lipid}, \tag{2.52}$$

and

$$I_b = CI_0 A n_b \int_0^\infty e^{-|z|/D(\alpha)} dz = CI_0 A n_b D(\alpha), \tag{2.53}$$

where A is the detector area, N_{ion} is the number of ions per lipid, A_{lipid} is the molecular area, and n_b is the ion bulk concentration. I_b can be obtained from the fluorescence data of the

pure solution without the monolayer, while I_s can be obtained from the fluorescence data of the solution with the monolayer after the subtraction of I_b. Using Eqs. 2.52 and 2.53, one can readily get the number of ions per molecule at the surface,

$$N_{ion} = \frac{I_s(\alpha)}{I_b(\alpha)} A_{lipid} D(\alpha) n_b. \tag{2.54}$$

The absorption of emission lines due to the solution is usually negligible.

CHAPTER 3.   EXPERIMENTAL SETUPS AND DETAILS

3.1   X-ray Source

The minute sizes of interfacial samples on the sub-micro-gram level, combined with weak interaction of X-rays with matter, result in very weak GIXD and reflectivity (at large Q_z) signals that require highly intense incident beams, which are available at X-ray synchrotron sources. A well prepared incident beam at a synchrotron has an intensity of 10^9 to 10^{11} counts per second (cps), whereas, an Ultra-X18 Rigaku X-ray source generator at 18-kW produces 10^4 to 10^5 cps. Although reflectivity measurements can be performed with rotating anode X-ray generators, the measurements are limited to almost half the angular range accessible at synchrotron sources, and they take hours to complete, compared to minutes at the synchrotron. GIXD experiments are practically impossible with X-ray generators, since the expected signals normalized to the incident beam are on the order of 10^{-8} to 10^{-10}.

"Third-generation" light sources at the Advanced Photon Source (APS) at Argonne National Lab, which provide high-brilliance and highly monochromatic X-ray beams, have been used in most of the experiments in this thesis. At the APS, producing brilliant X-ray beams begins with electrons emitted from a cathode heated to $\sim 1100°C$ (2,000°F), which are further accelerated to 450 MeV by high-voltage alternating electric fields in a linear accelerator. At 450 MeV, the electrons are relativistic: they are traveling at >99.999% of the speed of light. From the linear accelerator, the electrons are injected into the booster synchrotron. Here, the electrons are sent around an oval racetrack of electromagnets, providing further acceleration. Within one-half second, the electrons are accelerated from 450 MeV to 7 GeV and reach 99.999999% of the speed of light. Upon reaching this speed, the electrons are injected into the storage ring, a 1,104 meter circumference ring of more than 1,000 electromagnets and associated equipment, located

in a radiation-proof concrete enclosure inside the experiment hall

Once in the storage ring, the electrons produce X-ray beams that are available for use in experimentation. Around the ring are 40 straight sections. One of these sections is used to inject electrons into the ring, and four are dedicated to replenishing the electron energy lost though X-ray emission by using 16 radio-frequency accelerating cavities. The remaining 35 straight sections can be equipped with insertion devices (ID). Insertion devices, arrays of north-south permanent magnets usually called "undulators", cause the electrons to oscillate and emit light in the invisible part of the electromagnetic spectrum. In the 6-ID sector, location of our liquid surface diffractometer, X-ray energy can be continuously varied from $\sim$ 4 to 40 keV with the energy resolution $\sim$ 1 eV, and intensity can reach as high as $\sim 10^{10}$ cps at our two typical working energies: 8 keV and 16.2 keV.

3.2   Liquid Surface Diffractometer

X-ray reflectivity and GIXD measurements from the liquid surface require a special design of the instrument. A prototype liquid surface reflectometer was first introduced by Als-Nielsen and Pershan [73]. Figure 3.1 shows a side view diagram of the Ames Laboratory Liquid Surface Diffractometer (LSD) located at 6-ID sector of APS, which is designed for performing variable X-ray techniques (e.g., X-ray reflectivity, GIXD, fluorescence) on gas/liquid interface. Briefly, the highly monochromatic beam coming from one end is deflected onto the liquid surface (in the Langmuir trough) to any desired angle of incidence, α, by the beam-tilting monochromator, then the beam is further deflected by the liquid surface and collected by the detector on the other end.

In detail, the diffractometer can be divided into two main stages (left and right side of the Langmuir trough in Fig. 3.1). In the first stage, the incident beam on the liquid surface is optimized. This part consists of the axes that adjust the beam-tilting monochromator (ω, χ, ψ, ϕ), incident beam arm (S_1, S_2, α, IH), beam monitor, and variable attenuator. The ω axis, just below the monochromator crystal, is adjusted during the initial alignment process to ensure that the tilting axis χ is parallel to the monochromator surface. χ, ψ, and ϕ need to be adjusted
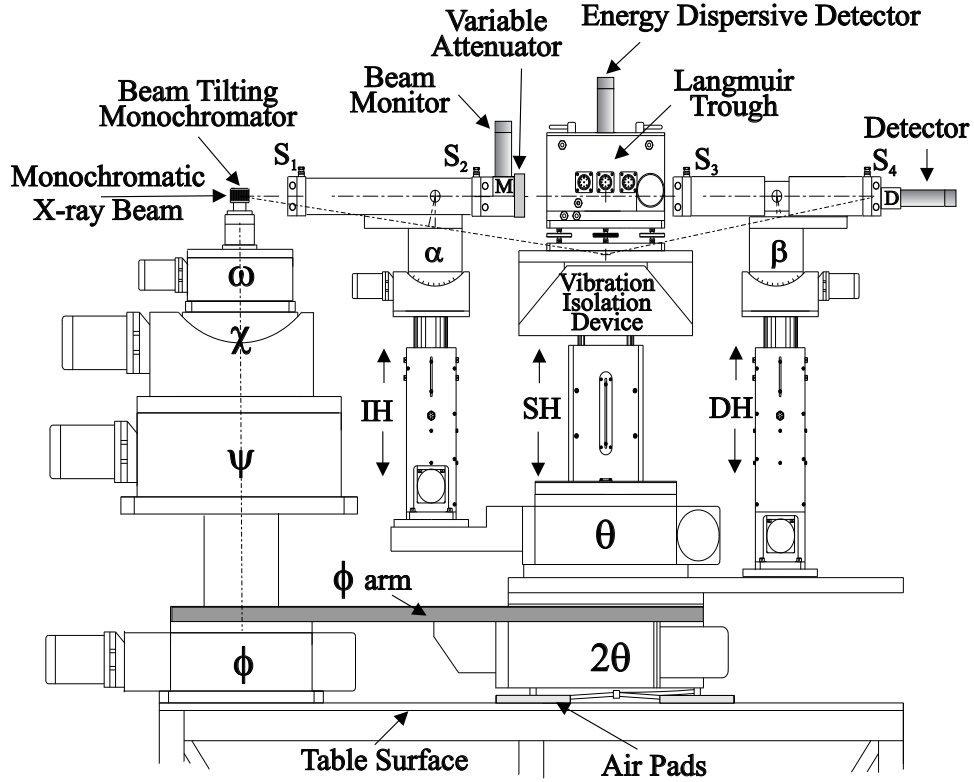
Figure 3.1   A side view diagram of the Ames Laboratory Liquid Surface
Diffractometer at the 6-ID beam line at the Advanced Photon
Source at Argonne National Laboratory.

properly in order to tilt the horizontal beam into a certain angle α (details described later). In

addition, the incident beam arm height IH, angle α, and Langmuir trough height (i.e., sample

height SH) are adjusted to ensure that the incident beam hits the center of the sample with the

desired angle α. Slits S_1 and S_2 are used to control the incident beam size and shape (normally,

a rectangular shape). To get total external reflectivity, the footprint of the incident beam needs

to be smaller than the width of the reflecting surface (i.e., trough width, ~ 12 cm). Usually,

the X-ray reflectivity measurements start from $Q_z = 0.01\text{Å}^{-1}$, and the corresponding incident

angles α are 0.0707º and 0.0349º at 8 and 16.2 keV, respectively. It gives the maximum of

incident beam height 0.148 mm at 8 keV and 0.073 at 16.2 keV. Therefore, the typical heights of

the incident beam, constrained by S_1 and S_2, are set as 0.1 mm and 0.05 mm at 8 and 16.2 keV,

respectively. There is a beam monitor located right before the Langmuir trough, monitoring

Table 3.1   Motor names for the corresponding motors shown in Fig. 3.1.

motor	name	motor	name	motor	name
ω	$mphi$	β	da	DH	dh
χ	$mtilt$	θ	th	S_1	$sl1t;sl1b$
ψ	mth	2θ	tth	S_2	$sl2t;sl2b$
ϕ	$mtth$	IH	ih	S_3	$sl3t;sl3b$
α	ia	SH	sh	S_4	$sl4t;sl4b$

any change of the incident beam intensity, which could be induced by the small instability of X-ray source and/or the instrument configuration change during the experiment.

The second stage consists of the outgoing beam arm (β, 2θ, DH), slits (S_3, S_4), and the detector. In this section, the intensity of the scattering beam from the surface is mapped out, and the angles β and 2θ and the detector height DH have to be adjusted according to the experimental details (e.g., $\beta = \alpha$ and $2\theta = 0$ for X-ray reflectivity measurements). The divergence of the outgoing beam controlled by the slits S_3 and S_4 affects the surface effective roughness as shown in the previous chapter. The two stages separated by the Langmuir trough are coupled through the ϕ-arm of the diffractometer, which needs adjustment as α varies as discussed below. There is another motor, θ, right below the Langmuir trough, which can make the trough rotate along the vertical axis. In general, it is kept idle because crystallization of monolayers at the liquid surface is powder, consisting of lots of single crystals with random orientations.

As shown in Fig. 3.1, most of the X-ray's path (from the monochromator to the detector) is between the incident beam slits (S_1 and S_2) and outgoing beam slits (S_3 and S_4), which are connected by two sealed tubes. Both tubes are in vacuum to reduce the scattering from the air to improve the X-ray intensity. All motors are connected to the motor control units (bought from Advanced Control Systems Corp.), which are further connected to the computer outside of the hutch. The motor names in the software for the corresponding motors shown in Fig. 3.1 are listed in Table. 3.1.

3.2.1 Beam-tilting Monochromator

In order to bring the beam from horizontal onto the liquid surface with a desired angle α, the monochromator is tilted by an angle χ either about the axis of the incident beam (indicated by χ_1 in Fig. 3.2) or about the axis normal to the reciprocal lattice wave vector of the monochromator, τ_0 (indicated by χ_2 in Fig. 3.2). The geometry of this tilting on both side and top views is shown in Fig. 3.2. α is the angle between reflected beam $\mathbf{K}_f$ and XY plane, ψ is the angle between incident beam $\mathbf{K}_i$ and the axis χ_2, and ϕ is the angle between χ_1 and the component of $\mathbf{K}_f$ in the XY plane. The incident and reflected beam vector in the coordinate shown in Fig. 3.2 are given by

$$\mathbf{K}_i = k_0(1,0,0); \qquad \mathbf{K}_f = k_0(\cos\alpha\cos\phi, \cos\alpha\sin\phi, \sin\alpha). \tag{3.1}$$

If the monochromator is tilted over the incident beam axis (χ_1), one can write the reciprocal lattice vector τ_0 as

$$\tau_0 = \tau_0(-\sin\psi, \cos\psi\cos\chi_1, \cos\psi\sin\chi_1), \tag{3.2}$$

where $\tau_0 = 2\pi/d$ (d is the d-spacing of the monochromator crystal). Combining Eqs. 3.1 and 3.2 and the Bragg condition for scattering,

$$\mathbf{K}_f - \mathbf{K}_i = \tau_0, \tag{3.3}$$

one can readily get the following relations,

$$\begin{aligned} \sin\psi &= \frac{\tau_0}{2k_0} \\ \sin\chi_1 &= \frac{k_0}{\tau_0}\cos\psi\sin\alpha \\ \cos\phi &= \left(1 - \frac{\tau_0^2}{2k_0^2}\right)/\cos\alpha \end{aligned} \qquad . \tag{3.4}$$

One should notice that the scattering angle ψ is independent of the tilting angle χ_1. It is due to the fact that when the monochromator crystal is rotated over the incident beam axis, ψ is always equal to the angle between the incident beam and the surface of the monochromator crystal, which is selected by the Bragg reflection and given by $\sin\psi = \frac{\lambda}{2d} = \frac{\tau_0}{2k_0}$ as shown in Eq. 3.4. Similarly, for the configuration (which is in use in our instrument) where the monochromator is
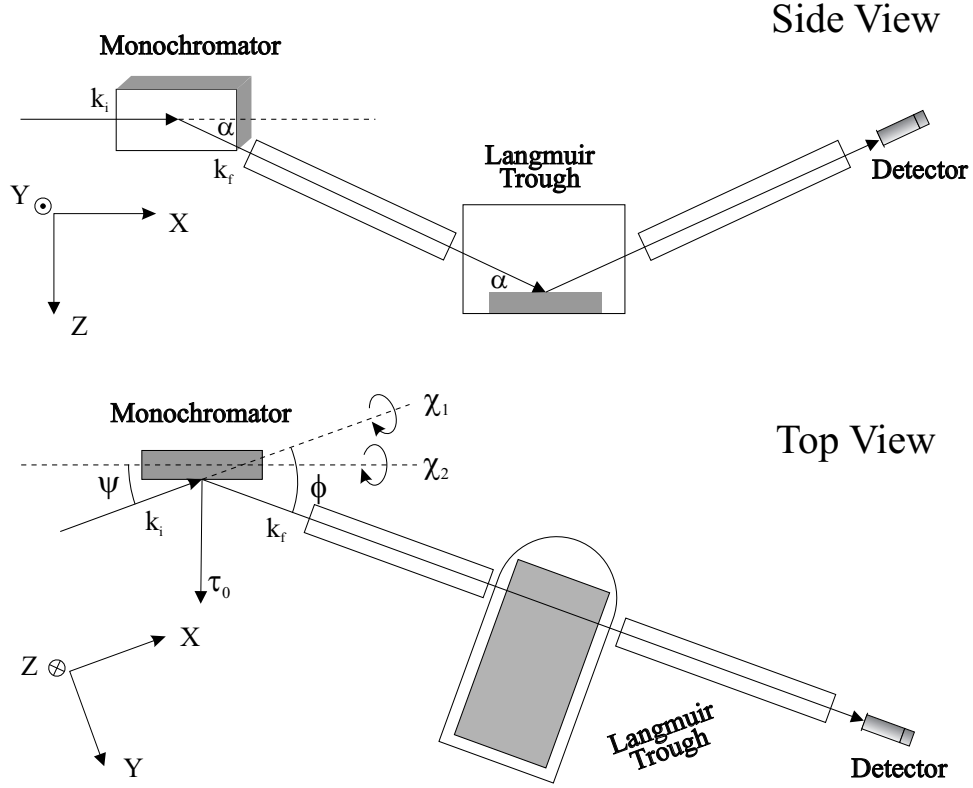
Figure 3.2   Monochromator geometry to tilt a Bragg reflected beam from
the horizon onto a liquid surface with an angle α.

tilted over the axis normal to $\tau_0 = \tau_0(-\sin\psi\cos\chi_2, \cos\psi\cos\chi_2, \sin\chi_2)$, one can obtain

$$\sin\psi = \frac{\tau_0}{2k_0\cos\chi_2}$$
$$\sin\chi_2 = \frac{k_0}{\tau_0}\sin\alpha \qquad . \qquad (3.5)$$
$$\cos\phi = \left(1 - \frac{\tau_0^2}{2k_0^2}\right)/\cos\alpha$$

Here, unlike the previous mode, tilting beam requires the adjustment of ψ, since the angle between the incident beam and the surface of the monochromator crystal gets smaller as χ_2 increases for a fixed ψ. However, for both modes, the scattering angle ϕ has to be modified as α is varied, and we have $\phi = 2\psi$ at the untilted configuration ($\alpha = 0$).

From these relations (Eq. 3.5), ψ, χ, and ϕ for any incident angle α can be calculated and applied to diffractometer, for a given wave vector (k_0) and crystal d-spacing (τ_0). In all our experiments, three single crystals have been chosen as monochromators: Ge(220), Ge(111), and α-Quartz(10$\bar{1}$1), with d-spacing 2.000, 3.266, and 4.256 Å, respectively. In order to keep
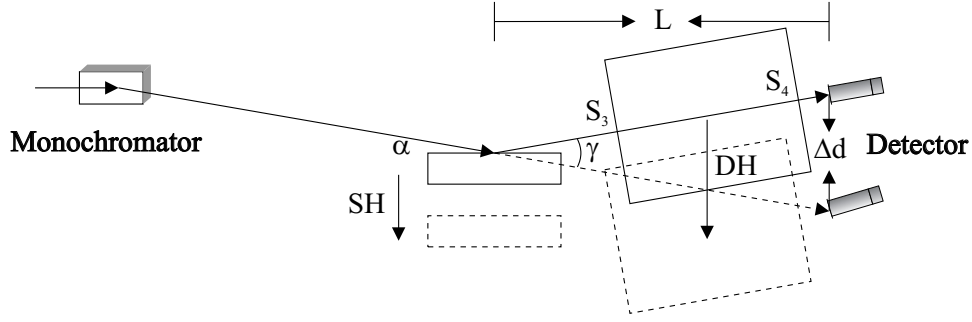
Figure 3.3   Diagram of the second stage of the alignment.

ψ and ϕ in a reasonable range, typically, Ge(220) is used for 16.2 keV, whereas Ge(111) and α-Quartz(10$\bar{1}$1) are used for 8 keV and even lower energy.

3.2.2   LSD Alignment

As introducing the diffractometer above, the alignment of the diffractometer also can be divided into two main stages. In the first stage (rough alignment, $Q_z = 0$), we use the direct beam to align the diffractometer. First, adjusting the diffractometer vertically (motors: "$leg1$", "$leg2$", and "$leg3$") and horizontally (motor: "$trans$") ensures that the incoming beam exactly hits the center of monochromator crystal. Second, scanning the angles (ω, χ, ψ, ϕ, and α) and motor "ih" optimizes the incident beam up to the beam monitor, setting the motor positions to what they should be according to Eqs. 3.5. Third, β, 2θ, and DH are adjusted to get the maximum direct beam intensity by the detector.

The second stage (fine alignment, $Q_z > 0$) is more complicated and its diagram is shown in Fig. 3.3. After the first stage, the diffractometer can be further aligned by using the reflected and direct beams as explained below. First, at $Q_z = 0$, we scan "sh" and find "$zero$" position, where the direct beam collected by the detector is half blocked. Second, we bring the diffractometer to a certain configuration ($Q_x = Q_y = 0$; $Q_z > 0$, usually $Q_z < Q_c$), and scan "sh" and "dh" to find the reflected beam. Third, we move the "sh" down and let the direct beam pass through, which can be found by the detector by moving the "dh" down accordingly. Using the "dh" difference Δd and premeasured distance L between the sample center and the detector (shown

in Fig. 3.3), for the small angles, the real and calculated Q_z is given by $\Delta dk_0/L$. Last, we move all motors back to the reflectivity condition, and set all motors to where they should be according to the calculated Q_z.

3.2.3 Detectors and Attenuator

Scintillation Detector Cyberstar X1000 fast scintillation detector (bought from Oxford Danfysik) is used for monitoring the incoming beam (monitor) and mapping out the outgoing beam (detector), which consists of a scintillator crystal, a photomultiplier tube (PMT), and a circuit for measuring the pulses produced by the photomultiplier. The scintillator (NaI(Tl), sodium iodide doped with thallium, by far the most widely used scintillator material) absorbs the incident photons and reemits the absorbed energy in the form of photons in the visible range ($\lambda \sim 420$ nm), which is called scintillation. PMT houses a bialkali photocathode (adapted to the NaI(TI) scintillation wavelength), 10 dynodes, and an anode (providing the electric field in the tube). Incident photons produced by the scintillator strike the photocathode material, producing electrons as a consequence of the photoelectric effect. These electrons are directed toward the dynodes chain, where they are multiplied by the process of secondary emission. Finally, the electrons reach the anode, where the accumulation of charge results in a sharp current pulse indicating the arrival of photons at the photocathode.

Scintillation detectors are generally assumed to be linear. This assumption is based on two requirements: (1) the output of the scintillator is proportional to the number of the incident photons; (2) the electrical pulse produced by the photomultiplier tube is proportional to the emitted scintillation photons. The linearity assumption is usually a good rough approximation, although deviations can occur, especially for a large number of incident photons, where the dead time correction is needed. However, when the incident beam exceeds a certain limit ($\sim$ 80k cps for Cyberstar X1000), an easy dead time correction is no longer valid.

Attenuator As mentioned above, our X-ray source has a count rate $\sim 10^{10}$ cps, larger than that limit. Therefore, the beam attenuator is required for the detector, which is present right after the monitor and before the Langmuir trough (see Fig. 3.1). According to Eq. 2.19, the
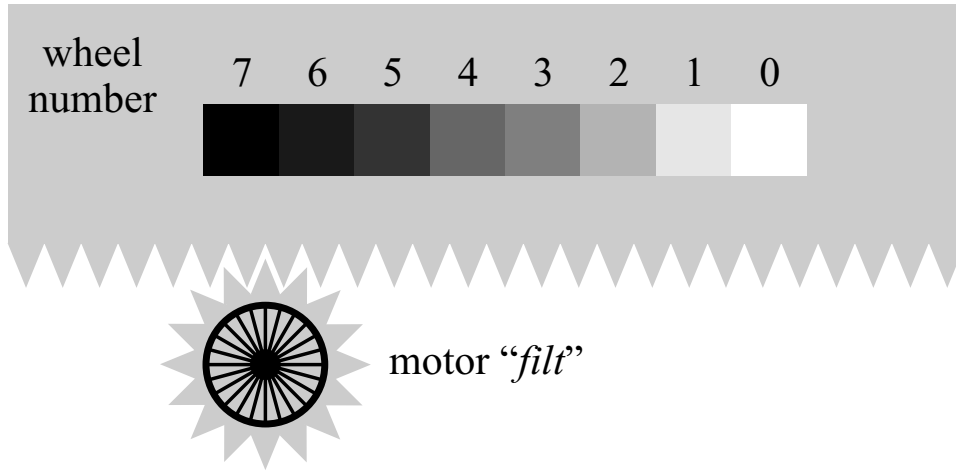
Figure 3.4   Diagram of the attenuator device.

X-ray reflectivity intensity is proportional to Q_z^{-4}, which means the incident beam needs to be more attenuated at small Q_z, and less attenuated at large Q_z. In other words, the goal is to ensure that the incident photon rate on the detector is as high as possible but less than ~ 20k cps, where the linearity assumption is still good. In order to accomplish that, a special design, consisting of various attenuators, is needed and shown in Fig. 3.4. Motor "*filt*" can change the attenuators from wheel 0 (no attenuation) to wheel 7 (maximum attenuation) as needed. The relative attenuation factor between two neighboring attenuators is given by the ratio between the counts on the detector from these two attenuators at one appropriate Q_z.

Usually, the incident beam includes a considerable amount of the 3rd order harmonic beam. To optimize the relative intensity of the 1st and 3rd harmonic beam, we typically choose the element, whose binding energy is slightly larger than the desired beam energy, as the attenuator material. For instance, we choose Nb (niobium; K shell $= 18.986$ keV) for 16.2 keV and Ni (nickel; K shell $= 8.333$ keV) for 8 keV. The beam monitor, which is present before the attenuator, collects the scattering of the incident beam from the air, whose count rate is typically less than 50k cps, implying no attenuator is required for the beam monitor. One should note that the 3rd order harmonic beam hardly has any contribution to the monitor, compared to the 1st order, due to the one or two orders of magnitude larger attenuation length.

Energy Dispersive Detector (EDD) Vortex-EX® Silicon Multi-Cathode Detector (SMCD;

SII NanoTechnology USA, Inc.) is used for collecting and analyzing the X-ray fluorescence data. The SMCD package includes the vacuum chamber, which is sealed with a Be window ($< 25\,\mu$m), and the preamplifier box. Inside the vacuum chamber are the SMCD chip, the thermoelectric cooler (TEC) and the first amplification stage field effect transistor (FET). As a type of silicon drift detector, it achieves very low capacitance (~ 0.06 pF) with a relatively large active area ($\sim 50\,\text{mm}^2$) and excellent energy resolution (< 136 eV FWHM at Mn $K\alpha$ is typical). The detector operates at near room temperature with thermoelectric cooling and is thus very compact in size. These features make it ideal for many X-ray fluorescence applications.

In principle, the SMCD is basically a pure silicon wafer (~ 0.35mm) with sideward depletion and an electrical field parallel to the surface. One side of the wafer is covered by a large area pn-junction, which is used as a homogeneous, very thin entrance window for the X-rays. The electric field is generated by concentric cylindrical drift electrodes (multi-cathode structure) on the opposite side of the wafer. The potential energy distribution for electrons in the wafer is such that the small-sized readout anode in the center of the device is the point of minimum potential energy, collecting all signal electrons generated in the depleted volume.

The SMCD measures the relative abundance of emitted X-rays versus their energy. When an incident X-ray strikes the detector, it creates plenty of electron/hole pairs, and electrons are forced to reach the anode to generate a charge pulse that is proportional to the energy of the X-ray. The charge pulse is converted to a voltage pulse, which remains proportional to the X-ray energy, by a charge-sensitive preamplifier. The signal is then sent to a multichannel analyzer (MCA), where the pulses are sorted by voltage. The energy, as determined from the voltage measurement, for each incident X-ray is sent to a computer for display and further data evaluation.

3.2.4 Langmuir Trough

Figure 3.5 shows the diagrams of a specially designed Langmuir trough, which mainly consists of an aluminum chamber and a telfon trough. In addition to providing a platform for the sample, the Langmuir trough can also record the surface pressure, temperature, and molecular area

Top View

water in   helium in   semiconductor thermistor

connected
to a chiller

← barrier

x-rays

Wihelmy
microbalance

aluminum
chamber

water out   helium out   teflon trough SiO_2 glass

Side View

helium pipes

in
out

motor
"*trough*"   EDD   microbalance

connected
to a chiller

telfon barrier

Kapton
window

water pipes   trough SiO_2 glass   thermistor   filter-paper
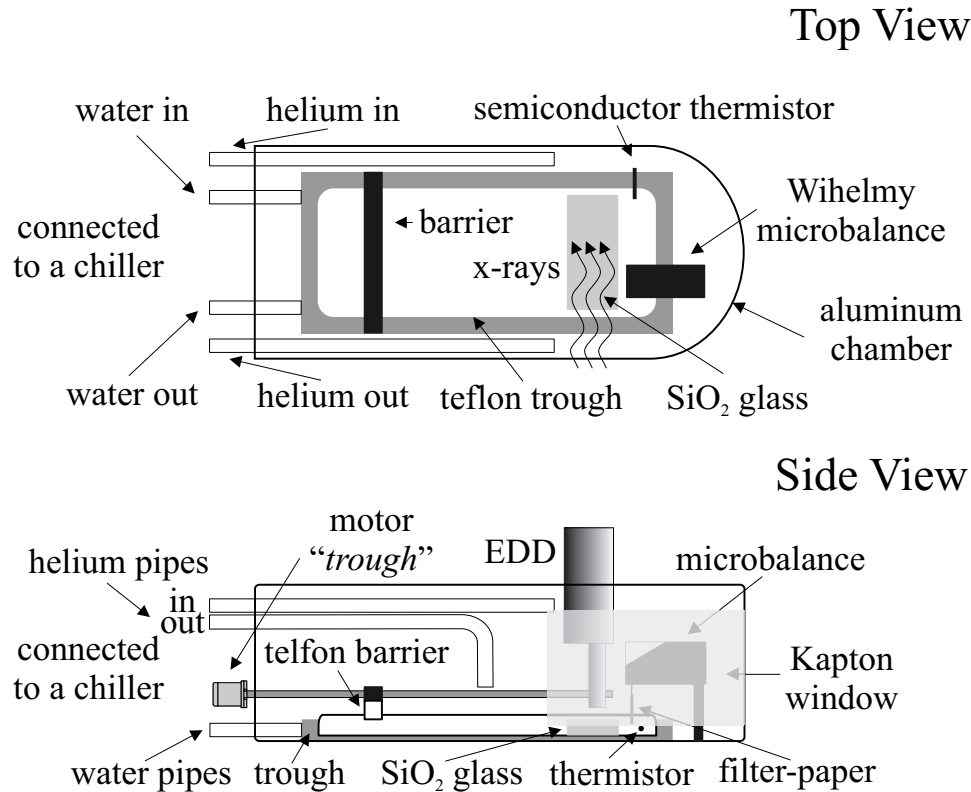
Figure 3.5   Top and side view diagrams of Langmuir trough

during experiments. A vibration isolation device underneath of the Langmuir trough (shown in Fig. 3.1) is used to suppress the liquid surface vibration induced by the sample height (SH) movements. A SiO_2 glass, placed below the liquid surface and at illuminated area as shown in the top view, is used for reducing the height of the water film to ~ 0.3 mm and further damping surface waves [74]. In X-ray (incident and outgoing beam) path area, the aluminum shell is replaced by Kapton film (shown in side view), which is commonly used as a material for windows of all kinds of X-ray sources. Its high mechanical and thermal stability as well as its high transmittance to X-rays make it the preferred material.

Physical properties of the monolayer materials vary with temperature; it is very important to maintain the sample temperature at a certain level. To accomplish that, water goes through the base of the trough by pipes connected to a chiller, providing a wide temperature control range ($10 - 70^{\circ}$C). Water-saturated helium with the same temperature also goes through the chamber, which has threefold functions. First, the helium environment can minimize radiation

damage due to the formation of radicals and ions and it can reduce the background scattering from air, which is very critical to the GIXD measurements. Air scattering in the trough can give rise to background levels that are at least two or three orders of magnitude higher than the expected signal from a typical 2-D Bragg reflection in the GIXD. Second, purging the helium with the same temperature as the trough helps the sample to reach temperature equilibrium quickly. Lastly, water-saturated helium prevents the change of the liquid surface level due to the evaporation of the water.

The telfon barrier position is controlled by the motor "trough", determining the trough area, A_{trough}, between the barrier and the other end of the trough (right end in the top view). For our trough design, A_{trough} can be continuously changed from 278 to 92.4 cm^2. To convert the trough area to the monolayer molecular area, a conversion factor C is needed and given by

$$C = \frac{A_{trough}(\text{cm}^2)}{A_{molecule}(\text{Å}^2)} = \frac{60.2\rho_m(\text{g/l})V(\mu\text{l})}{M.W.}, \tag{3.6}$$

where ρ_m is the mass density of monolayer material in the solution (process to make a solution is discussed later), V is the volume of monolayer material solution spread on the surface, and $M.W.$ is the molecular weight of monolayer material.

The sample temperature is recorded by a semiconductor thermistor whose resistance varies with temperature. The temperature dependence of the resistance is given by Steinhart-Hart equation as

$$\frac{1}{T} = A + B\ln(R) + C(\ln(R))^3, \tag{3.7}$$

where T is the temperature (in Kelvin) and R is the resistance at T (in Ohms). A, B, and C are the Steinhart-Hart coefficients, which vary depending on the type and model of thermistor and temperature range of interest.

Wihelmy microbalance combined with the filter paper shown in the side view are used for measuring the surface pressure. The microbalance needs to be calibrated by a few known masses before use. The surface pressure, π, is given by

$$\pi = \frac{F_0(\text{mN}) - F(\text{mN})}{L(\text{m})}, \tag{3.8}$$
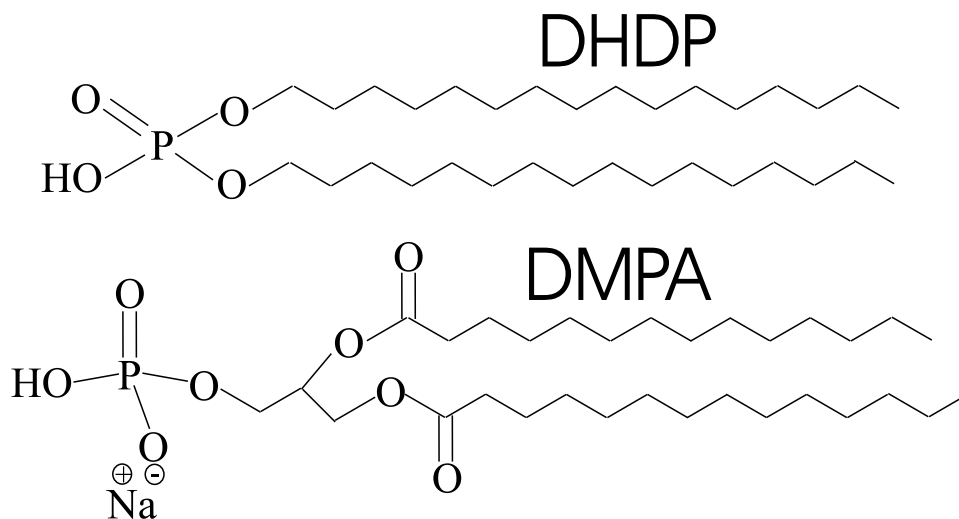
Figure 3.6 Dihexadeocyl hydrogen phosphate (DHDP) and 1,2-dimyris-toyl-*sn*-glycero-3-phosphate (sodium salt, DMPA) molecules used to form the Langmuir monolayers.

where F and F_0 are the forces on the microbalance when the filter paper is immersed in the sample and pure water, respectively, and L is the perimeter of the filter paper. The monolayer can also be held at a constant surface pressure, enabled by a computer controlled feedback system between the motor "*trough*", responsible for the movements of the compressing barrier, and the microbalance.

3.3   Sample Preparations

Dihexadecyl hydrogen phosphate (DHDP, $C_{32}H_{67}O_4P$; *M.W.* = 546.85, CAS# 2197-63-9, Sigma Corp.) and 1,2-dimyristoyl-*sn*-glycero-3-phosphate (sodium salt, DMPA, $C_{31}H_{60}O_8PNa$; *M.W.* = 614.77, CAS# 80724-31-8, Avanti Polar Lipids.), shown in Fig. 3.6, are chosen as monolayer materials in the current study. DHDP and DMPA are dissolved into 3:1 chloro-form/methanol without further purification and stored into the precleaned vials with a typical volume of 10 or 20 ml. Vials must be sealed by parafilm and stored in the refrigerator when not in use. Hamilton syringes (model 1710TLL, Sigma Corp.) with a typical capacity of 50 μl are used to take the monolayer materials solutions from vials and spread them on the liquid surface. During the spreading, monolayer materials solutions could drop into the bulk since chloroform

has higher density than water. To avoid it, we make a tiny droplet at the tip of syringes each time, and let it gently touch the surface and spread.

Monolayer compression, at a rate of $\sim 1\,\text{Å}^2/(\text{molecule} \times \text{min})$, is started 10-15 minutes after spreading to allow solvent evaporation. During the compression, the surface pressure is recorded by a microbalance using a filter paper, and the molecular area is recorded by the barrier position. It yields the isotherm (surface pressure versus molecular area, $\pi - A$) for monolayer materials on the air/liquid interface. The molecular area range of interest in the isotherm is $20 - 60\,\text{Å}^2$ for molecules with two acyl-chains since the cross-section of one acyl-chain is $\sim 20\,\text{Å}^2$. That indicates the conversion factor C to be about $4 \sim 5$. According to Eq. 3.6 and the typical spreading amount ($30 \sim 40\,\mu\text{l}$), the solute concentration is usually about $1 \sim 2\,\text{g/l}$ for DHDP and DMPA.

3.4   Radiation Damage

Origins of Damage Radiation damage to the specimen is a common nuisance when dealing with liquid surfaces. Many of the studies of liquid surfaces and monolayers involve investigations of organic or biomaterials that are susceptible to chemical transformations in general and, in particular, in the presence of the intense synchrotron beam. Radiation damage is of course not unique to monolayers on a liquid surface; other X-ray techniques that involve organic materials (protein, polymer, liquid crystals, and others) face similar problems. Radiation damage to a specimen proceeds in two steps. First, the specimen or a molecule in its surroundings is ionized (by the photoelectric, Auger, or Compton effect) or excited to higher energy levels (creating radicals). Subsequently, the ionized/excited product can react with a nearby site of the same molecule or with a neighboring molecule to form a new species, altering the chemistry as well as the structure at the surface. The remedies that are proposed here are in part specific to liquid surfaces and cannot be always fulfilled in view of the specific requirements of an experiment. To minimized the radiation damage, we use all of the following remedies.

Sample Exposure Control The most effective way to reduce the radiation damage is to reduce the sample exposure by minimizing time and intensity. The beam is blocked by a shutter

when not collecting data (e.g., while motors are still moving to their final positions.), which means that the sample is only exposed in the counting time. Reduced exposure can be also achieved by attenuating the flux on the sample to roughly match it to the expected signal, so that the full intense beam is used only for signals with cross-sections for scattering that require it.

High X-ray Energy Another approach to reducing the effect of the primary stage is by performing experiments at high X-ray energy. It is well known that the cross-section for all the primary effects is significantly reduced with the increase of X-ray energy. If the experiment does not require a specific energy, such as in resonance studies, it is advantageous to operate at high X-ray energy. However, higher mechanical angular resolutions and smaller slits are required in order to achieve reciprocal space resolutions comparable to those at lower energies.

Helium Environment Air surrounding the sample has probably the most negative effect on the integrity of the organic film at the liquid interface. The X-ray radiation readily creates potent radicals in the air (e.g., monatomic oxygen), which are highly diffusive and penetrant and can interact with almost any site of an organic molecule. Working in a helium environment can significantly reduce this source of radiation damage.

Lateral Translation Device The liquid substrate, even water, can create temporary radicals that can damage the monolayer, in particular, the head group region of lipids. Water under intense X-ray radiation can give many reactive products such as H_2O_2 or monatomic oxygen that can readily interact with the monolayer. Thus, some radiation damage, with extent that may vary from sample to sample, is inevitable, and fresh sample is required to complete the study. Moving the sample underneath the footprint is a quick fix in that regard, assuming that the radiation damage is mostly localized around the illuminated area. To accomplish that, in our instrument design, the Langmuir trough is mounted on a motorized stage that can translate the surface laterally with respect to the incident beam to allow X-ray probe different parts of the surface. With this design, one can also reproduce results and monitor radiation damage of the monolayer by examining the different regions of the sample.

3.5   Data Analysis

The majority of data analysis for the current study is extracting the ED profile from the X-ray reflectivity data. Modifications of the raw data before the analysis include data normalization and background subtraction. Due to the small variety of the incident beam intensity, the counts on the detector must be normalized by the counts on the monitor. The normalized intensity is

$$I = (I_s \pm \Delta I_s); \ I_s = \frac{\text{C[det]}}{\text{C[mon]}}; \ \Delta I_s = \sqrt{\frac{\text{C[det]}}{\text{C}^2\text{[mon]}} + \frac{\text{C}^2\text{[det]}}{\text{C}^3\text{[mon]}}}, \tag{3.9}$$

where ΔI_s is the uncertainty for normalized signal I_s, and C[det] and C[mon] are the counts on the detector and monitor, respectively. The contribution of the background to the signal becomes more and more significant as Q_z goes up, mainly due to the bulk scattering. There-fore, the background measurement and subtraction are necessary for getting the real signal (i.e., reflectivity), especially for large Q_zs. Intensity measurement by moving 2θ to 0.5^o from any specular reflectivity condition gives the background intensity I_b and its uncertainty ΔI_b, sim-ilar to Eq. 3.9. Considering the different attenuations used for different Q_zs and background subtraction, the real reflectivity R and its uncertainty σ are given by

$$\begin{aligned} R &= A(I_s - I_b) \\ \sigma &= A\sqrt{(\Delta I_s)^2 + (\Delta I_b)^2} \end{aligned} \ , \tag{3.10}$$

where A is the attenuation factor. R below the critical angle is further normalized to unity before the analysis.

The most common procedure for the analysis is the use of standard nonlinear least squares refinement of an initial ED model. The initial model is defined in terms of a P-dimensional set of independent parameters, $\mathbf{p}$, using all the information available in estimating $\rho(z, \mathbf{p})$. The parameters are then refined by minimizing the $\chi^2(\mathbf{p})$ quantity

$$\chi^2(\mathbf{p}) = \frac{1}{n - P} \sum_i \left[\frac{R_{exp}(Q_{z,i}) - R_{cal}(Q_{z,i}, \mathbf{p})}{\sigma(Q_{z,i})} \right], \tag{3.11}$$

where $\sigma(Q_{z,i})$ is the uncertainty of the measured reflectivity, $R_{exp}(Q_{z,i})$ (see Eq. 3.10), n is the number of measured points, and P is the number of parameters used to calculate the reflectivity, $R_{cal}(Q_{z,i}, \mathbf{p})$, according to Eq. 2.45. Uncertainties of a certain parameter can be obtained by

fixing it at different values away from its optimum and readjusting all other parameters to a new minimum until χ^2 increases by 50% [75, 76].

There can be multiple ED profiles that essentially yield the same reflectivity calculations. The uniqueness can be achieved by introducing physical constrains that are incorporated into the parameters of the model. Volume, in-plane density of electrons, etc., are among such constraints that can be used. Applying such constraints [76, 77, 78] can reduce the uncertainties and make ED profiles associated to the actual molecular arrangement. During the fitting process (minimizing the χ^2), χ^2 could be easily trapped into a serial local minima, making the initial estimating values important to reach the global minimum.

CHAPTER 4. MONOVALENT COUNTERION DISTRIBUTION AT HIGHLY CHARGED WATER INTERFACE PROBED BY ANOMALOUS REFLECTIVITY

To study the accuracy of Poisson-Boltzmann (PB) theory for monovalent ions, we performed surface sensitive synchrotron X-ray scattering studies on monolayer materials spread on 1:1 electrolyte solutions. DHDP was spread as a monolayer at the air/liquid interface to control surface charge density. Five decades in bulk ionic concentrations (CsI) are investigated, demonstrating that the interfacial distribution is strongly dependent on bulk concentration according to the reflectivity data off resonance (16.2 keV). We show that this is due to the strong binding constant of hydronium, H_3O^+, to the phosphate group, leading to proton transfer back to the phosphate group and to a reduced surface charge. The increase of Cs^+ concentration modifies the contact value potential, thereby causing proton release. This process effectively modifies the surface charge density and enables exploration of ion distributions as a function of effective surface charge density.

Using anomalous reflectivity off and at the Cs^+ L_3 resonance (5.012 keV), we provide spatial counterion (Cs^+) distributions next to the negatively charged interfaces. The experimental ionic distributions are in excellent agreement with a renormalized surface charge PB theory without fitting parameters or additional assumptions. We also discuss the accuracy of our experimental results in discriminating among possible deviations from PB theory.

4.1 Isotherm Comparisons

Surface pressure versus molecular-area ($\pi - A$) isotherms of DHDP at various CsI salt concentrations (n_b) are shown in Fig. 4.1. For $\pi > 0$, the isotherm exhibits two distinct slopes,
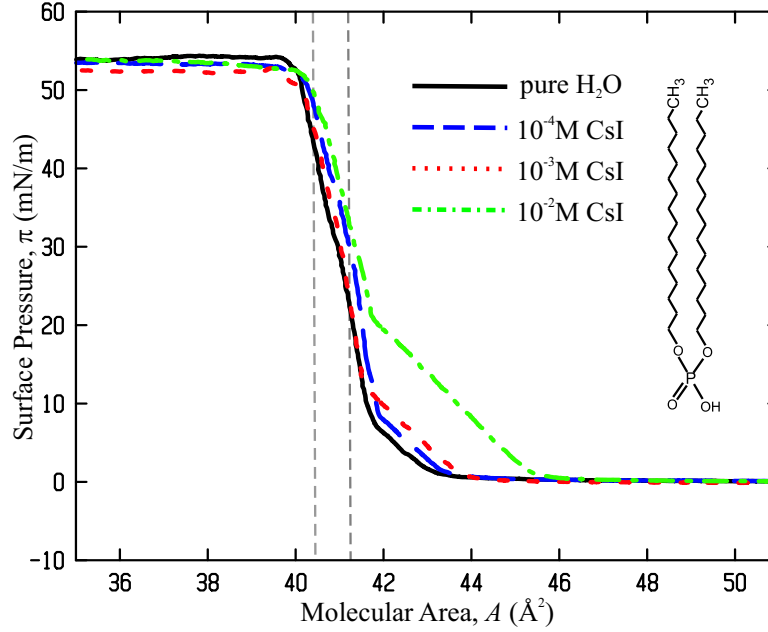
Figure 4.1   Surface pressure versus molecular area for DHDP spread on CsI solutions at various concentrations as indicated. Reflectivity and GIXD were performed at constant surface pressures 30 mN/m and 40 mN/m. The dash lines indicate the region where all X-ray experiments were conducted.

associated with crystalline tilted and untilted acyl-chains with respect to the surface normal. The transition from tilted to untilted chains at (A_t, π_t), occurs at a constant $A_t \approx 41.5$ Å^2, whereas π_t increases with salt concentration n_b. CsI and other electrolytes (NaCl and CsCl) in solution significantly influence the isotherm, causing an increase of the monolayer-coalescence area A_C, (i.e., $\pi > 0$) with the increase in n_b. For $A \leq 39$ Å^2 , approximately the cross-section of the two acyl-chains of DHDP, (constant $\pi \approx 55$ mN/m) the monolayer is in the yet poorly characterized state of collapse.

The headgroup $(R - PO_4H)$ of DHDP can be negatively charged after proton release (PO_4^-), providing the charged surface, whose charge density is presumably determined by the molecular area and given as $\sigma_s = -e/A$. According to the PB theory as discussed in Chapter I, counterion distribution near the interface has no n_b dependence for a highly charged surface. To verify that, it is better to fix surface charge density σ_s and vary bulk ionic concentration n_b. Therefore, in the present study, we focus on the untilted crystalline phase $(30 \leq \pi \leq 45$ mN/m), where
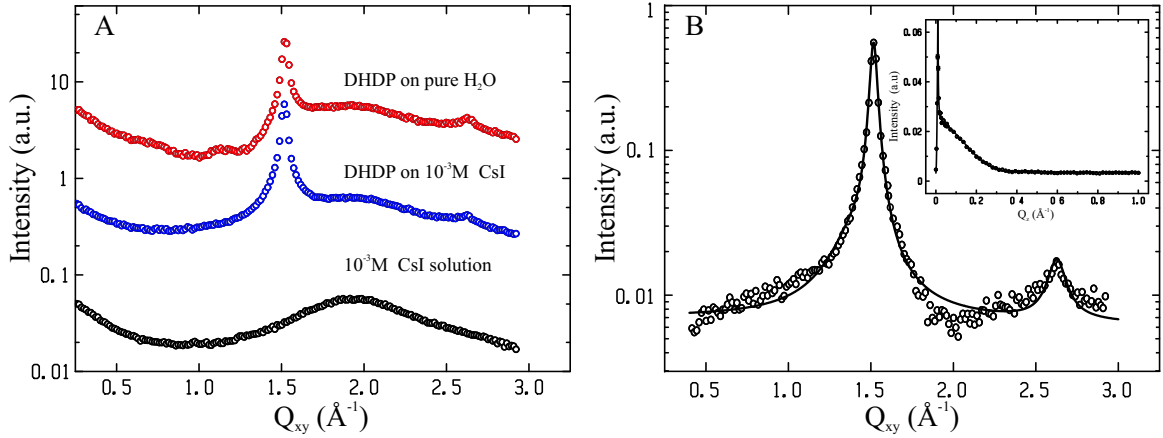
Figure 4.2   (A) GIXD scans versus the modulus of the in-plane momentum transfer Q_{xy}, at surface pressure $\pi = 30$ mN/m (curves are shifted by decades for clarity). The Bragg peaks are independent of bulk salt concentration indicating no significant change in in-plane molecular packing. GIXD scan for 10^{-3} M CsI (bare surface) shows a broad peak at $Q_{xy} \approx 2.0\text{Å}^{-1}$, due to the surface structure of water. (B) Background subtracted GIXD pattern for a DHDP monolayer on 10^{-3} M CsI solution ($\pi = 30$ mN/m) and the corresponding rod scan (shown in the inset) at the (1,0) peak ($Q_{xy} = 1.516\,\text{Å}^{-1}$).

the molecular area variation at a fixed π is less than 1.5%. In other words, the surface charge density (molecular area) is independent of the bulk concentration in that phase, and its value is $\sim -e/41\text{Å}$ as shown in Fig. 4.1 by assuming that each DHDP headgroup (PO_4^-) provides one negative charge.

4.2   GIXD and Rod Scan

GIXD experiments provided additional insight into the molecular packing of the acyl chains within the Langmuir monolayers, namely, the average in-plane density of the headgroups and the surface charge density. Figure 4.2(A) shows GIXD scans (X-ray energy is 16.2 keV; $\alpha = 0.064°$ and $\beta = 0.27°$) from DHDP on pure water and on CsI solution (10^{-3} M, at $\pi = 30$ mN/m) and from bare surface of CsI solution (10^{-3} M) before spreading the monolayer as a function of in-plane momentum transfer $Q_{xy} = \sqrt{Q_x^2 + Q_y^2}$. The broad peak centered at

Table 4.1 Best-Fit Parameters to high-resolution diffraction scan of DHDP
on 10^{-3} M CsI solution ($\pi = 30$ mN/m) shown in Fig.

peak	Q_{xy} (Å^{-1})	Δ (Å^{-1})	Intensity (a.u)
(1,0)	1.516±0.003	0.026	0.522
(1,1)	2.627±0.024	0.060	0.009

$Q_{xy} \approx 2$ Å^{-1} is due to the structure factor of the aqueous solution interface. The spreading and compression of the monolayer slightly modifies the water structure factor peak at $Q_{xy} \approx 2$ Å^{-1} and brings about two prominent Bragg reflections due the ordering of acyl-chains superimposed on a modified surface liquid structure factor [79]. The main features of the diffraction pattern are independent of the ionic concentration, consistent with the isotherms at the 30-40 mN/m region that show very small variations in the molecular packing. Figure 4.2(B) shows the 2D background subtracted (GIXD data of 10^{-3} M CsI solution with bare surface shown in (A)) diffraction pattern for a DHDP monolayer on 10^{-3} M CsI solution, consisting of a strong Bragg reflection at $Q_{xy} = 1.516$ Å^{-1} and a weaker peak at $Q_{xy} = 2.627$ Å^{-1}, corresponding to 4.145, and 2.392 Å d-spacings, respectively (Table 4.1). The shape, spacing, and location of the two intense peaks correspond closely with literature values for $(1,0)$ and $(1,\bar{1})$ planes in a hexagonal unit cell of ordered alkyl chains, also confirmed by the ratio $Q_{xy}(1,\bar{1})/Q_{xy}(1,0) = \sqrt{3}$. This unit cell (molecular area 19.83 Å^2) agrees with the cross-sectional area of alkyl chain [80]. Each headgroup has two alkyl chains, giving a molecular area of 39.66 Å^2, in agreement with values obtained from the $\pi - A$ isotherm (~ 40.5 Å^2, $\pi = 40$ mN/m). The small variations in molecular areas are attributed to the existence of domain boundaries, defects and minute impurities. The peaks in Fig. 4.2(B) were fitted to Lorentzians (solid line), whose parameters are given in Table. 4.1. The peak line width Δ is significantly larger for the higher order peak. This is expected in simple 2D crystals [81] and is even more pronounced for 2D crystals fluctuating in 3D space (fluctuating tethered membranes, see Ref. [82]). Here, it is worthy to emphasize again that for the untilted crystalline phase, the surface charge density (molecular area; $\sim -e/41$Å) is practically bulk concentration independent according to the combination of isotherm and GIXD measurements of DHDP monolayers on CsI solution in the $10^{-1} - 10^{-5}$ M range.

The inset in Fig. 4.2(B) shows the rod-scan at $Q_{xy} = 1.516$ Å^{-1} ((1,0) Bragg reflection), which basically is a β scan at a fixed 2θ (see Fig. 2.10 for experimental setup) and is used to determine the average ordered chain length and tilt with respect to the surface normal. The intensity along the rod of the 2D Bragg reflection is analyzed in the framework of the distorted wave Born approximation (DWBA)

$$I(Q_{xy}, Q_z) \approx |t(k_{z,i})|^2 |F(Q_z)|^2 |t(k_{z,f})|^2, \tag{4.1}$$

where $t(k_{z,i})$ and $t(k_{z,f})$ ($k_{z,i} = k_0 \sin\alpha$; $k_{z,f} = k_0 \sin\beta$) are the Fresnel transmission functions, which give rise to an enhancement at the critical angle. In modeling the rod scans, the length and tilt of the tails are varied, examining two tilt directions: one toward nearest neighbors (NN) and the second toward next NN (NNN) [44, 80]. The form factor for the tails is given by

$$F(Q_z') = \sin(Q_z' l/2)/(Q_z' l/2) \tag{4.2}$$

where Q_z' is defined along the long axis of the tail, and l is the length of the tail. The rod scan analysis (using Eqs. 4.1 and 4.2) yields an average chain-length ~ 20 Å, and a tilted angle with respect to the surface normal $< 5°$, consistent with the reflectivity and previous reports [83].

4.3   Reflectivity Off Resonance

Figure 4.3(A) shows the normalized reflectivity curves, R/R_F (where R_F is the calculated reflectivity of an ideally flat subphase interface; Fresnel reflectivity for pure water), for DHDP ($\pi = 40$ mN/m) on pure H$_2$O and CsI solutions measured at $E = 16.2$ keV. The solid lines are the best-fit calculated reflectivities based on the ED profiles shown in Fig. 4.3(B). Similar reflectivity curves were obtained for $\pi = 30$ mN/m. In Fig. 4.3(A), all X-ray reflectivity curves differ in the exact position and the sharpness of their minima, and the intensities of their maxima. Similar reflectivity curves were obtained for $\pi = 30$ mN/m (data not shown). In details, as the bulk concentration increases, the intensities of maxima are getting higher and the minima are getting sharper and shifting to the smaller Q_z. Given that, as already shown, the packing of DHDP is basically independent of salt concentration for $\pi = 40$ mN/m, the reflectivity curves
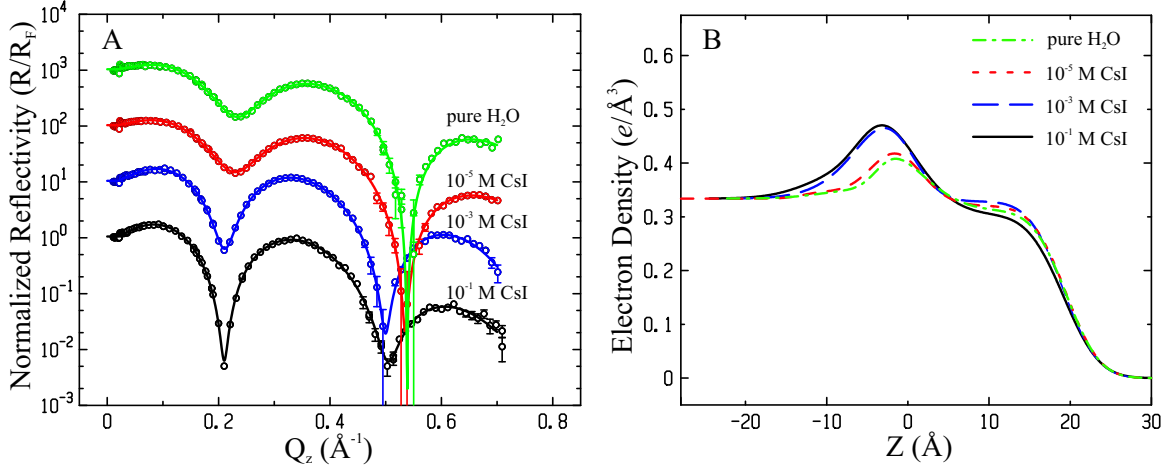
Figure 4.3   (A) X-ray reflectivity (circles) and corresponding best fit (solid lines) for the DHDP monolayer at four solutions ($\pi = 40$ mN/m) (curves are shifted by a decade for clarity). (B) ED profiles used to calculate the fits shown in (A).

in Fig. 4.3(A) qualitatively show a strong dependence of ion distribution close to the interface on bulk ion concentration, which is in a disagreement with PB theory.

Herein, the electron density profile across the interface is extracted by a two-stage refinement of a parameterized model that best fits the measured reflectivity by nonlinear least squares method. A generalized density profile $\rho(z) = \rho'(z) - i\rho''(z)$ of the electron density (ED) and the absorption density (AD) (real and imaginary parts, respectively) is constructed by a sum of error functions as follows:

$$\rho(z) = \frac{1}{2} \sum_{i=0}^{N} \mathrm{erf}\left(\frac{z - z_i}{\sqrt{2}\sigma_i}\right)(\rho_i - \rho_{i+1}) + \rho_{N+1}/2, \qquad (4.3)$$

where N+1 is the number of interfaces, $\rho_i = \rho'_i - i\rho''_i$, z_i and σ_i are the position and roughness of the ith interface, respectively, ρ_{N+1} is the electron density of the solution ($\approx 0.334\, e/\text{Å}^3$), and $\rho_0 = 0$ is the electron density of the gaseous environment. The use of a different roughness σ_i for each interface preserves the integral of the profile along Z direction or the electron density per unit area, thus conserving the chemical content per unit area. Although small variations are expected in σ_i for interfaces that separate rigid portion of a molecule (hydrocarbon chains/gas interface and hydrocarbon chain/headgroup interface, for instance), somewhat larger variations can occur at different interfaces (such as, gas/hydrocarbon chains interface
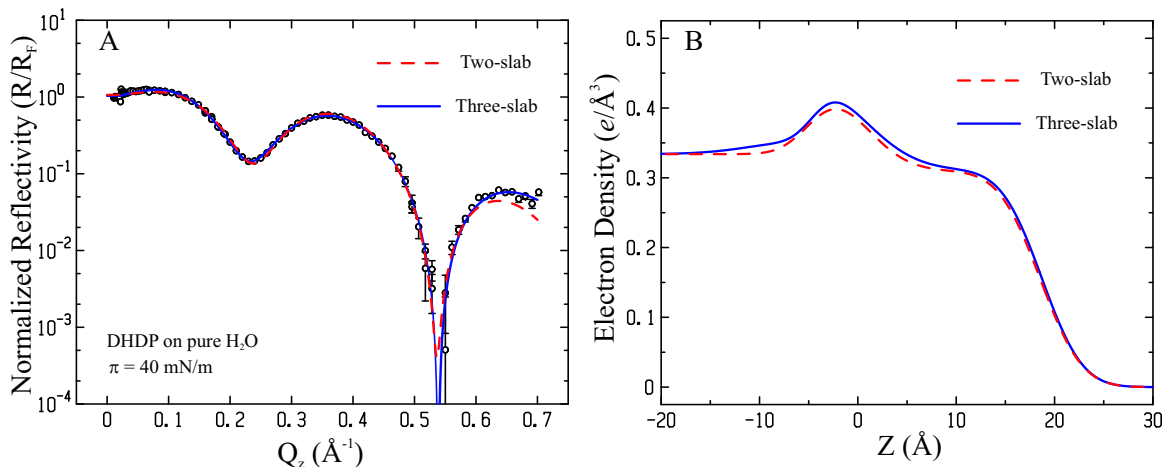
Figure 4.4   (A) Reflectivity (circles) taken from DHDP on pure H_2O and the best fit by using two-slab model (dashed line) and three-slab model (solid line). (B) ED profiles extracted from two-slab and three-slab model.

versus headgroup/subphase interface). The AD profile is particularly important at the Cs resonance (5.012 keV) as demonstrated below. The reflectivity is calculated by recursive dynamical methods [72, 84] of the discretized ED and AD in Eq. 4.3. In the first stage of the refinement, the variable parameters used to construct the electron density across the interface $\rho(z)$ are the thickness values of the various slabs $d_i = |z_{i+1} - z_i|$, their corresponding electron densities ρ_i, and interfacial roughness σ_i. By nonlinear least square fit we determine the minimum number of slabs required for obtaining the best fit to the measured reflectivity. The minimum number of slabs is the one for which the addition of another slab does not improve the quality of the fit, i.e., does not improve χ^2. In the second stage, we apply space filling and volume constraints [75, 76, 78] to calculate ρ_i by assigning to each slab a different portion of the molecule, the ions and water molecules, to a profile that has the same number of slabs as obtained in stage one of the analysis.

In the first stage of the analysis, we find that the three-slab ($N = 3$) model provides good quality fit to all reflectivities, and it does not improve with the addition of more slabs, i.e., more parameters. Our measured reflectivity for DHDP on pure H_2O is consistent with previous measurements [78] but extends to larger momentum transfers (Q_z), allowing for a more refined

Table 4.2   Best-Fit Parameters to the measured reflectivities of DHDP monolayers at $\pi = 40$ mN/m that generate the ED profiles across the interface. In this work, the error estimate (in parentheses) of a parameter is obtained by fixing a parameter at different values away from its optimum and readjusting all other parameters to a new minimum until χ^2 increases by 50%. Thicknesses of head group and Cs slab are not well defined due to electron density decay from $z = 0$ to the bulk.

subphase	H_2O	10^{-5} M CsI	10^{-3} MCsI	10^{-1} MCsI
d_{tail} (Å)	18.7(5)	19.6(10)	19.2(8)	20.2(6)
ρ_{tail} $(e/\text{Å}^3)$	0.311(8)	0.320(17)	0.329(14)	0.304(8)
d_{head} (Å)	4.4	3.2	3.8	4.3
ρ_{head} $(e/\text{Å}^3)$	0.476(15)	0.547(27)	0.590(39)	0.624(38)
d_{Cs} (Å)	3.6	9.5	3.3	4.2
ρ_{Cs} $(e/\text{Å}^3)$	0.375(11)	0.347(5)	0.431(14)	0.441(8)

structural analysis. Indeed, the two-slab model used in Ref. [78] was found to be slightly inadequate, particularly at large Q_z, and a better fit is achieved by adding an extra slab at the water-headgroup region as shown in Fig. 4.4. Thus, our detailed analysis of DHDP on pure water differs from the one reported in Ref. [78] in which the headgroup resides on a thin layer $(4 - 6 \text{ Åthick})$ of ED that is just slightly larger than that of bulk water (see Table 4.2). Similar observations were also reported for other monolayers at gas/water interface, and were interpreted as interfacial water restructuring induced by hydrogen bonds [85]. Further evidence of water restructuring at the interface is also found in the overall GIXD of the interfacial structure factor of water, especially a decrease in peak intensity at $Q_{XY} \approx 2 \text{ Å}^{-1}$ is observed [79].

Modeling DHDP monolayers on the salt solution is slightly more complicated as Cs^+ concentration decays slowly as a function of distance from the interface. As sketched in Fig. 4.5, we assume that Cs ions are present in both the head-group slab and the slab contiguous to it toward the bulk of the solution. Table 4.2 shows the parameters used to produce the ED profiles in Fig. 4.3(B) and the best-fit shown in Fig. 4.3(A). The position at $z = 0$ is defined by the interface between the phosphate headgroup and the hydrocarbon chain. ED profiles show that electron densities at and below the phosphate headgroup region are higher with the increase of salt bulk concentration, indicating more Cs^+ accumulating on the surface, and resulting in
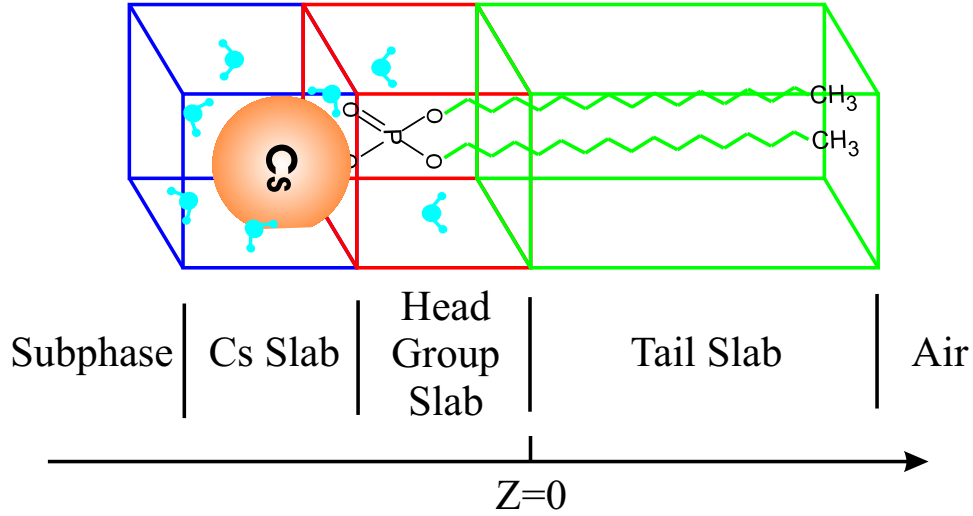
Figure 4.5   Schematic illustration of the three-slab model used to calculate self consistently the electron density profile assuming the a DHDP monolayer of known average molecular area, from GIXD and $\pi - A$ isotherm, and the associated Cs^+ and water molecules in the different slabs. Volume constraints were also applied in the ED calculations of the different potions of the molecule and the ion distribution.

sharper minima at smaller Q_z in the reflectivity data as shown in Fig. 4.3(A). The small differences of EDs associated with the alkyl-chains for the different subphases are due to the minute variations in molecular areas as shown in the isotherms above.

4.4   Modifications of PB Theory

As shown before, there is a significant difference between PB theory and our experimental observations. In order to understand it, a couple of modifications from the origin PB theory, induced by our studying system, must be introduced first. In the origin PB theory in planar geometry, the surface is assumed to be ideally flat, which is not true for a real air/liquid interface due to the capillary waves. To account for that fact, we propose to convolve the theoretical distribution $n_+(z)$ with a Gaussian function as follow:

$$n_+^r(z) = \frac{1}{\Gamma\sqrt{2\pi}} \int n_+(z')e^{-\frac{(z-z')^2}{2\Gamma^2}} dz'. \tag{4.4}$$
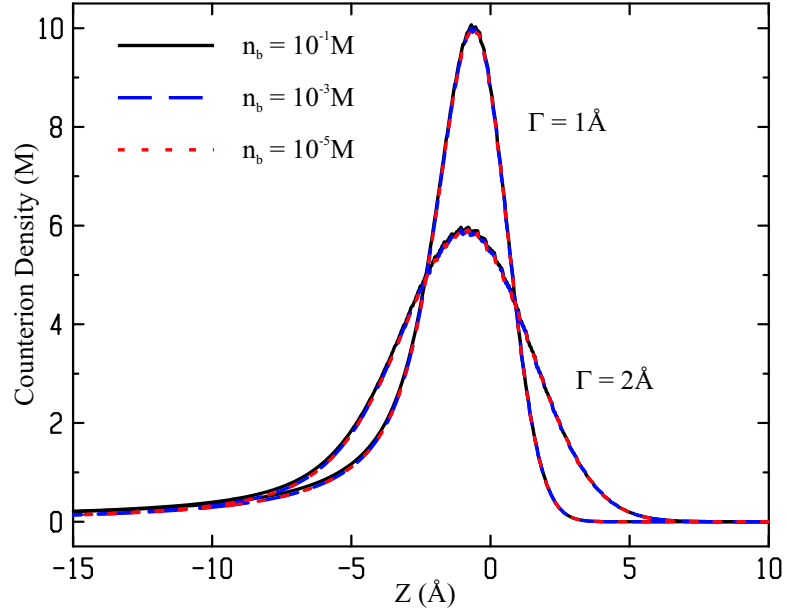
Figure 4.6   The convolutions of the distributions $n^+(z)$ from Eq. 4.4 as-
suming two Γ values as indicated. The theoretical distributions
are calculated from Eq. 1.9 by using $\sigma_s = -e/40\text{Å}^2$, $\epsilon = 80$,
$T = 293$ K, and n_b as indicated.

The convolution function is justified by the following assumption:(i) interface fluctuations are

Gaussian, and (ii) the wavelength of the capillary waves at the interface are larger than molecular

size. The width of the Gaussian Γ is dominated by surface roughness, which is independently

determined from the reflectivity. Figure 4.6 shows convolution of the theoretical distributions for

two different values of Γ as indicated. It is interesting to note that the convoluted calculations

are practically indistinguishable as a function of bulk salt concentration.

The second modification is the surface charge density, provided by the monolayer headgroups.

Each DHDP molecule has PO_4^- headgroup after dissociation with cross-section of $\sim 40\,\text{Å}^2$,

yielding $\sigma_s = -e/40\text{Å}^2$, used for all previous $n_+(z)$ calculations. However, in our system, one of

the ion species, the proton H^+, can bind to the interface and neutralize the charged headgroup,

and as a result, the surface charge density is reduced by a factor of α. That reaction can be

expressed by

$$H^+ + PO_4^- \Longleftrightarrow PO_4H,$$
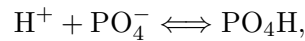
Table 4.3 Fractions of sites actually dissociated, α, for different bulk concentrations, n_b, using $pK_a = 2.1$, $pH = 6.6$ (within the range of uncertainty of the measured pH of our pure water), $\sigma_s = -e/41\text{Å}^2$, $\varepsilon_r = 80$, and $T = 293$ K.

n_b	10^{-5}	10^{-4}	10^{-3}	10^{-2}	10^{-1}
α	0.180	0.358	0.638	0.899	0.987

and the equilibrium condition is given by

$$\frac{[\text{H}^+]\left[\text{PO}_4^-\right]}{[\text{PO}_4\text{H}]} = K_a, \tag{4.5}$$

where the dissociation constant K_a is determined by the headgroup. The fraction of sites actually dissociated, α, defined by $\frac{[\text{PO}_4^-]}{[\text{PO}_4^-]+[\text{PO}_4\text{H}]}$, is related to K_a by

$$\alpha = \frac{1}{1 + 10^{(pK_a - pH)}},$$

with $pK_a = -\log(K_a)$. For DHDP monolayer material, its hydrogen-phosphate headgroup $(R - \text{PO}_4\text{H})$ has a $pK_a = 2.1$, presumably guaranteeing almost complete dissociation ($\alpha \approx 1$) for neutral $pH \sim 7$. However, when such molecules form an interface, in particular, one that is planar, the proton concentration becomes significantly higher than bulk at that interface, leading to a lower interfacial pH. Within the PB theory, the enhancement is expressed quantitatively by the Boltzmann factor $\text{e}^{-e\psi(0)/k_BT}$, which could be significantly larger than k_BT for a highly charged surface. Then, the fraction of sites actually dissociated is

$$\alpha = \frac{1}{1 + 10^{(pK_a - pH)}\text{e}^{-e\psi(0)/k_BT}}. \tag{4.6}$$

The potential at the interface, $\psi(0)$, which can be influenced by ion concentration in a solution, is determined self-consistently from the boundary-condition equation

$$\sinh\left(\frac{e\psi(0)}{2k_BT}\right) = -\left(\frac{\lambda_D}{\lambda_{GC}}\right)\frac{1}{1 + 10^{-(pH - pK_a)}\text{e}^{-e\psi(0)/k_BT}}. \tag{4.7}$$

Numerical solution of $\psi(0)$ from Eq. 4.7 yields α for any given pK_a, n_b, and σ_s. As an example, αs for DHDP headgroup and several different ionic bulk concentrations are listed in Tab. 4.3.

As a sequence, the real surface charge density is given by $\sigma_r = \alpha\sigma_s$, where σ_s is the maximum charge density monolayers can provide (i.e., all headgroups are dissociated). The counterion
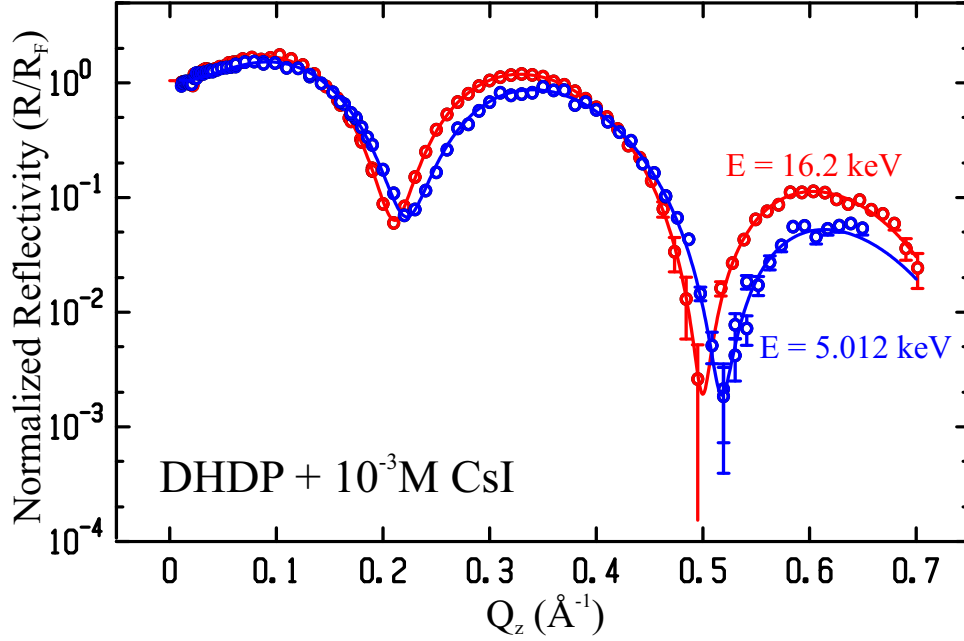
Figure 4.7   Normalized X-ray reflectivities measured at 16.2 and 5.012 keV
for DHDP monolayer spread on 10^{-3} M CsI solution ($\pi = 40$
mN/m). The solid lines are calculated reflectivities using the
ED and AD profiles shown in Fig. 4.9(A). The two data sets
were combined and refined to a model with common structural
adjustable parameters.

distribution is given by the PB theory with a renormalized Gouy-Chapman length $\lambda'_{GC} = \lambda_{GC}/\alpha = 2\varepsilon_0\varepsilon_r k_B T/|\sigma_r|e$, and expressed as

$$n_+(z) = n_b \left(\frac{1 + \gamma e^{z/\lambda_D}}{1 + \gamma e^{z/\lambda_D}} \right)^2, \tag{4.8}$$

with $\gamma = -\lambda'_{GC}/\lambda_D + \left((\lambda'_{GC}/\lambda_D)^2 + 1 \right)^{1/2}$. The renormalized surface charge density σ_r with PB theory is hereafter RPB theory. Clearly, for the monolayers at the surface, the surface charge density is not only dependent on the molecular area, but the bulk concentrations. It further implies that the counterion distribution actually depends on the bulk concentration, in a qualitative agreement with reflectivity data off resonance.
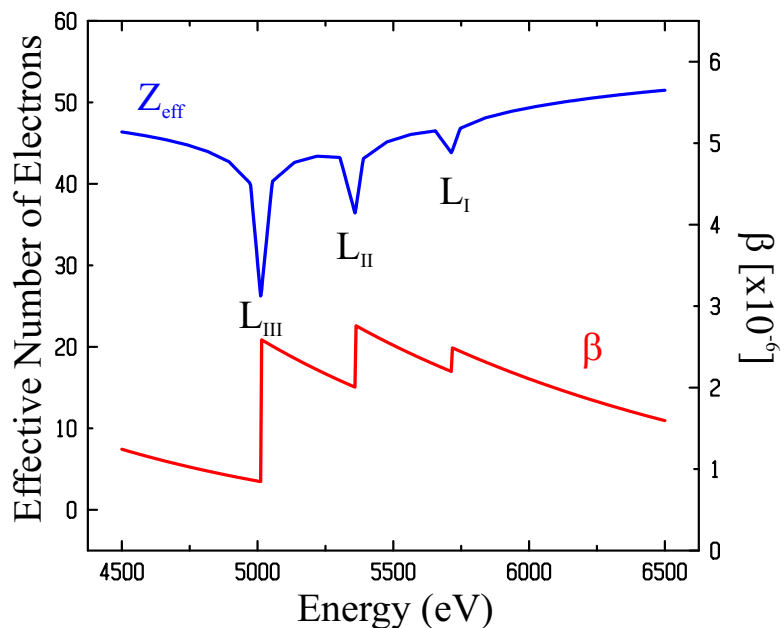
Figure 4.8   Effective number of electrons and the absorption factor β
for Cs^+. $Z_{eff} = \rho'/n$, where n is the number density and
$\beta = \lambda^2 \rho'' r_0 / 2\pi$. The mass density used for β calculation is
$1.87\,g/cm^3$.

4.5   Anomalous Reflectivity

Figure 4.7 shows reflectivities of DHDP spread on 10^{-3} M CsI for $\pi = 40$ mN/m at 16.2
and 5.012 keV (Cs L_3 edge). The reflectivity taken at 16.2 keV has sharper and deeper minima
that are slightly shifted to smaller Q_z, compared to the reflectivity taken at 5.012 keV. This is
due to the dependence of ρ_i' and ρ_i'' on the X-ray energy. At these two different energies the
measurements were conducted (16.2 and 5.012 keV), ρ' and ρ'' dramatically change only for
cesium (as shown in Fig. 4.8) and slightly for the phosphorous ion, whereas for the remaining
constituents, the binding energies are smaller than 5.012 keV and therefore all electrons behave
as free electrons. The significant drop of ρ' for Cs at its L_3 edge reduces the thickness and
electron density of headgroup and Cs slabs (see Fig. 4.9(A)), yielding the difference in the
X-ray reflectivity data between 16.2 to 5.012 keV. Or, in other words, that difference shown in
Fig. 4.7 provides the evidence for the existence of large amount of Cs at the surface.

Here we apply stage two of the analysis, each slab is associated with a portion of the molecule,

and the ED's and AD's are calculated self consistently by applying volume constraints. Thus, the ED of the hydrocarbon slab is given by

$$\rho'_{tail} = N_{tail}/d_{tail}A \tag{4.9}$$

and

$$\rho''_{tail} = 0, \tag{4.10}$$

where $N_{tail} = 258$ is the total number of electrons in the two acyl chains [78]. Similarly, we can calculate ρ_i for the headgroup and for the Cs^+ as follows,

$$\rho'_i = \left(N_{Cs^+}Z_{Cs^+} + N_{H_2O}Z_{H_2O} + N_{PO_4^-}Z_{PO_4^-}\right)/d_iA, \tag{4.11}$$

$$\rho''_i = \left(\mu_{Cs^+}N_{Cs^+}/\rho_{0_{Cs}} + \mu_P N_{PO_4^-}/\rho_{0_P}\right)/2d_iA\lambda r_0, \tag{4.12}$$

where N_j is the number of ions or molecules, Z_j is the number of electrons per ion or molecule, μ_j is the linear absorption coefficient of the material when the density of material is ρ_{0_j}. $N_{PO_4^-}=1$ in the headgroup slab and $N_{PO_4^-}=0$ in the Cs slab (see Fig. 4.5).

Using ρ'_i, ρ''_i, and Eq. 4.3, we can create the generalized density $\rho(z) = \rho'(z) - i\rho''(z)$, which includes both the electron density and the absorption density. We then apply the following volume constraints

$$d_iA = N_{Cs^+}V_{Cs^+} + N_{H_2O}V_{H_2O} + N_{PO_4^-}V_{PO_4^-}, \tag{4.13}$$

where, $V_{H_2O} = 30\,\text{Å}^3$, $V_{PO_4^-} = 60\,\text{Å}^3$ (calculated from the reflectivity of DHDP on water), and $V_{Cs^+} \approx 20\,\text{Å}^3$ (calculated from the ionic radius in standard tables). In the first stage of analysis, each slab has two free parameters: ρ_i and d_i besides the roughness. For the second stage, chain slab has two parameters: A and d_{tail} (see Eq. 4.9), same as the first stage. On the other hand, headgroup and Cs slabs have three parameters: d_i, N_{Cs^+}, and N_{H_2O} according to Eq. 4.11. However, one of them can be eliminated by the volume constrains (Eq. 4.13); therefore, the second stage does not introduce more parameters than the first stage. The advantage of this method is that a unique set of parameters is used to fit both reflectivities at and off resonance simultaneously, thus providing a strong self-consistency test to the analysis. This is very similar
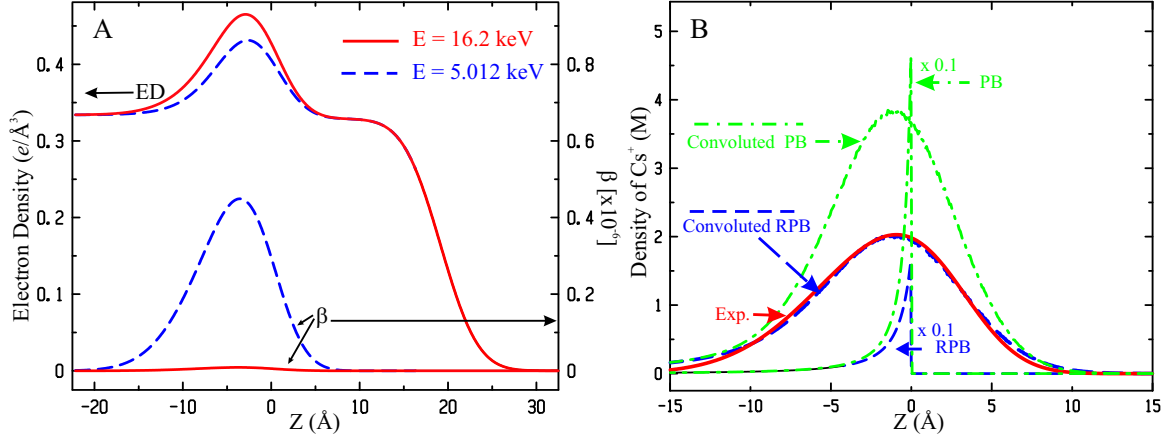
Figure 4.9   (A) ED profiles extracted by the reflectivity data shown in Fig. 4.7. Also shown is the profile of absorption factor β, which at 5.012 keV is dominated by the presence of Cs^+ close to the interface. (B) Solid smooth line is the distribution of Cs^+ determined from the reflectivity measurements as described in text. The dashed lines are the ion distribution calculated from the RPB equation with the corrected surface charge density due to hydronium affinity to PO_4^-, and RPB result convoluted with a Gaussian of width given by the average surface roughness of the monolayer obtained from XR without any adjustable parameters. Similar PB and convoluted PB predictions by assuming all headgroup dissociated are shown by dashed-dotted lines. PB and RPB calculations are divided by 10 for fitting the figure scale appropriately.

Table 4.4   Best-Fit Parameters to the data sets, in which the reflectivities measured at and off resonance are combined, for various slat concentrations at $\pi = 40$ mN/m.

subphase(CsI)	10^{-5} M	10^{-4} M	10^{-3} M	10^{-2} M	10^{-1} M
d_{tail} (Å)	19.6	19.8	19.2	18.8	20.2
d_{head} (Å)	3.2	3.7	3.8	6.7	4.3
N_{Cs^+}[1]	0.002	0.013	0.270	0.511	0.523
d_{Cs} (Å)	9.5	4.7	3.3	6.9	4.2
N_{Cs^+}[2]	0.119	0.288	0.289	0.187	0.410
A (Å^2)	41.00	41.04	40.97	41.00	42.08
total N_{Cs^+}[3]	0.12(5)	0.30(7)	0.56(10)	0.70(12)	0.93(12)

[1] Number of Cs^+ in the headgroup slab. [2] Number of Cs^+ in the Cs slab. [3] estimated errors are given in parentheses.

to the approach developed to determine the structure of a phospholipid monolayer by refining neutron and X-ray reflectivities simultaneously [75, 76].

The solid lines in Fig. 4.7 are calculated from the generalized density $\rho(z)$, obtained from parameters of a single model structure for the combined data sets, as shown in Fig. 4.9(A). The best fit structural parameters obtained by this method for various concentrations of CsI in solution are listed in Table 4.4. The absorption factor β shown in Fig. 4.9(A) can be converted to ρ'', AD curve, by a factor ($\beta = \lambda^2 \rho'' r_0 / 2\pi$). The AD curve for 5.012 keV up to a normalization factor is practically the profile of the counterion Cs^+ close to the interface (there is a minute contribution to the AD from phosphorous in the headgroup region, as shown in Eq. 4.12). The difference between the ED's at and off resonance, normalized by $Z_{eff}(16.2\,\text{keV}) - Z_{eff}(5.012\,\text{keV})$ [47], gives the desired ionic distribution at the interface. Figure 4.9(B) shows (solid line) the experimental Cs^+ distribution close to the interface at 10^{-3} M CsI. Similar distributions corresponding to other bulk CsI concentrations are shown in Fig. 4.10(A) (solid lines).

4.6   Comparison of Experimental Results With Theory

4.6.1   Ion Distributions

We first compute the integrated number of Cs^+ per DHDP over the first 15 Å next to the charged interface. This number can be obtained by integrating the experimental distribution along the z-axis and can be checked self-consistently from the model used in the analysis of the combined data set (Table 4.4). The number of ions per DHDP versus CsI bulk concentration are plotted in Fig. 4.10(B) with square symbols. In Fig. 4.10(B), the integrated values obtained by PB theory with the surface charge corresponding to the fully deprotonated phosphate groups are also plotted (dashed line) as for comparison. As shown, the experimental integrated number of Cs^+ at the interface varies roughly as a power-law of bulk concentration, which is well described with RPB (solid line) without fitting parameters.

The ion distribution predicted from RPB theory using Eq. 4.8 with the renormalized Gouy-Chapman length is compared with the experimental distribution in Figs. 4.9(B) and 4.10(A)
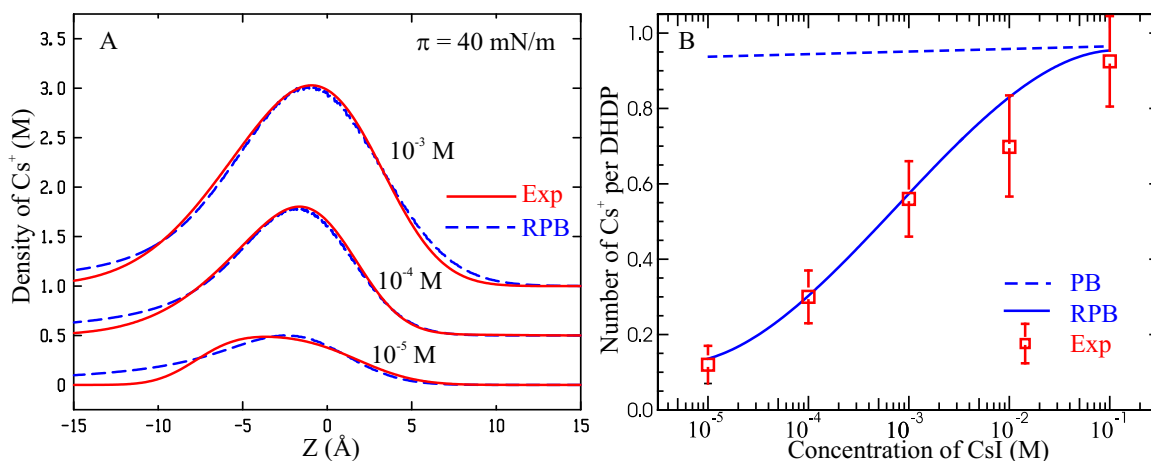
Figure 4.10 (A) Interfacial Cs^+ distributions (solid lines) determined from anomalous reflectivities (at 16.2 and 5.012 keV) for various CsI bulk concentration (shifted by 0.5 M for clarity). Calculated and convoluted distributions based on RPB with renormalized surface charge density as described in the text, are shown as dashed lines. (B) Square symbols are numbers of Cs^+ ions per DHDP ($\approx 41\,\text{Å}^2$) by integrating (up to $15\,\text{Å}$) the experimental distribution obtained from the anomalous scattering for 10^{-5}, 10^{-4}, and 10^{-3}M. For 10^{-2} and 10^{-1}M, the integrated number of ions are determined from the reflectivities off resonance only (the reflectivities at resonance for these concentrations were not measured). The dashed line and the solid line are obtained from PB theory and RPB theory, respectively.

(dashed lines). As discussed above, the theoretical distribution needs to be convoluted with the effective experimental resolution function. The distribution resulting from the convoluted RPB, with no fitting parameters, with $\Gamma \approx 3.8\,\text{Å}$ obtained from the analysis of the reflectivity, is shown to reproduce the experimental data remarkably well, as shown in Fig. 4.9(B). The value for $pH - pK_a = 4.5$, used in the calculation, is consistent within the range of our measured values for the $pH \sim 6.6$.

The distributions corresponding to the three bulk Cs^+ concentrations $10^{-3}, 10^{-4}$, and 10^{-5} M are shown in Fig. 4.10(A) with solid lines. The agreement with the RPB (dashed lines) convoluted as described is remarkable except for points far from the interface. We attribute this error to the difficulty to include slowly decaying tails of the PB theory to the ED profile

modeled by the faster decaying Error functions.
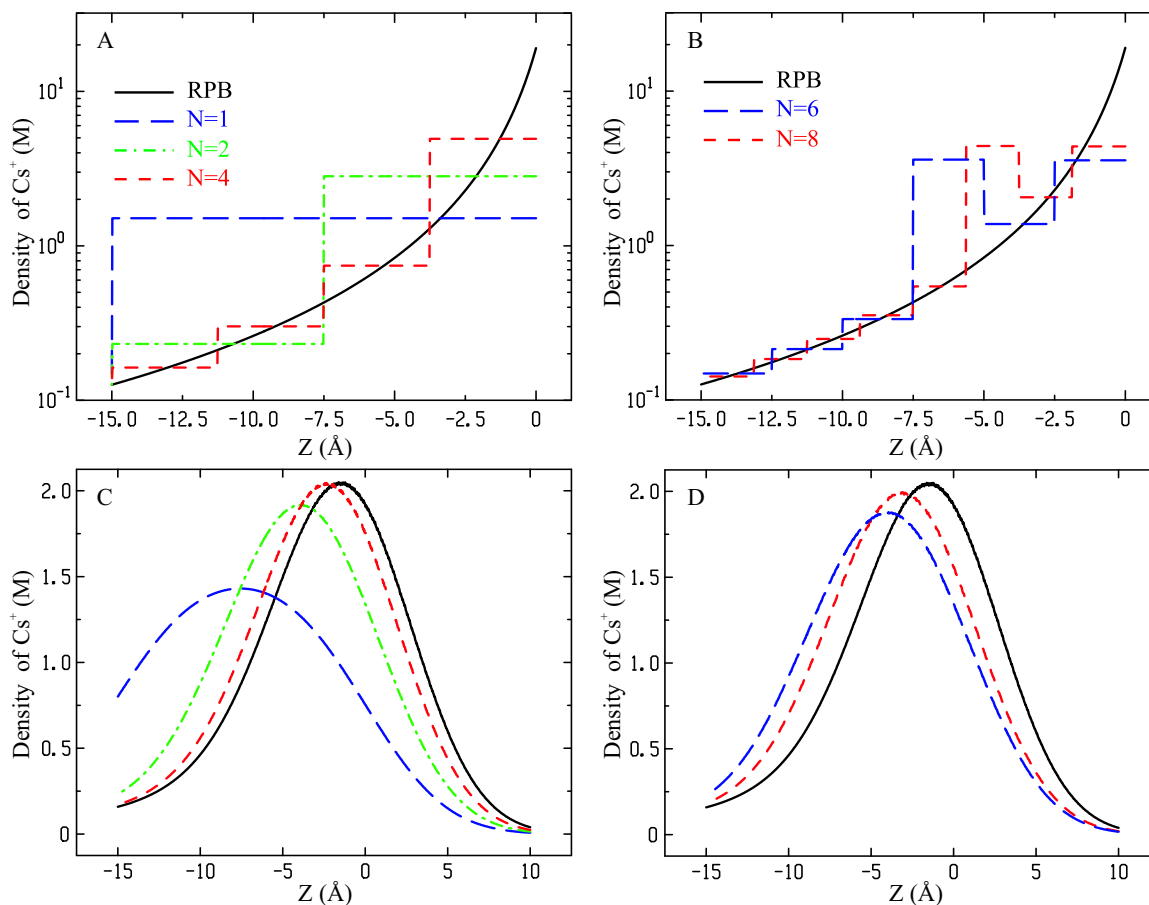
Figure 4.11   (A), (B) Solid line corresponds to the RPB profile at bulk concentration 10^{-3} M. Step-like monotonic (A) and non-monotonic (C) functions preserve the integral (up the first 15 Å) of the continuous RPB distribution. (C) and (D) are convoluted results with a Gaussian of width $\Gamma = 3.8$ Å from the distributions shown in (A) and (B), respectively.

4.6.2   Possible Deviations from PB Theory Distributions

This section deals with the examination of sensitivity of the anomalous reflectivity in determining the ion distribution, in addition to the integrated number of ions at the interface. The results presented in Fig. 4.10(A) show the unique capability of the anomalous reflectivity technique in providing ion distributions. Whereas the integrated number of ions, such as the ones shown in Fig. 4.10(B), can be obtained from standard reflectivity measurements and other

experimental techniques, as discussed in Chapter I, the determination of ion distributions requires the use of anomalous reflectivity. In fact, data such as shown in Fig. 4.10(B) has been used to assess the validity of PB theory in the past. As discussed in Chapter I, the excellent agreement maybe somewhat deceptive in that it may hide significant short distance deviations from RPB theory because only the total integrated ion density is involved.

Figure 4.11(A) shows counterion distribution from RPB theory at bulk concentration 10^{-3}M, and three step-like monotonic functions ($N = 1$, $N = 2$, and $N = 4$ steps of 15, 7.5 and 3.75 Å width, respectively) preserving the integral (up the first 15 Å) of the RPB distribution. The corresponding convoluted results with a Gaussian function of width $\Gamma = 3.8$ Å are shown in Fig. 4.11(C). Step-wise distributions with large width (> 3.8 Å; i.e., $N = 1$ (long-dashed line) and $N = 2$ (dashed-dotted line)) are quite different from the convoluted RPB (solid line). However, when the step width is comparable to or less than convolution width, Γ, the convoluted step-wise distribution ($N = 4$; short-dashed line) is practically identical with the convoluted RPB after proper shift along z-direction (see Fig. 4.11(C)). Therefore, our experimental resolution constrain possible deviations from RPB distributions to within 3.8 Å, the surface roughness. If such deviations are non-monotonic, showing bumps or oscillations, then the constraints are even more stringent. As an example, in Fig. 4.11(B) we construct two step-wise distributions ($N = 6$ and $N = 8$ steps of 2.5 and 1.9 Å width, respectively) whose total integrated area is the same as for RPB (solid line). Although the histograms have the same area as the RPB, they incorporate hypothetical non-monotonic decay of the distribution in the form of bumps. As it is shown in Fig. 4.11(D), despite the fact that the step-size are smaller than 3.8 Å, such distributions can be ruled out by the experiments. This demonstrates that if actual ion distributions are non-monotonic, their maxima or minima must be short-ranged in nature (shorter than ≈ 2 Å) to be consistent with our data.

4.7   Summary

The goal of this study was to explore the accuracy of PB theory for monovalent ions. For that, we selected a system with a relatively high surface charge density (one electron per 40 Å^2,

lattice constant ~ 6.8 Å) and a low $pK_a = 2.1$ system, which we expected would provide the most favorable scenario to observe deviations from PB theory. From the results obtained in our experiments, we conclude that PB with the renormalization of surface charge density due to proton-transfer and release processes (RPB) is strikingly accurate.

Certainly, the accuracy of our results is limited by the effective experimental resolution, which is dominated by the natural surface roughness of the air/liquid interface (≈ 3.8 Å), due mainly to thermally activated capillary waves. We should point out, however, that this resolution is comparable to the diameter of one Cesium ion (3.2 Å) or a single water molecule (~ 3 Å), and therefore our experimental distributions constrain deviations from RPB theory to very short-range variations involving one, at most two, water molecules or cesium ions. If the actual ionic distribution is non-monotonic, departures from RPB theory are even more constrained as it follows from the discussion in Fig. 4.11.

Our results show that theoretical effects that are usually suggested to modify PB theory, such as finite ion-size, in-plane modulations of surface charge density, hydration forces, short-range interactions, and the roughness of the surface or image charges are not necessary to describe the experimental data. This is not to be understood as implying that such effects are not present, but rather that their significance is entirely limited to a characteristic spatial distance of the order of ≈ 4 Å or less. As for claims based on the modification of PB by hydration forces (see for example, Ref. [14]), our experimental results conclusively rule out the possibility of modifications of PB within the $10 - 20$ Å range from the interface and confine such corrections, if present, to within the first $3 - 4$ Å from the interface as discussed. Although the experimental counterion distributions are well described within the RPB theory, we point out that the reflectivity and GIXD hint at water restructuring at the interface. Future theoretical or numerical work may clarify this issue.

A recent report analyzing the accuracy of PB near charged liquid-liquid interfaces by the use of X-ray surface sensitive techniques shows that ion distributions are well described by PB at concentrations of 10 mM, but marked deviations are found at higher concentrations (of the order 100 mM), where ion-ion correlations have to be included in the theoretical analysis [86].

We did not perform anomalous reflectivity for concentrations above 10mM, so we are not able to provide ionic distributions for these concentrations. We point out, however, the good agreement found for the integrated quantities at these concentrations (Fig. 4.10(B)), which provides an example of integrated quantities possibly hiding deviations from actual distributions as pointed out in Chapter I.

The results presented in this study enhance our understanding of the electrostatics in aqueous media and also show the strength of surface sensitive X-ray synchrotron techniques in obtaining high resolution data.

CHAPTER 5.   ION DISTRIBUTIONS AT CHARGED AQUEOUS SURFACES BY NEAR RESONANCE X-RAY SPECTROSCOPY

In previous chapter, we reported the monovalent counterion distributions near a charged surface extracted by the anomalous reflectivity technique. The experimental results for various bulk concentrations are in excellent agreement with a renormalized surface charge PB (RPB) theory without fitting parameters or additional assumptions. In this Chapter, we used an independent technique, near resonance X-ray spectroscopy, to explore the same subject.

Again, monolayer material DHDP was spread on 10^{-3} M CsI, providing a uniformly charged surface. Energy scans at fixed momentum-transfers under specular reflectivity conditions near the L_3 Cs$^+$ resonance reveal the formation of a diffuse Cs$^+$ rich layer at a charged surface. The energy scans exhibit periodic dependence on photon momentum transfer (Q_z) with a line shape that consists of a Q_z-dependent linear-combination of the dispersive $f'(E)$ and absorptive $f''(E)$ fine-structure corrections. We discuss the results in the Born approximation and more quantitatively by using the dynamical method numerically (i.e., recursive or matrix methods to calculate the reflection of electromagnetic waves from stratified media). The ion distributions obtained from the analysis of the spectroscopy are in excellent agreement with those obtained from anomalous reflectivity measurements, providing further confirmation to the validity of the RPB theory for monovalent ions.

In addition to ion distributions, energy scans also yield the fine-structures of $f'(E)$ and $f''(E)$ near a resonance, which we find shed light on the local environment of the non-crystalline ions. In the past, the dispersion corrections were obtained by Bijvoet Pairs at Bragg reflections [87], by absorption cross-section measurements [88, 89], and by calculation using atomic wave functions [90]. Our results for the dispersion corrections differ significantly from the multi-
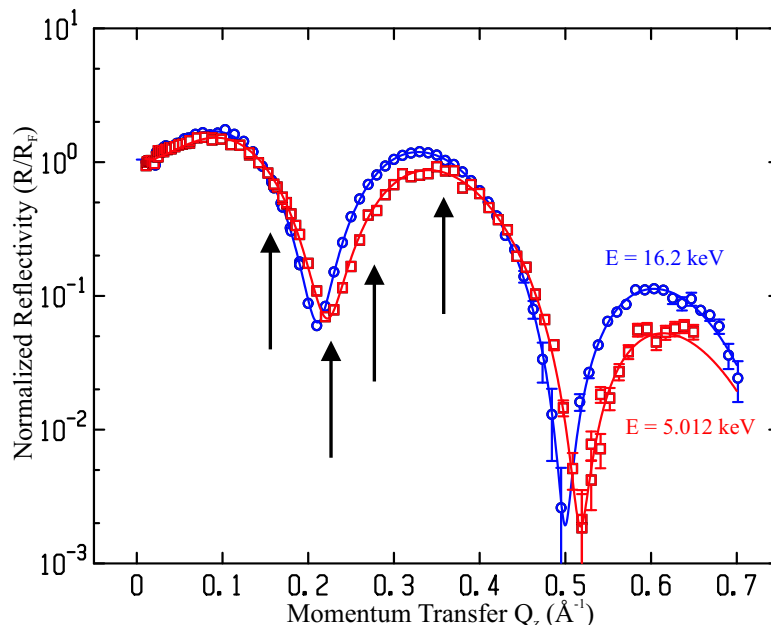
Figure 5.1   Normalized X-ray reflectivities measured at 16.2 keV (circles) and 5.012 keV (squares) of DHDP monolayer spread on 10^{-3} M CsI solution ($\pi = 40$ mN/m). Arrows indicate the selected momentum transfers at which energy scans were measured. Solid lines are best fits to the data.

electron photoexcitation spectra of the isolated ion, revealing the local environment of a Cs^+ ion in the solution at the interface. The comparison with similar X-ray absorption fine structures suggests that the Cs^+ ion is surrounded by a shell of eight oxygen atoms.

5.1   Experimental Data from Energy Scans

Figure 5.1 shows normalized reflectivity curves, R/R_F versus Q_z, for DHDP (surface pressure, $\pi = 40$ mN/m) spread on 10^{-3} M CsI solution measured at and off the Cs L_3 resonance (at 5.012 keV and at 16.2 keV, respectively; R_F is the calculated reflectivity of an ideally flat gas/water interface). The minima of the reflectivity measured at the Cs resonance are slightly shifted to larger Q_z, suggestive of a smaller effective film-thickness compared to that measured off resonance. This is due to the reduction in the effective number of electrons near the resonance, which is also responsible for the overall intensity reduction compared to the one measured away from resonance. As described in more detail in Chapter IV, the generalized density $\rho(z)$

can be extracted from the two reflectivities as shown in Fig. 5.3 for $\rho'(z)$. From the difference between the two ED's obtained at two energies, we can quantify the spatial distribution of Cs^+ at the interface. It has been shown that this distribution is in good agreement with the renormalized surface charge density Poisson Boltzmann theory after convolution with the experimental resolution function, as shown in Fig. 5.3.
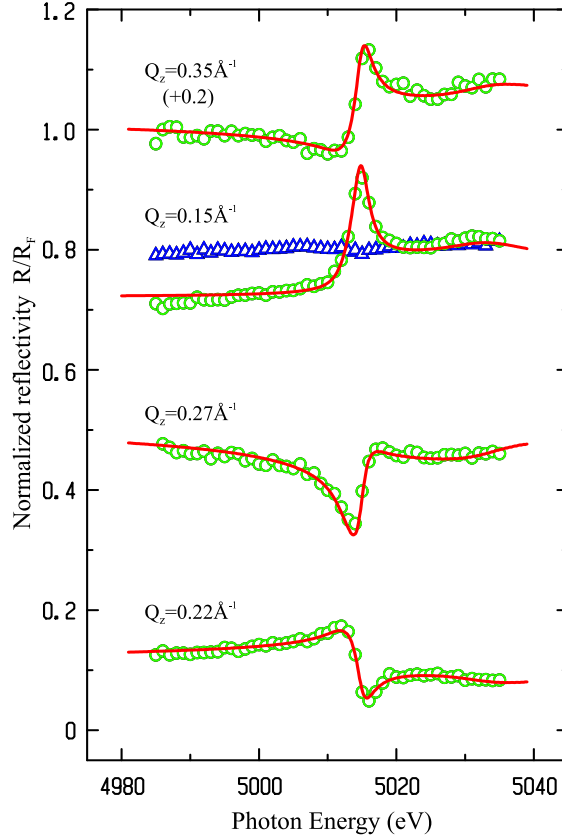
Figure 5.2   Energy scans at fixed momentum transfers (as indicated, see Fig. 5.1) Q_zs near the Cs L_3 edge of a DHDP monolayer spread on 10^{-3} M CsI solution ($\pi = 40$ mN/m). Solid lines are best fits to the data as described in the text (energy scan at $Q_z = 0.35\,\text{Å}^{-1}$ is offset vertically for clarification). Energy scan of CsI solution surface (10^{-3} M) at $Q_z = 0.15\,\text{Å}^{-1}$ (triangles) do not detect any anomalies in the absence of interfacial charges, i.e., with no monolayer.

Figure 5.2 shows normalized reflectivities (R/R_F) at fixed momentum transfer Q_zs *versus* incident photon energies measured near the Cs L_3 resonance. Similar reflectivity measurements
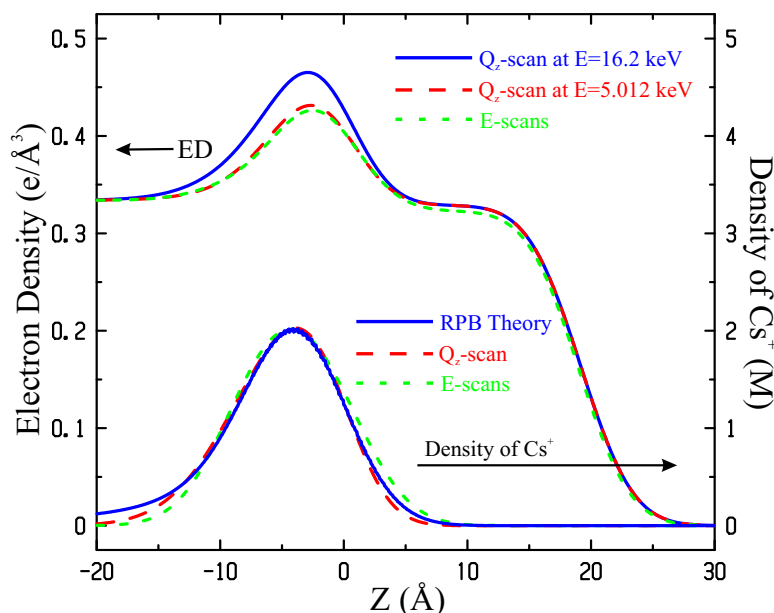
Figure 5.3   Electron densities obtained from the reflectivities (Q_z-scan) shown in Fig. 5.1 at 16.2 keV and 5.012 keV, and from the combined energy scans (E-scan) shown in Fig. 5.2 also calculated at the resonance. Spatial Cs^+ distributions determined from the anomalous reflectivity measurements (dashed line) and energy scans (dotted line). The solid line is obtained from renormalized surface charge PB theory (RPB) after convolution with the experimental resolution function as discussed in previous Chapter.

performed on the CsI solution (10^{-3} M, in the absence of a monolayer) did not reveal any anomalies in the reflected beam as a function of photon energy, as shown (triangles) in Fig. 5.2 for $Q_z = 0.15$ Å^{-1}. However, with the DHDP monolayer on the surface, the energy scan at the same momentum transfer ($Q_z = 0.15$ Å^{-1}) shows a huge peak around the Cs L_3 resonance, implying significant amount of Cs^+ accumulating on the surface. The DHDP monolayer containing the $R - PO_4H$ headgroup, with its strong proton dissociation constant ($pK_a = 2.1$), provides negative surface charges attracting a sufficient number of Cs^+ counterions, giving rise to the spectra observed. Based on the experimental setup, we estimate the signal originates from $\approx 5 \times 10^{13}\, Cs^+$ ions ($\approx 10^{-8}\,$g Cs spread over $0.4\,$cm^2 of the beam footprint). Furthermore, we did not detect any signal in energy scans around the I L_3 absorption edge (4.557 keV) at fixed Q_z. This is clear evidence that the concentration of I^- is in fact depleted with respect to

that of the bulk at the surface.

5.2   Analysis by Born Approximation

The spectra shown in Fig. 5.2 systematically exhibit opposite characteristics for each two points separated by $\Delta Q_z \approx 0.125$ Å^{-1}(i.e., $Q_z = 0.15$ and 0.27 Å^{-1}; $Q_z = 0.22$ and 0.3 Å^{-1}). To explain these features semi-quantitatively, we assume for simplicity that the monolayer ED consists of two slabs (as shown in Fig. 5.4), one of thickness d_1 and electron density ρ_c associated with the hydrocarbon chains ($\rho_c \approx \rho_s$, the subphase ED, ρ_s, is almost the same as that of closely packed hydrocarbon chains). The second slab of thickness d_2 is associated with the headgroup and hydrated Cs$^+$ ion distribution ($d_2 = d_{head} + d_{Cs}$), with a complex ED $\rho_h + \rho_{Cs}(f' + if'')$ ($\rho_{Cs} = Z_{Cs}N_{Cs}$; N_{Cs} is the number of Cs ions per molecule; $f'(E)$ and $f''(E)$ are dispersion corrections for Cs). For this energy scan range, from 4980 to 5040 keV, we can assume dispersion coefficients f' and f'' are energy dependent only for Cs and constant for other elements in our studying system.
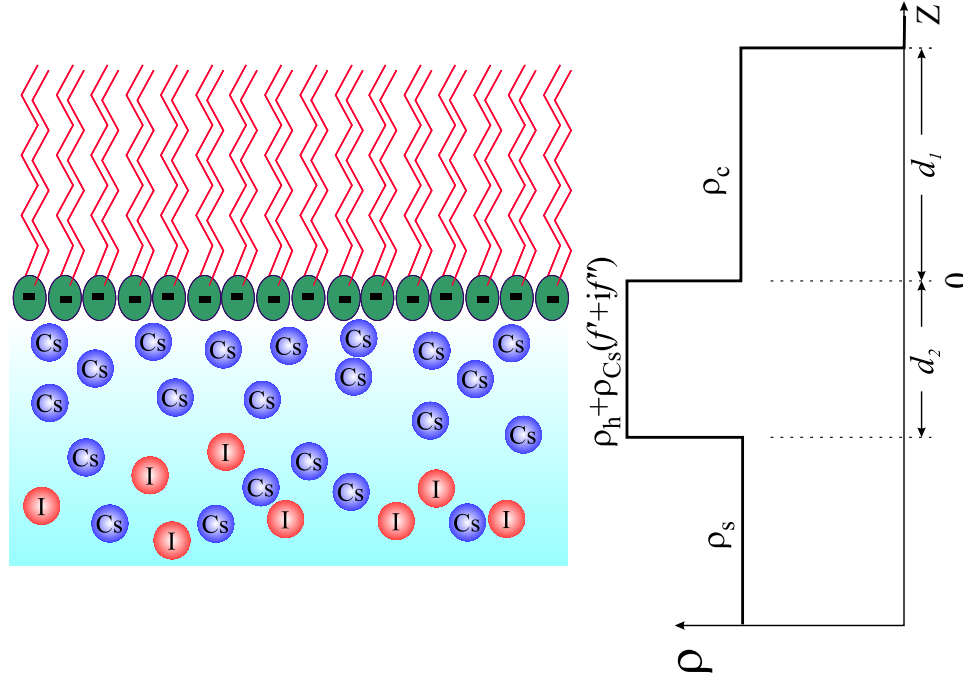
Figure 5.4   Simplified step-like electron density profile used to calculate the reflectivity in the Born-Approximation as explained in text.

In the Born approximation, the reflectivity from the film is given by [53, 22],

$$R(Q_z, E) = \frac{R_F(Q_z)}{\rho_s^2}\left|\int \frac{d\rho(z,E)}{dz}e^{-iQ_z z}dz\right|^2,\tag{5.1}$$

valid for $Q_z \gg Q_c$, where $Q_c = 4\sqrt{\pi\rho_s r_0} \approx 0.0217 \text{ Å}^{-1}$ is the critical momentum transfer for total external reflection. Substituting the generalized electron density profile

$$\rho(z,E) = \begin{cases} 0 & z > d_1 \\ \rho_c & 0 < z \leq d_1 \\ \rho_h + \rho_{\text{Cs}}(f' + if'') & -d_2 < z \leq 0 \\ \rho_s & z \leq -d_2 \end{cases}\tag{5.2}$$

into Eq. 5.1 and assuming $\rho_c = \rho_s$ yield

$$\frac{R(Q_z, E)\rho_s^2}{R_F(Q_z)} = \left|\rho_c e^{-iQ_z d_1} + (\rho_h + \rho_{\text{Cs}}(f' + if'') - \rho_c) - (\rho_h + \rho_{\text{Cs}}(f' + if'') - \rho_c)\, e^{iQ_z d_2}\right|^2$$

$$\simeq \rho_c^2 + (\rho_h - \rho_c)^2(2 - 2\cos(Q_z d_2)) + 4\rho_c(\rho_h - \rho_c)\sin(Q_z\bar{d})\sin(\frac{Q_z d_2}{2})$$

$$+ 4\rho_c\rho_{Cs}(f'\sin(Q_z\bar{d}) + f''\cos(Q_z\bar{d}))\sin(\frac{Q_z d_2}{2}),\tag{5.3}$$

where $\bar{d} = d_1 + d_2/2$. The last term in Eq. 5.3 predicts that a linear combination of $f'(E)$ and $f''(E)$ is superimposed on the reflectivity from the monolayer at energies away from the resonance. Separating the energy dependent term from others gives

$$R(Q_z, E) \simeq A(Q_z) + B(Q_z)(f'\sin(Q_z\bar{d}) + f''\cos(Q_z\bar{d})),\tag{5.4}$$

where A and B are constant for energy scans at fixed Q_z. The term, $f'\sin(Q_z\bar{d}) + f''\cos(Q_z\bar{d})$, gives the energy scans periodic dependence on photon momentum transfer (Q_z), with a line shape that resembles a superposition of the dispersive $f'(E)$ and absorptive $f''(E)$ fine-structure corrections. Furthermore, the resonant contribution of any point Q_{zi} is exactly opposite in sign for any other point Q_{zj} for which $(Q_{zi} - Q_{zj})\bar{d} = \Delta Q_z\bar{d} = \pi$, as we observe experimentally. This property yields $\bar{d} = \pi/\Delta Q_z \approx 25.1 \text{ Å}$. Using the literature value for $d_1 \approx 19.7 \text{ Å}$ [78] we obtain $d_2 \approx 10.8 \text{ Å}$ corresponding to the phosphate headgroup and hydrated Cs^+ compartment which is much larger than that found for a monolayer spread on pure water, $d_2 \approx 3.4 \text{ Å}$ [78]. This

unequivocally demonstrates Cs$^+$ ions accumulate, but do not bind to the phosphate headgroup at the interface, forming an extended (diffuse) layer much larger than the hypothetical bound Cs-phosphate. It is interesting to note that Eq. 5.4 counter intuitively indicates that the absorption term f'' can enhance the reflectivity, for $Q_z\bar{d} = \pi$ (noticing f'' has a negative value here), as evidenced in Fig. 5.2 for $Q_z = 0.15\,\text{Å}^{-1}$. More generally, Eq. 5.4 predicts that for $Q_z\bar{d} \approx 3\pi/2$ or $5\pi/2$ (i.e., $Q_z = 0.22$ and $0.35\,\text{Å}^{-1}$), the spectrum resembles $\mp f'_{Cs}(E)$; and if $Q_z\bar{d} \approx \pi$ or 2π (i.e., $Q_z = 0.15$ and $0.27\,\text{Å}^{-1}$) it resembles $\mp f''_{Cs}(E)$, consistent with our observations (see Figs. 5.2 and 5.5).

5.3   Analysis by the Dynamical Method

To provide a more quantitative account of the energy scans, we employ a more accurate method to calculate the reflectivity recursively [72] by slicing a parameterized generalized density profile, $\rho(z, E)$, and refining its parameters by nonlinear squares fit method. To include the energy dependent dispersion corrections near resonance, we construct the absorptive portion, $f''(E)$, as a sum of one Error function (of known step height from the literature [91]), and superimpose on it the minimum number of Lorentzians necessary to obtain an adequate fit and for which the addition of another one does not improve the quality of the fit. The dispersive portion, $f'(E)$, is numerically calculated by the Kramer-Kroning relation

$$f'(E) = \frac{2}{\pi}P\int_0^{+\infty}\frac{E'f''(E')}{E'^2 - E^2}dE'. \tag{5.5}$$

The integration is performed over a finite energy range using Simpson's rule. Integration by the Kramer-Kroning relation of f'' with close by anomalies ($\sim \pm 200\,\text{eV}$ away from the Cs L_3 resonance) do not affect the shape of f' near the resonance. To improve the reliability of the procedure, we use a single parameter set for the refinement of a combined data set consisting of all energy-scans at four different Q_z values. One should note that the spectra shown in Fig. 5.2 are given on an absolute scale. The solid lines in Fig. 5.2 are calculated with one set of parameters that best fit the combined data set.

The generalized density profile obtained from this procedure is consistent within error with
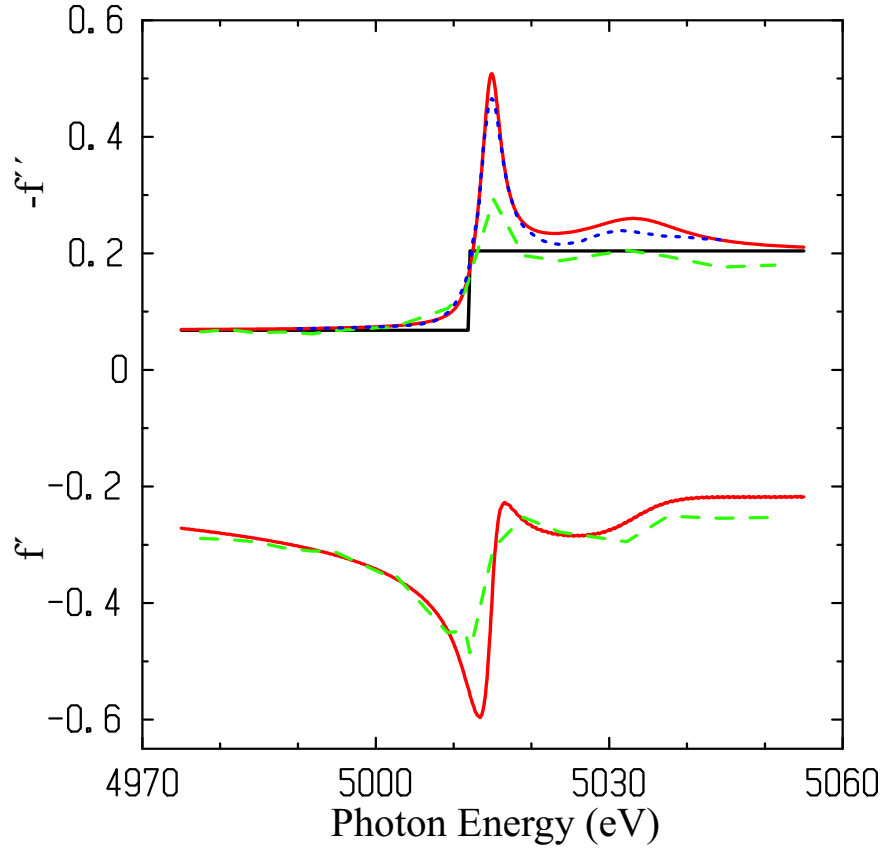
Figure 5.5   Dispersion corrections near the Cs L_3 edge. The solid lines are
derived from the best fit to the spectra shown in Fig. 5.2. The
dashed line was obtained from the Bijvoet-pairs measurements
of $CsHC_4H_4O_6$ single crystal [87], the dotted line was measured
by absorption of $CsNO_3/H_2O$ solution [89], and the step-like
function was calculated by Cromer and Libermann [90].

the one obtained from the Q_z-scan reflectivity as shown for the ED (real part) in Fig. 5.3
(dotted line). As described in previous Chapter, three energy dependent Error functions (i.e.,
chain, headgroup, and Cs^+ rich slabs) are used to construct the generalized density that best
fits the spectra. The centers of the Error functions define the average thicknesses of molecular
compartments in the film as follows: $d_{chain} = 19.5\,\text{Å}$ for the hydrocarbon chains, $d_{head} = 3.0\,\text{Å}$
for the headgroup, and $d_{Cs} = 7.1\,\text{Å}$ for the hydrated Cs^+ diffuse layer (our analysis indicates
partial protrusion of Cs^+ into the headgroup compartment). The combined thickness, $d_2 =
d_{head} + d_{Cs} = 10.1\,\text{Å}$, is in good agreement with the one extracted from the Born-approximation

calculation (10.8Å) as described above. Using these parameters we construct the ion distribution $N_{Cs^+}(z)$ (Fig. 5.3, dashed line), and obtain on average 0.58 integrated Cs^+ per lipid with approximately 11 water molecules in the headgroup and the Cs^+ compartments. The value agrees with the one obtained from Q_z-scan reflectivity (0.56 ± 0.1) and with the renormalized surface charge Poisson Boltzmann theory (RPB).

Figure 5.5 shows the dispersion corrections for Cs^+ near the L_3 edge extracted from the energy scans (solid lines), from the Bijvoet-pairs in $CsHC_4H_4O_6$ single crystal (dashed line) [87], from $CsNO_3/H_2O$ solution (dotted line) [89], and calculated step function [90]. Our extraction of $f''(E)$ shows an enhanced Lorentzian at resonance (so-called white-line, centered at 5013.33 ± 0.11 eV, height 0.32 ± 0.03, and width 1.49 ± 0.11 eV) and a second Lorentzian (centered at 5033.29 ± 0.19 eV, height 0.054 ± 0.003, width 7.91 ± 0.53 eV). We find that the absorption edge, defined as $\max(df''/dE)$, is at 5013.9 eV within the uncertainty of the values found in the literature 5012 eV [87, 88, 89]. The fine-structures of $f'(E)$ and $f''(E)$ obtained in the process differ significantly from the multi-electron photoexcitation spectra of the isolated ion [92], revealing the local environment of a Cs^+ ion in the solution at the interface. Although the edge we find agrees very well with that of the single crystal $CsHC_4H_4O_6$ [87], the overall features of $f'(E)$ and $f''(E)$ are significantly different. We argue this is due to the fact the local environment of Cs in the crystal consists primarily of hydrogen, whereas, the local environment of the ion in the present study consists of oxygen from the solution and the PO_4^- headgroup. Indeed, a recent XAFS study of $CsNO_3$ in water solution [89] exhibits f'' that is very similar to the one we obtained (Fig. 5.5). In that study, it was found that there are six nearest water molecules at an average distance 3.25 Å and another two at 4.0 Å [89, 93].

5.4   Summary

In the present study, we demonstrated that ion distributions close to a charged surface can be extracted from reflectivity spectra near an edge of a specific ion. This technique, can be used in conjunction with fixed energy reflectivity measurements to improve the reliability of the structural parameters. It also provides unequivocal evidence for the presence of minute

ion accumulation at aqueous interfaces. This ion-specific procedure has thus the advantage of showing the depletion of certain ions at the interface; in this study they show the depletion of the co-ions I^- at the interface. This technique is invaluable in distinguishing the distribution of ions from bound ones as expected [26, 94] for multivalent ions (such as Ba^{2+}, or La^{3+}) at charged interface.

In addition to ion distributions, this process is unique in providing, on an absolute scale, the dispersion corrections, which reflect the local environment of the probed ion. The local environment near the surface can be different from that of the bulk due to some effects such as the restructuring of the water at the surface. With the ability of probing the surface local environment, this technique is an excellent tool for investigating that difference.

CHAPTER 6.   X-RAY FLUORESCENCE SPECTROSCOPY FROM IONS AT CHARGED VAPOR/WATER INTERFACES

In the last two Chapters, we reported on the spatial distributions of monovalent ions (Cs^+) at highly charged interfaces at ~ 3 Å resolution by using synchrotron X-ray anomalous reflectivity techniques. We demonstrated that these distributions are well described by the Poisson-Boltzmann theory that accounts for the proton release and binding to a $R - PO_4H$ group (R is typically a fatty acid portion of the molecule). Subsequently, we reported on the extension of these studies by analyzing X-ray energy scans at fixed momentum-transfers (Q_z) under specular reflectivity conditions. In addition to obtaining ion distributions, our analysis yielded the energy dependence of the dispersion corrections $f'(E)$ and $f''(E)$ near the Cs^+ L_3 resonance. This study confirmed the ion density accumulations at the charged interfaces and provided spectroscopic information of the ions with details that shed light on the immediate environment of the ions, similar to that obtained by extended X-ray absorption fine structure spectroscopy (EXAFS) experiments.

The X-ray fluorescence near total reflection is another common technique to determine ion adsorption to charged Langmuir monolayers at the air/solution surface [23, 49, 50, 51, 95, 96, 97]. Herein, we report detailed determination of fluorescence spectra from monovalent ions Cs^+ in dilute solutions and as they form an ion rich layer near the charged interfaces. For the salt solution without the monolayer, the fluorescence signals below the critical angle are significantly lower than the detection sensitivity and only above the critical angle signals from the bulk are observed. In the presence of a monolayer that provides surface charges, strong fluorescence signals below the critical angle are observed. Ion density accumulated at the interface is determined from the fluorescence. We compare the findings with results obtained from the anomalous

reflectivity technique.

In this Chapter, we extend on previous studies by exploring the fluorescence signals as a function of photon energies, in particular, near resonances. As shown below, our approach yields the energy dependence of the dispersion corrections of Cs^+, $f'(E)$ and $f''(E)$, near a resonance, which are compared with results obtained from the energy scans. In general, EXFAS and related spectroscopic experiments are conducted in transmission configurations, but it is known that fluorescence experiments, as in this study, can yield similar results. The fluorescence data from divalent Ba^{2+} with and without monolayer are also presented.

6.1   Experimental Setup and Methods

In this study, monolayers materials DHDP and DMPA (also has PO_4^- head group) were both spread at salt (e.g., CsI and BaI_2) solution/gas interfaces [47, 78, 83], providing the uniformly charged surfaces. All X-ray fluorescence were conducted at the untilted phase of monolayers, implying that the molecular area is fixed at $41\pm1\text{Å}^2$. Vortex-EX Multi-Cathode X-Ray Detector (SII Nano Technology USA, Inc.), an energy dispersive detector (EDD), is lowered to the surface in an aluminum well with a thin Kapton window located ~ 2 cm above the liquid surface (Fig. 6.1). The Langmuir trough is placed in a sealed canister kept under a flow of water-saturated helium gas.

Fluorescence is an ion-specific technique in that it can distinguish contributions from different ions because of their characteristic fluorescence spectra [51, 96, 97]. Since the X-ray penetration depth changes dramatically (from $60 - 80 \text{ Å}^2$ to $1 - 2 \mu$m) around the critical angle ($Q_c \sim 0.022 \text{ Å}^{-1}$ for the total reflection), the fluorescence signals below and above the critical angle for all solutions in the present study are dominated by different regions of the systems. Below the critical angle, the signal is less sensitive to contributions from the pure bulk solution and in the presence of charges is dominated by ions at the surface, due to the finite penetration depth of X-rays. On the other hand, above the critical angle, the fluorescence signals consist of contributions from the ions in the bulk and at the interface.
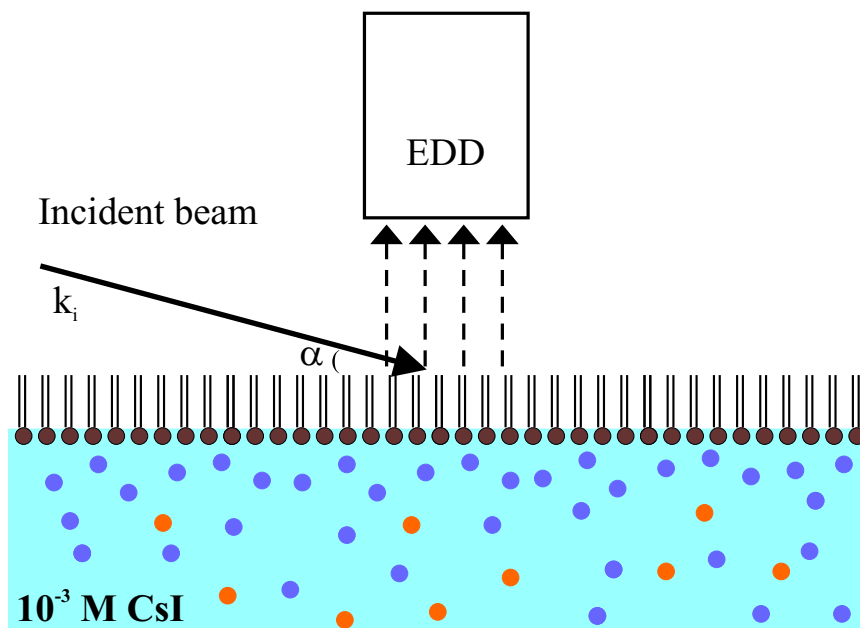
Figure 6.1   Illustration of the fluorescence experiment setup. The mono-
layer (DHDP or DMPA) is spread on 10^{-3}M CsI in an encap-
sulated Langmuir trough purged with water saturated helium.
The Vortex-EX Multi-Cathode X-Ray Detector window (50mm^2
effective detector area) is placed at a distance ~ 2 cm from the
surface. The fluorescent beam goes through a thin Kapton win-
dow that seals the trough.

6.2   Surface Ion Enrichment

Figure 6.2 shows contour plots of fluorescence intensity as functions of X-ray photon energy,

E, and momentum transfer, Q_z, for 10^{-3} M CsI with and without DHDP monolayer. Without

monolayer (Fig. 6.2(A)), the fluorescence pattern is relatively simple. Below the critical angle

$(Q_z < Q_c)$, no significant fluorescence intensity is observed, consistent with the fact that ions

(e.g., Cs$^+$, I$^-$) in the bulk are not concentrated enough to generate any detectable intensity

over the very short penetration depth. For this ion concentration (10^{-3} M), we can practically

claim that ions in the bulk have no contribution to the fluorescence signal in this Q_z range, or

that for this concentration the signal from the bulk is significantly lower than the sensitivity

of our detector. This is true at least for dilute concentrations ($\leq 10^{-3}$ M), but not for higher

concentrations as shown below. Above the critical angle $(Q_z > Q_c)$, the X-ray beam penetrates

Figure 6.2   Contour plots of fluorescence intensity for 10^{-3} M CsI without (A) and with monolayer DHDP (B). Emission lines are labeled on the right side. Incident X-ray beam energy is 8 keV.
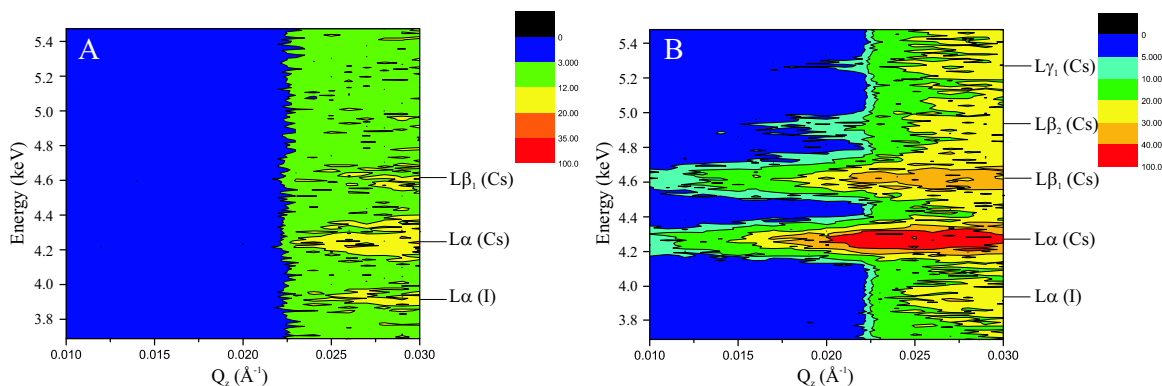
much deeper $(1 - 2\ \mu\text{m})$, and this concentration is sufficient to generate fluorescence signals. A few main emission lines from Cs^+ ($L\alpha$ and $L\beta_1$) and I^- ($L\alpha$) are clearly identified.

The fluorescence pattern with the DHDP monolayer (Fig. 6.2(B)) is significantly different from that of the bare surface below the critical angle, showing emission lines from Cs^+, but none from I^-. These emission lines include a few weaker ones ($L\beta_2$ and $L\gamma_1$), not observed from the bulk of the pure solution (Fig. 6.2(A)). This is qualitative evidence that Cs^+ exclusively adsorbs at the negatively charged surface. No emission lines from I^-, including the strongest $L\alpha$, are observed below the critical angle. This implies that within the uncertainty of our measurement (about 0.1 ions per DHDP molecule) there is no enrichment of I^- at the interface. Using DMPA as a monolayer yields essentially the same fluorescence patterns (data not shown), consistent with theoretical predictions [26].

Figure 6.3(A) shows E-cuts (cuts along the energy axis at a specific Q_z value) of the fluorescence pattern for 10^{-3} M CsI without the monolayer below ($Q_z = 0.018\ \text{Å}^{-1}$) and above the critical angle ($Q_z = 0.030\ \text{Å}^{-1}$). Fluorescence signals are observed only above the critical angel. In the presence of monolayers (DHDP and DMPA), the E-cuts below the critical angle are shown in Fig. 6.3(B). As indicated, the emission lines from Cs^+ are labeled, but no emission lines of I^- (e.g., $L\alpha$, ~ 3.9 keV) are detected. The DHDP or DMPA monolayers have practically identical fluorescence signals, which implies they have similar amounts of Cs^+ ions at the sur-
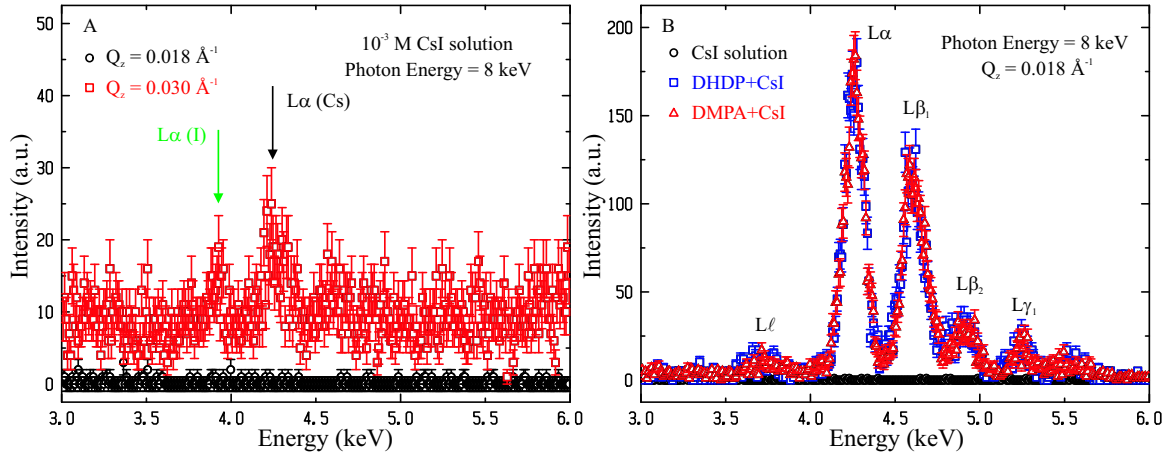
Figure 6.3   (A) Fluorescence intensity versus emission line energy for 10^{-3} M CsI below and above the critical angle as indicated. (B) Fluorescence intensity versus emission line energy at $Q_z = 0.018$ Å^{-1} with and without monolayers at the interface.

face. This is theoretically expected, according to the renormalized Poisson-Boltzmann theory. This is because DHDP and DMPA have similar pK_α (~ 2.1) for the first proton release. At this concentration, it is not expected that the second hydrogen in DMPA will be released, unlike in the case of the divalent [47] or the trivalent ion solutions [94].
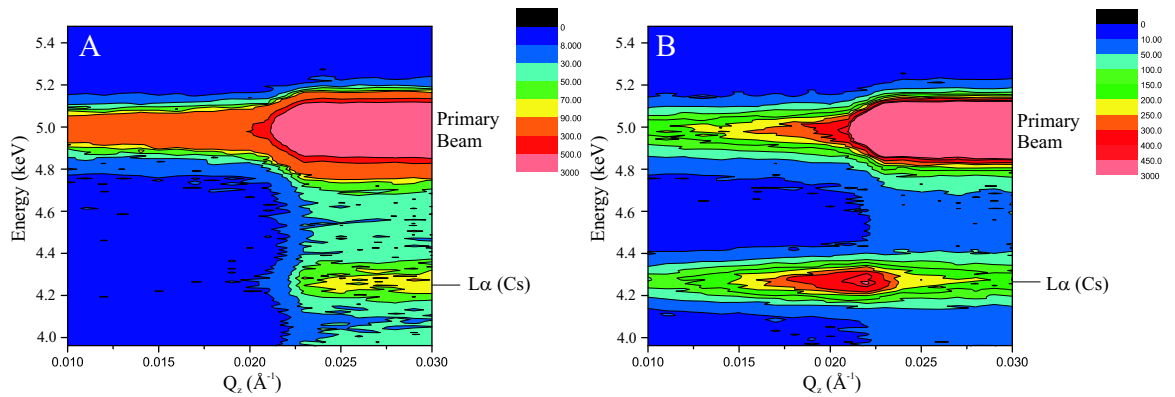
Figure 6.4   Contour plots of fluorescence intensity for 10^{-3} M CsI without (A) and with monolayer DHDP (B). Incident X-ray beam energy is 5.015 keV.

Contour plots of fluorescence intensity for 10^{-3} M CsI with and without the monolayer DHDP with incident X-ray beam energy (5.015 keV) slightly larger than the Cs L_3 resonance

are shown in Fig. 6.4. The strong intensity ridge at approximately 5 keV is due to scattering of the incident beam, labeled as the primary beam. This signal consists of primarily elastic and Compton inelastic scattering. Figure 6.5(A) shows E-cuts obtained from Fig. 6.4 below the critical angle ($Q_z = 0.018$ Å^{-1}). Because the incident beam energy is near the Cs$^+$ L_3 resonance, only emission lines from L_3 (Ll, $L\alpha$,) are observed (the $L\beta_2$ is entangled with the primary beam). Figure 6.5(B) shows the Q_z-cuts of Cs$^+$ $L\alpha$ emission line from those contour plots. Without a DHDP or DMPA monolayer, the fluorescence signal is observed only above the critical angle, that is from the bulk. The intensity slightly increases with Q_z since the penetration depth becomes longer with Q_z [49]. With the DHDP monolayer, fluorescence intensity below the critical angle, due to surface enrichment of Cs$^+$ at the surface, is observed. This intensity reaches a maximum value at the critical angle, due to the multiple scattering, as predicted by the distorted wave Born approximation [44, 98, 99].
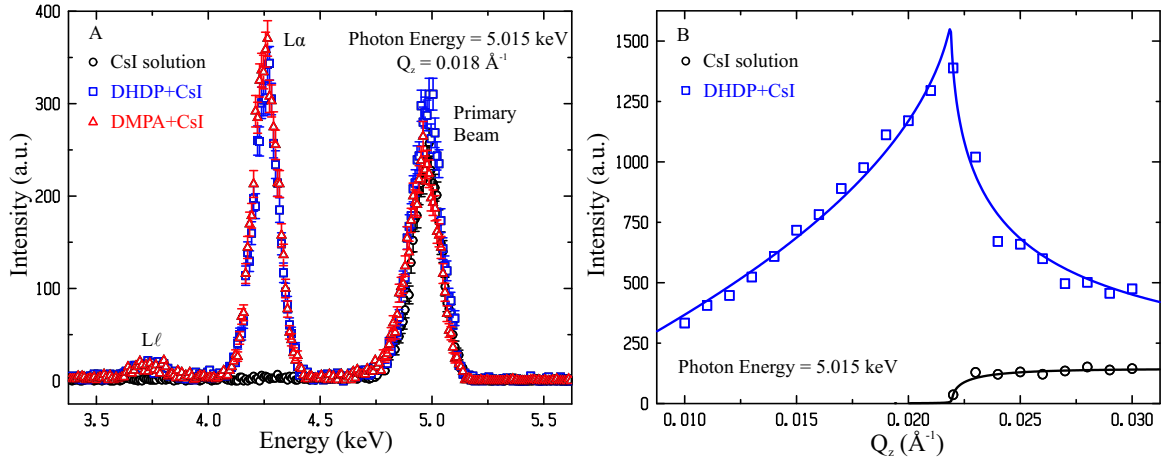
Figure 6.5   (A) Fluorescence intensity versus emission line energy at $Q_z = 0.018$ Å^{-1} with and without monolayer materials (E-cuts from Fig. 6.4). (B) Fluorescence intensity of Cs$^+$ $L\alpha$ emission line versus Q_z with and without DHDP (Q_z-cuts Fig. 6.4).

Similar experiments performed with BaI$_2$ solution (for 10^{-2} M) with monolayers produce similar results. The fluorescence data below the critical angle with and without the DMPA monolayer are shown in Fig. 6.6. Because of the higher bulk concentration (than that used with CsI), the emission lines from both Ba^{2+} and I$^-$ are observed below the critical angle for the

bare surface solution without the monolayer. The presence of DMPA charges at the interface enhance the Ba emission lines, with no detectable change in the intensities of the I^- emission lines.
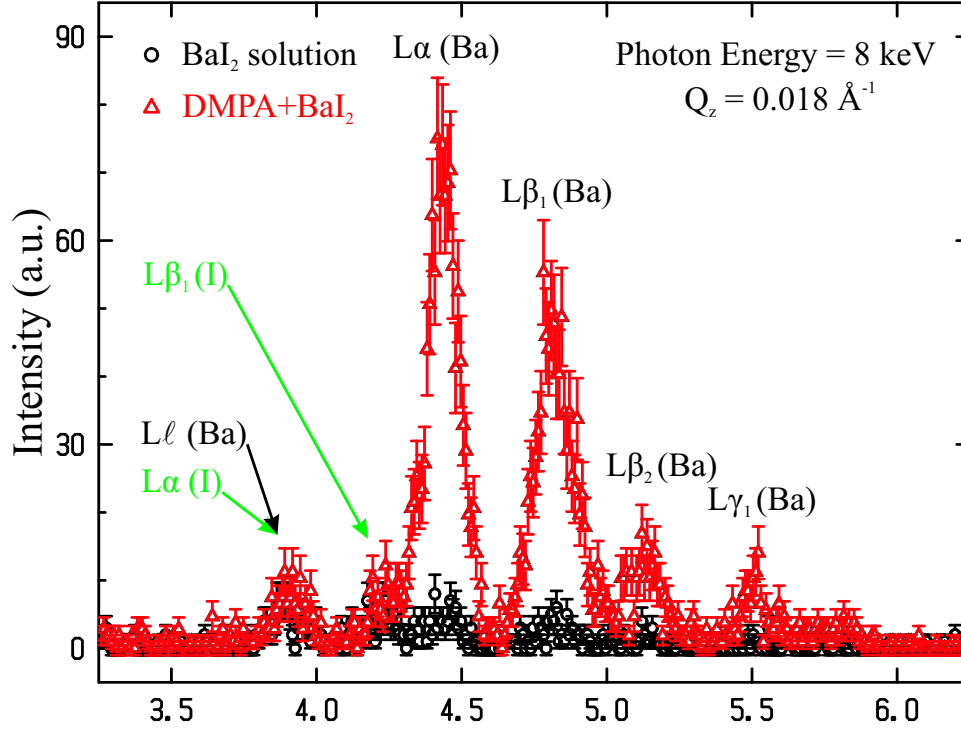
Figure 6.6   Fluorescence intensity versus emission line energy for 10^{-2} M BaI_2 with and without DMPA at $Q_z = 0.018$ Å^{-1}. Emission lines from both Ba^{2+} and I^- are labeled.

6.3   Evaluating Interfacial Ion Concentration

As discussed in Chapter II, given the Cs^+ $L\alpha$ emission line intensity with and without monolayers, the number of adsorbed ions per lipid at the surface can be obtained from

$$N_{ion} = \frac{I_s(\alpha)}{I_b(\alpha)} A_{lipid} D(\alpha) n_b, \tag{6.1}$$

where A_{lipid} is the molecular area for the monolayer, $D(\alpha)$ is the penetration depth for the incident beam, n_b is the ionic bulk concentration, $I_b(\alpha)$ is the fluorescence intensity of the pure solution without the monolayer, and $I_s(\alpha)$ is the fluorescence intensity of the solution with the monolayer after the subtraction of $I_b(\alpha)$. The absorption of emitted photons as they traverse to

the EDD is negligible, since their path in the sample is shorter than that of the incident beam by a factor of at least 100.
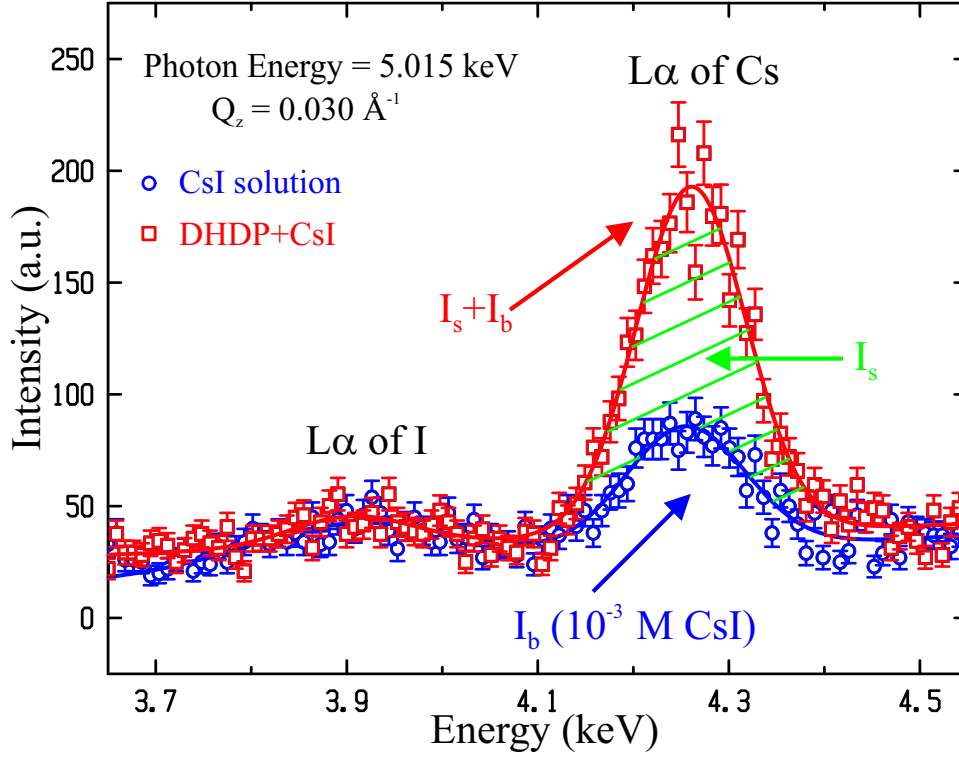
Figure 6.7   Fluorescence data above the critical angle ($Q_z = 0.030\,\text{Å}^{-1}$) for 10^{-3} M CsI with ($I_s + I_b$) and without DHDP (I_b). The shaded area represents I_s of Cs$^+$ $L\alpha$ emission line. X-ray energy is 5.015 keV.

Figure 6.7 shows the fluorescence data above the critical angle ($Q_z = 0.030\,\text{Å}^{-1}$) for 10^{-3} M CsI with and without the monolayer DHDP, and the definition of measured I_s and I_b. Spreading a DHDP monolayer enhances the Cs$^+$ $L\alpha$ emission line intensity (shaded area), due to the accumulation of Cs$^+$ at the charged surface induced by the monolayer materials. However, it does not change the intensity of I$^-$ $L\alpha$ emission line, implying again there is no accumulation of I$^-$ at the surface. Some of the emission lines from different ions overlap, due to the poor resolution of the EDD. For instance, the emission line of the Cs$^+$ $L\alpha$ line (4.3 keV), and the I$^-$ $L\beta_1$ may cause overestimating I_b from the Cs line. To overcome this problem, we used the PyMca program to fit fluorescent data to obtain the relative contributions of both lines from Cs

and I. PyMca program is capable of fitting the fluorescence data with fixed ratios of all emission lines for one specific element. According to intensity of I^- $L\alpha$, which is not mixed up with any other emission line in our system, the intensity of I^- $L\beta_1$ can be calculated and further removed from the overlapping region of the Cs^+ $L\alpha$.

As shown in Eq. 6.1, the number of ions can be obtained by evaluating I_s and I_b at any Q_z above the critical angle. In this study, I_s and I_b were measured at eight different Q_z values (from 0.023 to 0.030 Å^{-1}), yielding an average 0.47 ± 0.09 and 0.54 ± 0.09 Cs^+ per lipid for 10^{-3} M CsI solution with DHDP and DMPA as a monolayer, respectively. Both values are in a good agreement with anomalous reflectivity and constant-Q_z energy scans studies, where more complicated data analysis is required.

6.4   Evaluating the Fine Structure f″(E)

The intensity of the emission line is proportional to the absorption of the ion, which is strongly dependent on photon energy near an absorption edge and also the immediate environment of the ion. By varying the incident beam energy at a fixed Q_z, we obtain the energy dependence of the absorption correction, namely $f''(E)$, up to a scale factor. Performing this experiment below the critical angle does not require any geometry or absorption corrections, since there is negligible bulk contribution to the signal as the emitting ions are concentrated at the first 10 Å of the surface according to RPB theroy.

Figure 6.8 shows the fluorescence intensity of the Cs^+ $L\alpha$ emission line as a function of the incident beam energy. DHDP and DMPA were used as monolayer materials and Q_z was fixed at $0.018\,\text{Å}^{-1}$ to minimize the bulk contribution. The incident beam energy was scanned around the Cs^+ L_3 resonance. Far away from that resonance (± 30 eV), $f''(E)$ for Cs is known from various experimental and theoretical studies [90]. In the vicinity of the resonance, $f''(E)$ of the emitting ion can be influenced by the local environment, and the spectra becomes more complex. By scaling the $f''(E)$ values away from the resonance (± 30 eV), the fluorescence intensity of the Cs^+ $L\alpha$ emission line can be converted to the specific $f''(E)$ in its interfacial environment. As shown in Fig. 6.8, the fluorescence intensity after scaling agrees well with $f''(E)$ (solid line),
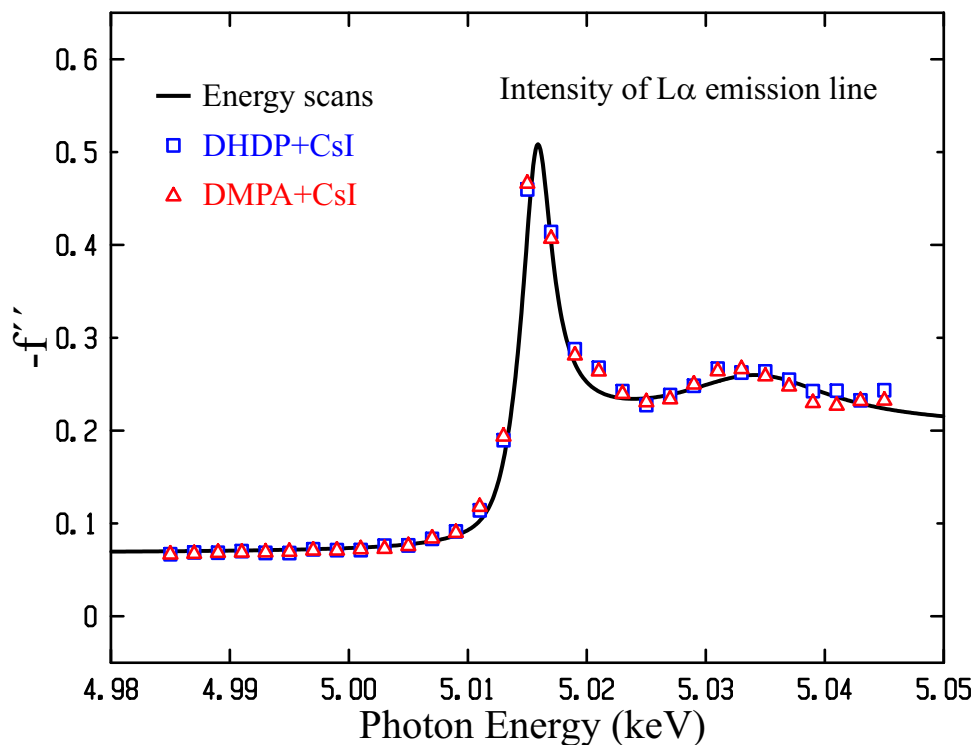
Figure 6.8   Fluorescence intensity of the Cs^+ $L\alpha$ emission line from 10^{-3} M CsI with the monolayers (DHDP and DMPA) at $Q_z = 0.018\,\text{Å}^{-1}$. The intensity is scaled to the $f''(E)$ far away from the Cs^+ L_{III} resonance (± 30 eV). The solid line is $f''(E)$ obtained by fixed-Q_z energy scans shown in Chapter V.

obtained by a more complicated analysis of constant-Q_z energy scans in Chapter V. We note that the reported measurement of $f''(E)$ in bulk aqueous environment (see Fig. 5.5) is slightly different than the one we report here for the Cs^+ L_3 edge. These differences may arise from the fact that the ions in our study reside at the interface with a slightly different environment than that in bulk solution.

6.5   Summary

In the present study, we extended previous X-ray fluorescence techniques that had been used to determine the interfacial ion enrichment at charged monolayers [23, 49, 50, 51, 95, 96, 97] by tracing all emissions lines that can be resolved by our EDD. Although X-ray fluorescence has been used for detecting the number density of ions of similar systems by similar means, these

either needed complicated data analysis [49] or were limited to providing the number density of ions relative to a known density of another ion at the interface [51]. We confirmed that the fluorescence technique below the critical angle provides a quick and reliable determination of the presence of ions, specifically, by identifying the characteristic emission lines of each element that fluoresce. We demonstrated how to calculate the number density of Cs^+ ions at the surface by measuring the fluorescence signals with and without the monolayer above the critical angle. This technique is invaluable in investigating the preferential affinity of ions in the mixed salt solutions [51, 103].

We have also shown that the fine structure of the absorption $f''(E)$ for the specific ions at the surface can be readily obtained from fluorescence signals measured as a function of photon energy near an absorption edge. The fluorescence technique, first introduced by Bloch and coworkers [49], can shed light on the local environment of the ions at the interface in a similar manner to the newly introduced fixed-Q_z energy scan near ion resonances method [48].

CHAPTER 7.   CONCLUSIONS

In this thesis, we presented how to utilize three independent surface sensitive synchrotron X-ray scattering techniques to explore the monovalent ions adsorption at charged air/water surfaces.

Using anomalous X-ray reflectivity, we obtained both the distribution and the integrated number of monovalent ions per charge at the interface over five orders of magnitude in ion bulk concentrations. We conclude that PB theory with the renormalization of surface charge density is strikingly accurate. Other corrections of PB theory, such as finite ionic radius, charge modulations, short-range interactions, image charges, or water restructuring were not necessary for describing the experimental data, implying that such effects, if relevant, would change the distribution at distances shorter than the surface roughness.

Energy scans at fixed momentum transfers and X-ray florescence, as independent techniques, provided the further confirmations to the validity of the RPB theory in the distribution and the integrated number, respectively. These two ion-specific procedures have the advantage of showing the depletion or enrichment of certain ions at the interface, and are even more valuable for the mixed salt solutions. In addition, these two techniques yielded the fine structure of the absorption on an absolute scale, reflecting the local environment of the probed ion near the interface.

The spatial resolution of ion distributions near charged objects (for instance, membranes, DNA filaments, vesicles, polyelectrolytes, and others) in aqueous environment have been improved in recent years with the advances in synchrotron X-ray radiation and have been expanded to more complex systems [86, 100]. These experimental tools, together with theoretical advances [101, 102], brought new insight into the nature of ion accumulation near charged inter-

faces that allow distinguishing between purely electrostatic attraction and ion-specific binding. The understanding we gained with the monovalent ions is of critical importance to the ongoing investigations of charged interfaces at multivalent-ion solutions.

BIBLIOGRAPHY

[1] A. Gouy, J. Phys. (Paris) **9**, 457 (1910).

[2] D. L. Chapman, D. L. Philos. Mag. **25**, 475 (1913).

[3] J. Israelachvili, *Intermolecular and Surface Forces* (Academic Press, London, 2000).

[4] J. Lyklema, *Fundamentals of Interface and Colloid Scienc*e (Academic Press, London, 1995).

[5] O. Stern, Z. Elektrochem. **30**, 508 (1924).

[6] P. P. Debye and F. Hückel, Phys. Z. **24**, 185 (1923).

[7] D. C. Grahame, Chem. ReV. **1**, 103 (1947).

[8] C. W. Outhwaite, J. Chem. Soc., Faraday Trans. II **74**, 1214 (1978).

[9] C. W. Outhwaite, L. B. Bhuiyan, and S. Levine, J. Chem. Soc., Faraday Trans. II **76**, 1388 (1980).

[10] G. M. Torrie, J. P. Valleau, and G. N. Patey, J. Chem. Phys. **76**, 4615 (1982).

[11] R. Kjellander and S. Marcelja, J. Chem. Phys. **82**, 2122 (1985).

[12] P. M. Biesheuvel and M. van Soestbergen, J. Colloid Interface Sci. **316**, 490 (2007).

[13] S. Leikin, V. Parsegian, and D. C. Rau, Annu. Rev. Phys. Chem. **44**, 369 (1993).

[14] M. Manciu and E. Ruckenstein, Adv. Colloid Interface Sci. **112**, 109 (2004).

[15] J. Faraudo and F. Bresme, Phys. Rev. Lett. **92**, 236102 (2004).

[16] A. J. Proesser and E. I. Franses, Colloids Surf. A **178**, 1 (2001).

[17] R. J. Hunter, *Colloid Science* (Academic Press, London, 1981).

[18] S. McLaughlin, Annu. Rev. Biophys. Chem. **18**, 113 (1989).

[19] K. Tajima, K Muramatsu, and M. Sasaki, Bull. Chem. Soc. Jpn. **43**, 1991 (1970).

[20] K. Tajima, Bull. Chem. Soc. Jpn. **44**, 1767 (1971).

[21] K. Kobayashi and K. Takaoka, Bull. Chem. Soc. Jpn. **59**, 93 (1986).

[22] K. Kjaer, J. Als-Nielsen, C. A. Helm, P. Tippman-Krayer, and H. Möhwald, J. Phys. Chem. **93**, 3200 (1989).

[23] J. M. Bloch and W. Yun, Phys. Rev. A **41**, 844 (1990).

[24] M. J. Bedzyk, G. M. Bommarito, M. Caffrey, and T. L. Penner, Science **248**, 52 (1990).

[25] E. LeCalvez, D. Blaudez, T. Buffeteau, and B. Desbat, Langmuir **17**, 670 (2001).

[26] A. Travesset and D. Vaknin, Europhys. Lett. **74**, 181 (2006).

[27] Y. Gur, I. Ravina, and A. J. Babchin, J. Colloid Interface Sci. **64**, 333 (1978).

[28] V. N. Paunov, R. I. Dimova, P. A. Kralchevsky, G. Broze, and A. Mehreteab, J. Colloid Interface Sci. **182**, 239 (1996).

[29] G. L. Gaines, *Insoluble Monolayers at Liquid Gas Interface* (Wiley & Sons, New York, 1966).

[30] J. D. Swalen, D. L. Allara, J. D. Andrade, E. A. Chandross, S. Garoff, J. Israelachvili, T. J. McCarthy, R. Murray, R. F. Pease, J. F. Rabolt, K. J. Wynne, and H. Yu, Langmuir **3**, 932 (1987).

[31] H. Möhwald, Annu. Rev. Phys. Chem. **41**, 411 (1990).

[32] K. Kjaer, J. Als-Nielsen, C. A. Helm, L. A. Laxhuber, and H. Möhwald, Phys. Rev. Lett. **58**, 2224 (1987).

[33] P. Dutta, J. B. Peng, B. Lin, J. B. Ketterson, and M. Prakash, P. Georgopoulos, and S. Ehrlich, Phys. Rev. Lett. **58**, 2228 (1987).

[34] M. Lösche and H. Möhwald, Rev. Sci. Instrum. 55, 1968 (1984).

[35] V. T. Moy, D. J. Keller, H. E. Gaub, and H. M. McConnell, J. Phys. Chem. **90**, 3198 (1986).

[36] S. Henon and J. Meunier, Rev. Sci. Instrum. **62**, 936 (1991).

[37] D. Hönig and D. Möbius, J. Phys. Chem. **95**, 4590 (1991).

[38] G. Cevc, Biochim. Biophy. Acta **1031**, 311 (1990).

[39] J.-F. Tocanne and J. Teissie, Biochim. Biophy. Acta **1031**, 111 (1990).

[40] E. M. Landau, S. G. Wolf, M. Levanon, L. Leiserowitz, M. Lahav, and J. Sagiv, J. Am. Chem. Soc. **111**, 1436 (1989).

[41] S. P. Weinbach, D. Jacquemain, F. Leveiller, K. Kjaer, J. Als-Nielsen, and L. Leiserowitz, J. Am. Chem. Soc. **115**, 11110 (1993).

[42] J. Als-Nielsen and K. Kjaer, in *Phase Transitions in Soft Condensed Matter*, edited by T. Riste and D. Sherrington, (Plenum, New York, 1989).

[43] D. Jacquemain, S. G. Wolf, F. Leveiller, M. Deutsch, K. Kjaer, J. Als-Nielsen, M. Lahav, and L. Leiserowitz, Angew. Chem. **31**, 130 (1992).

[44] K. Kjaer, Physica B **198**, 100 (1994).

[45] M. K. Sanyal, S. K. Sinha, A. Gibaud, K. G. Huang, B. L. Carvalho, M. Rafailovich, J. Sokolov, X. Zhao and W. Zhao, Europhys. Lett. **21**, 691 (1993).

[46] S. Banerjee, Y. J. Park, D. R. Lee, Y. H. Jeong, K. -B. Lee, S. B. Yoon, H. M. Choi, J. -C. Park, J. S. Roh, and M. K. Sanyal, Appl. Surf. Sci. **136**, 41 (1998).

[47] D. Vaknin, P. Krüger, and M. Lösche, Phys. Rev. Lett. **90**, 178102 (2003).

[48] C. Park, P. A. Fenter, N. C. Sturchio, and J. R. Regalbuto, Phys. Rev. Lett. **94**, 076194 (2005).

[49] W. B. Yun and J. M. Bloch, J. Appl. Phys. **68**, 1421 (1990).

[50] J. Daillant, L. Bosio, J. J. Benattar, and C. Blot, Langmuir, **7**, 611 (1991).

[51] V. L. Shapovalov, M. E. Ryskin, O. V. Konovalov, A. Hermelink, and G. Brezesinski, J. Phys. Chem. B **111**, 3927 (2007).

[52] *http://henke.lbl.gov/optical_constants/*

[53] X.-L. Zhou and S.-H. Chen, Physics Reports **257**(4 & 5), 223 (1995).

[54] S. K. Sinha, E. B. Sirota, S. Gasoff, and H. B. Stanley, Phys. Rev. B **38**, 2297 (1988).

[55] J. D. van der Waals, Z. Phys. Chem. **13**, 657 (1894).

[56] J. W. Cahn and J. E. Hilliard, J. Chem. Phys. **28**, 258 (1958).

[57] S. Fisk and B. Widom, J. Chem. Phys. **50**, 3219 (1969).

[58] F. P. Buff, R. A. Lovett, and F. H. Stillinger, Jr., Phys. Rev. Lett. **15**, 621 (1965).

[59] J. D. Weeks, J. Chem. Phys. **67**, 3106 (1977).

[60] M. P. Gelfand and M. E. Fisher, Physica (Amsterdam) **166A**, 1 (1990).

[61] D. Beysens and M. Robert, J. Chem. Phys. **87**, 3056 (1987).

[62] J. S. Huang and W. W. Webb, J. Chem. Phys. **50**, 3677 (1969).

[63] E. S. Wu and W. W. Webb, Phys. Rev. A **8**, 2065 (1973).

[64] A. Braslau, P. S. Pershan, G. Swislow, B. M. Ocko, and J. Als-Nielsen, Phys. Rev. A **38**, 2457 (1988).

[65] B. M. Ocko, X. Z. Wu, E. B. Sirota, S. K. Sinha, and M. Deutsch, Phys. Rev. Lett. **72**, 242 (1994).

[66] M. K. Sanyal, S. K. Sinha, K. G. Huang, and B. M. Ocko, Phys. Rev. Lett. **66**, 628 (1991).

[67] M. Fukuto, O. Gang, K. J. Alvine, and P. S. Pershan, Phys. Rev. E **74**, 031607 (2006).

[68] D. Vaknin, W. Bu, and A. Travesset, J. Chem. Phys. **129**, 044504 (2008).

[69] D. K. Schwartz, M. L. Schlossman, E. H. Kawamoto, G. J. Kellogg, P. S. Pershan, and B. M. Ocko, Phys. Rev. A **41**, 5687 (1990).

[70] J. Sung, K. Park, and D. Kim, J. Phys. Chem. B **109**, 18507 (2005).

[71] D. Vaknin, W. Bu, J. Sung, Y. Jeon, and D. Kim, J. Phys.: Condens. Matter **21**, 115105 (2009).

[72] L. G. Parratt, Phys. Rev. **59**, 359 (1954).

[73] J. Als-Nielsen and P. S. Pershan, Nucl. Instrum. Methods **208**, 545 (1983).

[74] K. Kjaer, J. Als-Nielsen, M. Lahav, and L. Leiserowitz, In *Neutron and Synchrotron Radiation for Condensed Matter Studies*; J. Baruchel, J.-L. Hodeau, M. S. Lehmann, J.-R. Regnard, and C. Schlenker, Edts. Springer-Verlag, Herdelberg, Germany, Vol. III, p. 47, (1994).

[75] D. Vaknin, K. Kjaer, J. Als-Nielsen, and M. Lösche, Biophys. J. **59**, 1325 (1991).

[76] D. Vaknin, K. Kjaer, J. Als-Nielsen, and M. Lösche, Makromol. Chem. Macromol. Symp. **46**, 383 (1991).

[77] D. Vaknin, J. Als-Nielsen, M. Piepenstock, and M. Lösche, Biophys. J. **60**, 1545 (1991).

[78] B. W. Gregory, D. Vaknin, J. D. Gray, B. M. Ocko, P. Stroeve, T. M. Cotton, and W. S. Struve, J. Phys. Chem. B **101**, 2006 (1997).

[79] D. Vaknin, J. Am. Chem. Soc. **125**, 1313 (2003).

[80] M. V. Kaganer, H. Möhwald, and P. Dutta, Rev. Mod. Phys. **71**, 779 (1999).

[81] B. Jancovici, Phys. Rev. Lett. **19**, 20 (1967).

[82] M. J. Bowick and A. Travesset, Phys. Rep. **344**, 255 (2001).

[83] B. W. Gregory, D. Vaknin, J. D. Gray, B. M. Ocko, T. M. Cotton, and W. S. Struve, J. Phys. Chem. B **103**, 502 (1999).

[84] M. Born and E. Wolf, *Principles of Optics*, MacMillan, New York, 1959.

[85] H. Lavoie, D. Blaudez, D. Vaknin, B. Desbat, B. M. Ocko, and C. Salesse, Biophys. J. **83**, 3558 (2002).

[86] G. M. Luo, S. Malkova, J. Yoon, D. G. Schultz, B. H. Lin, M. Meron, I. Benjamin, P. Vanysek, and M. L. Schlossman, Science, **311**, 216 (2006).

[87] D. H. Templeton, L. K. Templeton, J. C. Phillips, and K. Hodgson, Acta Cryst A **36**, 436 (1980).

[88] K. M. Kemner, D. B. Hunter, W. T. Elam, and P. M. Bertsch, J. Phys. Chem. **100**, 11698 (1996).

[89] J.-X. Gao, B.-W. Wang, T. Liu, J.-C. Wang, C.-L. Song, Z.-D. Chen, T.-D. Hu, Y.-N. Xie, J. Zhang, and H. Yang, J. Synchrotron Rad. **12**, 374 (2005).

[90] D. T. Cromer and D. Libermann, J. Chem. Phys. **53** 1891 (1970).

[91] B. L. Henke, E. M. Gullikson and J. C. Davis, At. Data Nucl. Data Tables **54**, 181 (1993).

[92] I. Arčon, A. Kodre, J. Padežnik Gomilšek, M. Hribar, and A. Mihelič, Phys. Scr. **T115**, 235 (2005).

[93] G. A. Krestov, N. P. Novosyolov, L. S. Perelygin, A. M. Kolker, L. P. Safonova, V. D. Ovchinnikova, and V. N. Trostia, *Ionic Solvation*,(Ellis Horwood, New York, 1994).

[94] J. Pittler, W. Bu, D. Vaknin, A. Travesset, D. J. McGillivray, and M. Lösche, Phys. Rev. Lett. **97**, 046102 (2006).

[95] J. M. Bloch, M. Sansone, F. Rondelez, D. G. Peiffer, P. Pincus, M. W. Kim, and P. M. Eisenberger, Phys. Rev. Lett **54**, 1039 (1985).

[96] N. N. Novikova, S. I. Zheludeva, O. V. Konovalov, M. V. Kovalchuk, N. D. Stepina, I. V. Myagkov, Y. K. Godovsky, N. N. Makarova, E. Y. Tereschenko, and L. G. Yanusova, J. Appl. Crystallogr., **36**, 727 (2003).

[97] S. I. Zheludeva, N. N. Novikova, O. V. Konovalov, M. V. Kovalchuk, N. D. Stepina, and E. Yu, Mater. Sci. Eng., C, **23**, 567 (2003).

[98] D. Vaknin, in *Characterization of Materials*, edited by E. N. Kaufmann, **2**, 1027-1047 (John Wiley & Sons, New York, 2003).

[99] G. Vineyard, Phys. Rev. B **26**, 4146 (1982).

[100] K. Giewekemeyer and T. Salditt, Euro. Phys. Lett., **79**, 18003 (2007).

[101] P. Koelsch, P. Viswanath, H. Motschmann,V. L. Shapovalov, G. Brezesinski, H. Möhwald, D. Horinek, R. R. Netz, K. Giewekemeyer, T. Salditt, H. Schollmeyer, R. von Klitzing, J. Daillant, and P. Guenoun, Coll. Surf. A **303**, 110 (2007).

[102] D. Andelman, Proceedings of the Nato ASI & SUSSP on Soft condensed matter physics in molecular and cell biology, pg. 97-122, ed. by W. Poon and D. Andelman, (Taylor & Francis, New York, 2006).

[103] W. Bu, K. Flores, J. Pleasant, and D. Vaknin, Langmuir **25**, 1068 (2009).